

Università degli Studi di Torino
Facoltà di Scienze M.F.N.

CORSO DI LAUREA MAGISTRALE IN FISICA
DELLE INTERAZIONI FONDAMENTALI

TESI DI LAUREA

**Study of electron transport
in Silicon Drift Detectors**

Relatore:
Dott. Stefania Beolé

Corelatore:
Dott. Francesco Prino

Candidato:
Sara Vallero

A.A. 2005/2006

A Irene.

Contents

1 Phase Transitions of Nuclear Matter	3
1.1 Introduction	3
1.2 Phase Transitions	4
1.3 The Quark Gluon Plasma	6
1.3.1 QGP Equation of State	7
1.3.2 A phenomenological model	9
1.4 Experimental approach	10
1.4.1 Nucleus-nucleus collisions	10
1.4.2 Physical observables	13
1.4.3 Highlights from SPS and RHIC	17
1.5 Conclusions	25
2 The ALICE experiment	28
2.1 A Large Hadron Collider (LHC)	28
2.1.1 General considerations	28
2.1.2 ALICE running strategy	30
2.2 The ALICE experiment	31
2.2.1 Design requirements from specific physics topics	32
2.2.2 Experimental Layout	34
2.2.3 Detectors	35
2.3 The Inner Tracking System	39
2.3.1 Design considerations	39
2.3.2 Experimental layout	44
3 Silicon Drift Detectors	47
3.1 An overview on Silicon Sensors	47
3.1.1 Energy response	48
3.1.2 Applications	48
3.1.3 Radiation damage effects	49
3.2 SDDs underlying principles of operation	50
3.2.1 Focusing potential	51
3.2.2 Drift potential	53
3.2.3 Actual potential distribution	53
3.2.4 Collection zone	55

CONTENTS	2
-----------------	----------

3.3	Detector layout for the ALICE experiment	55
3.3.1	Systematic effects	57
3.3.2	Mos charge injectors	60
3.4	Readout electronics	61
3.5	Silicon Drift layers	63
3.5.1	SDDs modules	65
4	Experimental system	69
4.1	Introduction	69
4.2	Set-up	70
4.2.1	Trigger and data acquisition	71
4.3	Trajectory definition	73
4.3.1	Test scan	73
4.3.2	Diffusion measurements	74
4.3.3	Mapping required resolution	74
4.3.4	Mapping trajectory	75
4.4	Set-up optimization	76
4.4.1	Laser wavelength	76
4.4.2	Laser centering and focusing	77
4.4.3	Motor axis angle	79
5	Electron diffusion	82
5.1	Introduction	82
5.2	Electron dynamics	83
5.3	Experimental results	85
5.3.1	Fit to data	85
5.3.2	Drift speed	88
5.3.3	Detector temperature	88
5.3.4	Diffusion coefficient	89
5.4	Comparison with STAR SDDs results	90
5.5	Conclusions	95
6	Detector full-test	98
6.1	Standard procedure	98
6.2	Detector testing	98
6.3	Mapping	103
6.3.1	Typical mapping results	103
6.3.2	Non-linearity of the voltage divider	110
6.3.3	Doping inhomogeneities	110
6.4	Perspective of injector data analysis	113
6.5	Conclusions	116

Chapter 1

Phase Transitions of Nuclear Matter

1.1 Introduction

Exploring the nuclear matter phase diagram and identifying its different phases is one of the main challenges in modern nuclear physics. The fundamental goal is to understand, at the various energy scales, the properties of the nuclear interaction and its macroscopic manifestations.

At low energy densities, hadronic bound states are the degrees of freedom of nuclear matter. Their interaction is described by an effective theory emerging as the low energy limit of Quantum Chromodynamics (QCD), the fundamental theory of strong interactions. At higher energy densities the degrees of freedom are expected to be quarks and gluons, interacting with the strong force.

Heavy ion collisions are exploited to heat up and compress nuclear matter in order to explore the phase diagram at temperatures ranging from a few MeV up to several hundreds of MeV and matter densities up to many times the density of ordinary nuclear matter. The ion beam kinetic energies range from the Fermi energy scale, $\mathcal{O}(100A \text{ Mev})$, through relativistic energies, $\mathcal{O}(1A \text{ GeV})$, to ultra-relativistic energies up to $\mathcal{O}(1A \text{ TeV})$ of the LHC collider.

To gain a deeper insight into the properties of the nuclear interaction, nuclei are excited up to a point where they dissociate into loosely interacting nucleons. The objective of heavy-ion physics at the Fermi energy is, in this context, to establish the properties of the phase transition from the self-bound state inside the nucleus to a gas of freely streaming nucleons. The focus of this research is to understand how collective phenomena and macroscopic properties, involving many degrees of freedom, emerge from the microscopic laws of elementary particle physics. Specifically, heavy ion physics addresses these questions in the sector of strong interactions by studying nuclear matter under conditions of extreme temperature and density. The most striking case of a collective bulk phenomenon predicted by QCD is the occurrence of a phase transition to a de-

confined chirally symmetric state, the quark gluon plasma (QGP).

Next section summarizes the current understanding of the phase diagram of nuclear matter. Section 1.3 focuses on QGP, proposing a general overview of the problem and not pretending to be exhaustive. Finally, in section 1.4 the experimental approach to the study of QGP formation in ultra-relativistic nucleus-nucleus collisions is discussed.

1.2 Phase Transitions

In the framework of the Standard Model, the study of phase diagram of strongly interacting matter is not only of interest in exploring and testing QCD on its natural scale (non-perturbative sector) but it might also shed light on such fundamental questions as the nature of confinement itself and on the process of spontaneous symmetry breaking, which is made responsible for the origin of the effective quark masses (the pion being the Goldstone boson). The early Universe presumably underwent this very phase transition $10^{-6} - 10^{-5}$ s after the Big Bang. Critical phenomena that can occur close to a phase boundary, for example long range density fluctuations (as in condensing water), might have an influence on important aspects of cosmology, such as nucleosynthesis, dark matter and the large scale structure of the Universe.

The study of extreme states of matter created in high-energy nuclear collisions thus provides us an opportunity of gaining insight into many important aspects of different fields of physics. In order for heavy ion collisions to fullfil these expectations, certain necessary preconditions have to be met:

- In order to use macroscopic variables, the system created has to be *big*: its dimensions ought to be much larger than the typical scale of strong interactions ($\gg 1$ fm) and it should consist of *many* particles ($\gg 1$).
- In order to use the language of thermodynamics, the system has to be in equilibrium: its lifetime has to be larger than the typical relaxation times ($\tau \gg 1$ fm/c $^{-1}$). Equilibrium can be reached and maintained throughout the expansion only in a sufficiently interacting system; therefore the number of collisions per particle has to be larger than one. Rescattering of the produced particles (hadrons/quarks) amongst themselves and with the surrounding nuclear matter is therfore of crucial importance and not a trivial effect. Only a few (typically > 3) collisions are required, for example, to equilibrate momentum distributions in low energy nucleus-nucleus collisions [2].
- The energy densities ε needed for QGP formation are predicted by QCD to be of the order of $1 - 3$ GeV fm $^{-3}$, equivalent to a temperature $T_c \approx 150 - 200$ MeV or a baryon density $\rho_c \approx 5 - 10$ times nuclear matter density.

- Because the created system is not static, but rapidly evolving, experimental observables will in general correspond to an integral over the complete space-time history of the reaction until freeze-out. Disentangling the various contributions to a signal from the different phases presents a formidable challenge indeed. Furthermore, a system evolving in equilibrium by definition erases its memory of preceding stages, so it is necessary to identify observables that decouple at different times from the expansion and are more sensitive to the early and hot stages of matter.

Nucleus-nucleus collisions are the tool to heat and compress atomic nuclei. In general, increasing the beam energy leads first to heating of the atomic nucleus and then, as the beam energy is further increased, to temperatures such that the concept of a nucleus will be replaced by that of a hot hadron gas and finally, at still higher beam energies, the concept of hadron gas will be replaced by that of a gas of the fundamental constituents of hadrons: quarks and gluons. To set the scale, typical excitation energies for the three regimes can be characterized by temperatures below 10 MeV, 10 – 100 MeV and above 100 – 200 MeV respectively.

The second relevant parameter to describe the phase diagram is a measure of the density or compression. This is expressed either in terms of the nucleon (or baryon) density ρ in units of ground state nuclear matter density ρ_0 , or in terms of the baryochemical potential μ_B .

At moderate beam energies (of the order of a hundred MeV per nucleon) the nucleus is heated and compressed rather gently and may take during its decompression and cooling a path that leads into two different regions into the temperature versus baryon density plane. In these regions two phases of nuclear matter coexist: the Fermi liquid and a cold gas of nucleons and light nuclei. The system can find itself in the *spinodal region* of negative pressure and it then breaks up into fragments of all sizes in a process called *multiparticle fragmentation* [3].

When the beam kinetic energy is increased to a few hundred to ~ 1000 MeV per nucleon, nuclear matter is compressed to two or three times its normal value and heated to a few tens of MeV. A hot and dense hadron gas is generated. Its properties are dominated by the excitations of its original constituents, the nucleons. Meson production is starting to gain significance.

This region is interesting because, to a very large degree, the available energy is channelled into collective degrees of freedom during the cooling and expansion phase and it allows to sample the properties of hadrons embedded into a dense and hot baryonic medium.

At still higher temperatures and baryon densities there is the boundary from hadron gas to the quark gluon plasma. Along the temperature axis this transition is predicted by Quantum Chromodynamics (QCD). Beyond the phase boundary, confinement of quarks and gluons is lifted and chiral symmetry is re-

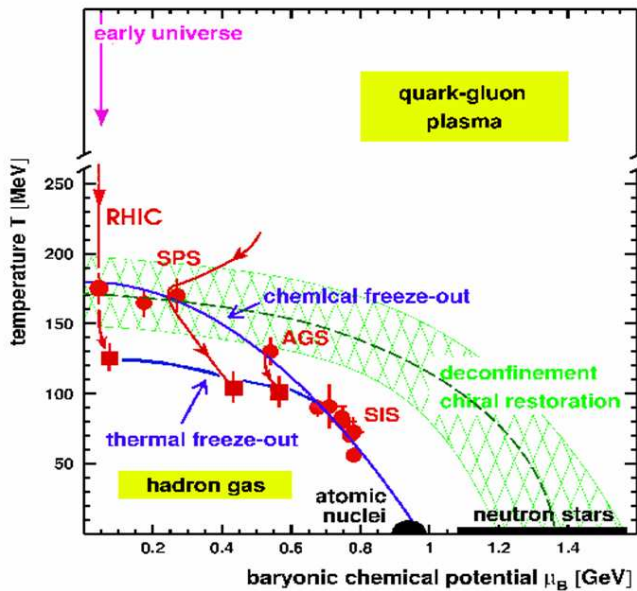


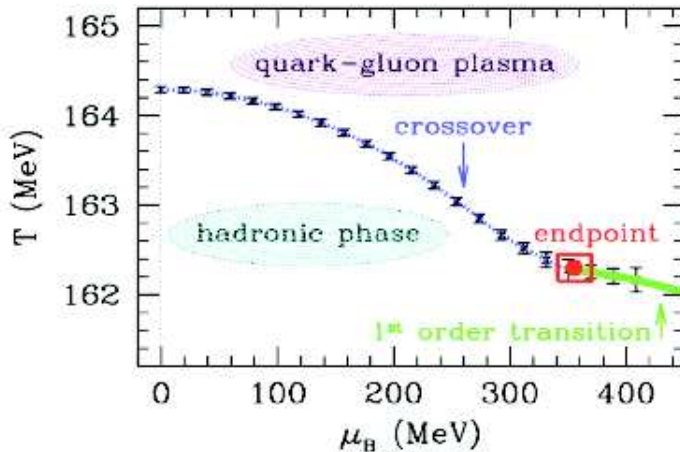
Figure 1.1: *The phase diagram of QCD.*

stored. If quarks are embedded in a sufficiently dense matter, gluons will screen the colour force between quarks, an the effective strong coupling constant vanishes (transition from a *colour insulator* to a *colour conductor*).

QCD calculations are only possible via Monte Carlo on the lattice (because of the non-perturbative regime). Early lattice QCD calculations found a sharp discontinuity in the temperature as a function of energy density diagram. This phenomenon had been associated with a first order deconfinement transition from an ideal hadron gas to an ideal QGP. More recent calculations have however shown that the first order nature of the phase transition is questionable. While calculations both with static ($m_q \sim \infty$) and dynamical ($m_q \sim 0$) fermions render first order phase transitions, the use of realistic quark masses seems to give a second order phase change only or even a smooth cross-over.

1.3 The Quark Gluon Plasma

The first indication of a limiting temperature in hadron interaction was discovered by Hagedorn in 1965 [1]. He postulated an exponential behaviour for the

Figure 1.2: *The order of the phase transition.*

mass densities of hadronic states:

$$\rho(m) \simeq m^\alpha e^{m/m_0} \quad (1.1)$$

in agreement with baryon and meson resonances experimental evidence. Then he integrated this expression over momentum space, obtaining the energy density of excited hadronic matter:

$$n(E) \approx E^{\alpha+2} \exp \left\{ -E \left(\frac{1}{k_B T} - \frac{1}{m_0} \right) \right\} \quad (1.2)$$

This expression is integrable only if the quantity $1/k_B T$ is larger than $1/m_0$, a fact that leads to the existence of a limiting critical temperature $T_c = m_0/k_B$ over which ordinary hadrons cease to exist. A value for m_0 can be extracted from experimental data, and it is found to correspond to the so called *Hagedorn temperature* of $T_c = 200$ MeV.

In the next section the Equation of State of QGP will be introduced, referring to a specific phenomenological model: the MIT bag model [5], which is in agreement with the fact that hadronic matter, composed of individual hadrons, ceases to exist at temperatures above a critical value of the order of Hagedorn temperature.

1.3.1 QGP Equation of State

The equation of state of quark matter is based on the fundamental QCD Lagrangian:

$$L_{QCD} = -\frac{1}{4} \sum_a F_{\mu\nu}^a F_a^{\mu\nu} + \sum_{f=1}^{N_f} \bar{\psi}_f \left(i c \gamma^\mu \partial_\mu - g \gamma^\mu A_\mu^a \frac{\lambda^a}{2} - m_f \right) \psi_f \quad (1.3)$$

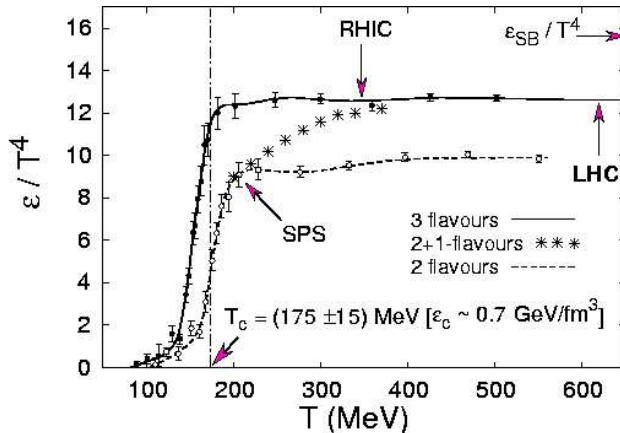


Figure 1.3: Energy density behaviour predicted by lattice QCD calculations: a phase transition is expected at a temperature of about 200 MeV.

where f is the quark flavour and the field strength is:

$$F_{\mu\nu}^a = \partial_\mu A_\nu^a - \partial_\nu A_\mu^a + g f_{abc} A_\mu^b A_\nu^c \quad (1.4)$$

f_{abc} are the structure constants of SU(3), the colour gauge group. The explicit summation over these constants in the Lagrangian, runs over the possible flavours of quarks. The last term in the field strength underlines the non-abelian nature of the group: a crucial feature of the theory.

The renormalized coupling constant is a function of the transferred momentum Q^2 :

$$\alpha_s \equiv \frac{g^2(Q^2)}{4\pi} = \frac{4\pi}{(11 - \frac{2}{3}N_f)\ln(\frac{Q^2}{\Lambda^2})} \longrightarrow 0 \quad \text{for } Q^2 \rightarrow \infty \quad (1.5)$$

QCD predicts a weakening of the quark-gluon interaction at short distances or equivalently at high momenta Q^2 . The accepted value for the QCD scale parameter is $\Lambda \simeq 150$ MeV.

The phase transition can be seen as the transition between two different states of matter which correspond to different states of vacuum in QCD: the perturbative and chirally symmetric vacuum, where quarks and gluons propagate almost freely, and the physical non perturbative vacuum with broken chiral symmetry.

In principle the Lagrangian density gives all the dynamical input necessary for strong interaction thermodynamics. From L the Hamiltonian H may be constructed and then the *partition function*:

$$Z(T, V) = Tr(e^{-H/T}) \quad (1.6)$$

for a thermodynamical system at temperature T and within a spatial volume V ; the trace runs over all microscopic physical states. The desired thermodynamic observables are obtained from Z by differentiation, getting for instance:

$$\epsilon = \frac{T^2}{V} \left(\frac{\partial \ln Z}{\partial T} \right)_V \quad (1.7)$$

for the energy density, and:

$$P = \left(\frac{\partial \ln Z}{\partial V} \right)_T \quad (1.8)$$

for the pressure.

The perturbative approach is suitable for the actual evaluation of Z only in the case in which the interactions are weak. But the transition to QGP is by nature non-perturbative and cannot be addressed in such a fashion. The only approach known at present is lattice formulation, replacing space-time continuum with a discrete and finite set of lattice points.

1.3.2 A phenomenological model

To get a more intuitive comprehension of the problem, we introduce a simple phenomenological model: the *MIT bag model*.

In a QGP the long range colour force is screened due to collective effects, and the medium becomes a colour conductor, as opposed to ordinary vacuum which acts as a perfect colour insulator confining colored quarks and gluons to a hadron "bag". In the bag model approximation, quarks are treated as massless particles inside a bag of finite dimensions and are infinitely massive outside the bag. Confinement is the result of the balance between *bag pressure* B and the stress arising from the kinetic energy of quarks. The effect of non perturbative QCD is taken into account through the inward bag pressure B . This balance of opposite pressures provides a simple understanding of why new phases of matter are expected. A unconfined state of constituents is possible when bag pressure is not able to compensate a too high kinetic stress from the quarks, and a large pressure of quark matter arises when the temperature of matter or the baryonic density are large. So, there are two crucial quantities in determining a possible phase transition: temperature and baryochemical potential.

An estimation of the transition temperature from ordinary matter to QGP at zero baryon density can be obtained by comparing the equations of state of the two simplest approximations: non interacting hadron gas of massless pions and an ideal gas of massless gluons and two-flavour quarks (plasma). The energy density ϵ and the pressure p of an ideal gas of massless particles may be expressed as a function of temperature T by the following thermodinamical relations:

$$\epsilon = \frac{g}{30} \pi^2 T^4 \quad (1.9)$$

$$P = \frac{\epsilon}{3} = \frac{g}{90} \pi^2 T^4 \quad (1.10)$$

where g is a degeneracy factor. Since bosons and fermions are governed by a different quantum statistic, g is different for the two considered gases. Defining n_b and n_f the degrees of freedom for bosons and fermions respectively, the degeneracy factor is given by:

$$g = n_b + \left(1 - \frac{1}{2^3}\right) n_f \quad (1.11)$$

For the hadron gas the number of degrees of freedom is $n_b = 3$ as the three isospin pion states, while $n_f = 0$. In the case of QGP the boson (gluon) degrees of freedom are $n_b = 16$ (8 color states \times 2 spin states) and the fermion (quarks) degrees of freedom are $n_f = 24$ (2 flavours \times 3 colors \times 2 spins \times for quarks and anti-quarks).

Therefore, for the pion gas energy density and pressure are given by:

$$\epsilon_\pi = \frac{3}{30} \pi^2 T^4 \quad (1.12)$$

$$P_\pi = \frac{\epsilon_\pi}{3} = \frac{3}{90} \pi^2 T^4 \quad (1.13)$$

and for the QGP:

$$\epsilon_{QGP} = \frac{37}{30} \pi^2 T^4 + B \quad (1.14)$$

$$P_{QGP} = \frac{37}{90} \pi^2 T^4 - B \quad (1.15)$$

At the critical temperature $T_c \simeq 0.75 B^{1/4} \simeq 150$ MeV (if $B \simeq 200$ MeV) the pressure of the two states is equal, while the energy density between the two differs by a considerable amount: $\Delta\epsilon_c \simeq aB \simeq 0.8$ GeV/fm³ [6]. This simple model predicts a first order transition and the value $\Delta\epsilon_c$ may be interpreted as latent heat required for the phase transition to take place, neglecting hadronic mass temperature dependence and interactions between quarks and gluons. Performing first order perturbative calculations $\Delta\epsilon_c$ is reduced by a factor ~ 2 for $\alpha_s = 0.5$ but a first order transition is still predicted.

At low temperatures a deconfined quark matter is still possible at very high baryon densities. In fact due to Pauli exclusion principle, no more than one fermion can populate a state with a defined set of quantum numbers. So, as quark density increases, these particles must populate states of greater momentum. Thus, the gas acquires more and more pressure with quark density because of the degeneracy of states. At $T = 0$ the critical baryon density is found to be $n_B = 0.72$ fm⁻³, about 5 times the density of normal nuclear matter.

1.4 Experimental approach

1.4.1 Nucleus-nucleus collisions

In this section the high-energy reaction between two heavy nuclei will be considered. Since nuclei are extended objects, their geometry plays an important

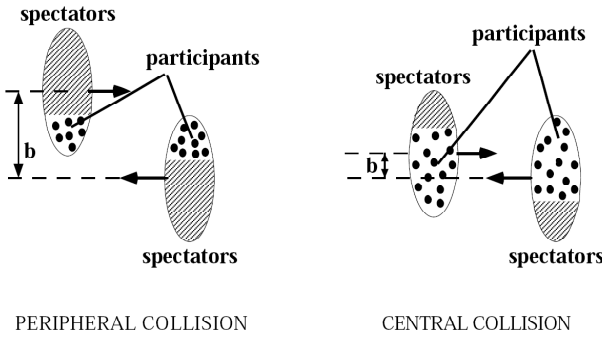


Figure 1.4: *Peripheral and central collision in the centre of mass system of the two nuclei.*

role: it is usual to consider straight-line trajectories for nucleons, justified by the fact that the energy exchanged between two nucleons during the interaction is considerably lower than the momentum of colliding beams. According to that, the impact parameter b is defined, which measures the distance between the centers of two nuclei. The impact parameter separates nucleons into *participants*, with primary nucleon-nucleon collisions, and *spectators* which proceed with little perturbation along the original direction. In a *central collision* the impact parameter is ideally zero and the two nuclei completely overlap. It is important to distinguish between central and peripheral collisions because of the energy density released, which is maximal in a central collision. In this case when the two nuclei collide a volume of hot hadronic matter is created and the search for QGP is made possible (RHIC, LHC). Collisions can be either *coherent* or *incoherent*. In the first case each nucleus interacts as a whole and there is a collective effect, the second one is a succession of independent nucleon-nucleon interactions. If the system is at equilibrium, coherent collisions can be treated with thermodynamical and hydrodynamical models; thermodynamics considers the exchange of energy and heat while hydrodynamics takes into account the mechanical motion of expansion and compression of hadronic matter. The initial energy density created in a heavy ion collision is usually estimated from the Bjorken hydrodynamical model in the so called Bjorken limit ($\sqrt{s} \gtrsim 100$ GeV). The Bjorken limit is a regime of *full transparency* in which baryons from interacting nuclei move away from the center of mass after the collision and leave the mid-rapidity¹ region at zero baryon density. The opposite situation is

¹The rapidity of a particle is defined in terms of its energy-momentum components p_0 and p_z (z is the beam direction) by:

$$y = \frac{1}{2} \ln \left(\frac{p_0 + p_z}{p_0 - p_z} \right)$$

For high momenta y coincides with the pseudorapidity η , defined as $\eta = -\ln[\tan(\theta/2)]$, where θ is the angle between the particle momentum and the beam axis. Thus different regions

the *full stopping*, where the colliding baryons are stopped in the center of mass system and eventually form a QGP with high baryon content.

The Bjorken model provides an estimation of the initial energy density as a function of the transverse mass ($m_T = \sqrt{p_T^2 + m^2}$) and the transverse overlapping area (A):

$$\epsilon = \frac{m_T}{\tau A} \left(\frac{dN}{dy} \right)_{y=0} \quad (1.16)$$

where $(dN/dy)_{y=0}$ is the rapidity density of particles at mid-rapidity and τ the proper time at which particles are produced (~ 1 fm/c). On the contrary, models of incoherent collisions do not allow an estimate of ϵ . In the analysis of experimental data a hybrid methodology can be applied: the energy density is estimated from the Bjorken model and the kinematics of the secondary particles is compared with models of incoherent collisions.

Now we consider the space-time evolution of a central collision. In the first moments of the reaction, hard scattering processes on the parton level may occur with a small probability (given by structure functions and perturbative QCD cross sections). In addition soft nucleon-nucleon collisions (with large cross sections) between the two Lorentz contracted nuclei redistribute a fraction of the initial beam energy into other degrees of freedom. After a short *formation time* (~ 1 fm/c) partons materialize out of the highly excited QCD field. Thermal equilibrium may now be approached via individual parton-parton interactions (or equivalently string-string interactions [3]). Calculations of the mean free path of quarks in QCD matter give a value of $\lambda \approx 0.5$ fm at energy densities $\epsilon = 2$ GeV/fm³, thus indicating that equilibrium may indeed be reached in collisions of heavy nuclei, where the transverse radii, and the initial dimensions, are larger than λ .

The system expands rapidly, mainly along the longitudinal direction, and lowers its temperature until it reaches the critical transition temperature T_C after $\tau \approx 3 - 5$ fm/c. In the case of a first order transition, the matter remains a long time ($\tau > 10$ fm/c) in a *mixed phase*; in this lapse of time the many degrees of freedom of QGP (partons) are rearranged into the smaller number available in the hadron phase, with a large release of latent heat. In the last and hadronic phase (*hadron gas*, $\tau \gg 10$ fm/c) the still interacting system keeps expanding in an ordered flow. It may expand to dimensions up to $10^4 - 10^5$ fm³ until *chemical freeze-out*, when anelastic interactions between hadrons cease and particle multiplicities reach their final configuration. When even elastic collisions stop (*thermal freeze-out*), hadrons stream freely away to be detected in the experiments.

can be considered: a *central* zone with $y = 0$ (mid-rapidity) and two *fragmentation* zones ($y \simeq y_{beam}$).

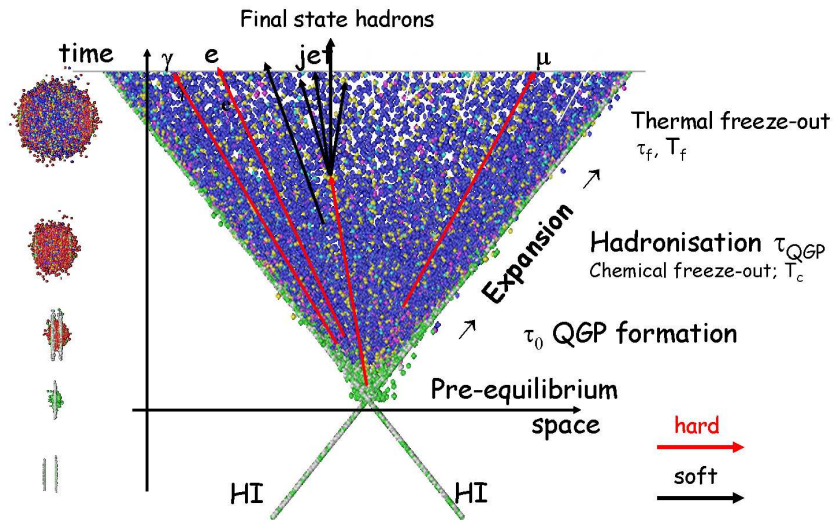


Figure 1.5: *Space-time evolution of a central collision between heavy ions.*

1.4.2 Physical observables

Observables and signatures that can probe the possible formation of QGP are mainly indirect signals, since they are related to particles which have undergone significant reinteractions between the early collision stages and their final observation. Only a few of them, like direct photons or dileptons, carry direct information of the early stages of the collision, but are extremely difficult to measure.

The various signals can be associated with the different stages of the evolution:

Initial conditions

Their knowledge requires the measurement of global event features. Specifically from baryon distributions, transverse energy and particle production one can estimate the impact parameter, the initial volume, the degree of stopping and the energy density reached on an event-by-event basis².

²An event-by-event analysis is useful for the study of fluctuations in particle multiplicities, ratios, transverse momenta and correlations, which would otherwise be washed out when averaging over many events.

Quark Gluon Plasma

Weakly interacting probes decouple at early times and are the only means to get direct informations on the plasma phase. Such observables (*direct photons*, *dileptons*) should emerge as thermal radiation from the heated matter, without being altered by final-state effects, and contain information only about temperature and space-time volume of the emitting source, but nothing about the nature of its constituents. Instead, signals originating from hard scattering processes at the very beginning of the reaction, are not directly connected with plasma formation but serve as a tool to probe the state of the surrounding QCD matter. The most representative phenomena are:

- *Direct photons and dileptons*: the study of these signals requires a precise measurement of the rates and p_t spectra of π^0 and η , in order to separate the actual photon component from the background arising from their decays. For what concerns dilepton pairs, they offer the advantage of carrying invariant mass, which makes it possible to distinguish among different production processes, and to observe vector mesons from their direct decay.
- *J/Ψ suppression*: charmonium is the bound state of a charm and a anti-charm quarks ($c\bar{c}$) and, owing to its large mass, can only be produced in high transferred momentum collisions between quarks (early and hotter stage of the nucleus-nucleus collision). The principle at the base of this process is similar to the one that rules the formation of bound states in electrodynamics; it assumes the presence of an attractive potential which is different in QED and QCD due to the different behaviour of the two coupling constants. In QCD the potential has a Coulomb long range term ($\propto 1/r$) and a short range term ($\propto r$) responsible for quark confinement into hadrons:

$$V(r) = \sigma \cdot r_D \left(1 - e^{-r/r_D} \right) - \frac{\alpha}{r} e^{-r/r_D} \quad (1.17)$$

where r_D is Debye radius ($0.3 - 0.5$ according to QCD lattice calculations) and its effect is to screen color charges (*Debye screening*). Therefore, a $c\bar{c}$ state formation is possible only if its dimension is $\ll r_D$. At hadronization the formation of lighter mesons such as D or \bar{D} (open-charm) is more favorable, because of the greater abundance of lighter quarks, thus leading to a suppression of $c\bar{c}$ states production in a plasma. Charmonium suppression, predicted in 1986 by Matsui and Satz [7], is a function of the temperature reached by deconfined matter because color charge density increases with temperature. The loosely bound χ_C and Ψ' should start to be suppressed at a lower temperature with respect to the strongly bound J/Ψ state.

At RHIC J/Ψ measurements were performed both in the channel $J/\Psi \rightarrow \mu^+ \mu^-$ and $J/\Psi \rightarrow e^+ e^-$. At SPS the only channel studied was the muonic one and the cross-section was quoted relative to the Drell-Yan cross-section ($q\bar{q} \rightarrow \mu^+ \mu^-$) per nucleon-nucleon collision.

- *open charm enhancement*: carries information about the partons kinematics in the very early stage. Charm can only be produced in the early and hottest stage of the collision; the probability of subsequent annihilation is very low and essentially all the produced charm ends up in the final state, mostly in the form of open charm mesons (D and \bar{D}). So an enhancement of the charm observation in the final state is predicted and the degree of enhancement is expected to be sensitive to the initial value of the energy density and to the duration of the thermalization process [10, 11].
- *strangeness enhancement*: in a QGP the production of strange quarks should be favoured by different mechanisms. Due to partial chiral symmetry restoration, their mass is reduced from ~ 500 MeV to ~ 150 MeV. Besides, light quarks production is inhibited by the Pauli blocking system, favouring strange quarks formation. During the collision light quarks produced begin to fill the available phase space. As the baryon density increases, greater energy is required to produce light pairs, favouring the production of $s\bar{s}$ states. Nevertheless, strangeness is enhanced in nuclear collisions at all center of mass energies. The SPS strangeness data never supported a QGP conclusion, even though this phenomenon was one of the original proposed signatures for the QGP [13].
- *jet quenching*: is due to the suppression of high p_t hadron spectra caused by the interaction of high E_T partons, producing these particles, with the medium. The energy loss of such partons is very sensitive to the density of the medium and can be used as a probe. In fact, observables associated with hard processes (hard probes) are of particular interest because their ability to probe dense matter is less complicated by the hadronization process. Furthermore, at high energies they dominate the underlying collision dynamics, which will determine the initial conditions of the produced partonic system.

Phase Transition

The presence of a transition could be signalled by long range fluctuations in multiplicity or by intermittency patterns. The long lifetime associated with a first order phase transition might reflect itself in Bose-Einstein correlations of identical particles. A tool to study this phenomenon is the *interferometry of identical particles* (π, K, p)³, performed in analogy with the Hanbury-Brown and Twiss (HBT) method in astronomy. Consider the experimental two-pion

³The use of pions to measure the space-time dimensions in $p\bar{p}$ annihilation was proposed by G. Goldhaber, S. Goldhaber, W. Lee and A. Pais [13].

correlation function:

$$C(p_1, p_2) = \frac{N_2(p_1, p_2)}{N_1(p_1)N_1(p_2)} \quad (1.18)$$

where the p_i are the 4-momenta of the particles and N_1 and N_2 are the single/double pion inclusive distribution functions respectively. This function is analyzed in terms of:

$$C(p_1, p_2) = 1 + \lambda|\rho(Q)|^2 \quad (1.19)$$

where λ is the incoherence or chaoticity parameter and Q is often chosen as the invariant 4-momentum difference $Q = \sqrt{-(p_1 - p_2)^2}$. Besides $\rho(Q)$ is the Fourier transform of the freeze-out space-time density. A common parametrization of $\rho(Q)$ is a Gaussian space-time density distribution, separable in space and time, which yields a Gaussian correlation function. This parametrization assumes a source with emitters fixed in space-time.

Even though the correlation function measures the pion space-time distribution at freeze-out, the domain where they decouple from strong interaction, an eventual phase transition to QGP in the early expansion phase could modify the dynamics of the expansion, and thus the correlation among identical particles. Ideally, the presence of a phase transition (constant temperature over a range of energy densities) would manifest in a characteristic dependence of the average p_t on the energy density.

Hadron gas

The evolution and cooling of the system is usually described in terms of *hydrodynamic expansion*. In the early 1950's Belenkij and Landau [14] observed that Fermi statistical model [15], describing the number of secondary particles in nucleon-nucleon collisions in terms of temperature and chemical potential ⁴, has to be extended to hydrodynamics when considering particle spectra. The analysis of particle spectra for different particles permits to gain information about the presence of a collective and non thermal motion called *transverse flow*. By considering the transversal degrees of freedom only, the energy produced in the collision may be studied independently from the beam kinematics. In principle, the investigation of p_\perp and m_\perp spectra could give information on the fireball temperature at freeze-out and on the global collective expansion. The transverse mass distribution depends on the temperature T through:

$$\frac{d^2N(m_t, x)}{dm_t dx} \approx m_t \cdot e^{-m_t/T} \quad (1.20)$$

Furthermore, the longitudinal expansion of the source introduces a strong correlation of the position and momentum of particles which could be measured via two-particle correlations.

⁴A system completely described by temperature and chemical potential, able to exchange energy and matter with the external environment, is referred to as a *grand canonical ensemble*. The concept of ensemble was introduced by Gibbs in order to define a set of ideal copies of a real thermodynamic system, representing all its possible realizations.

Besides transverse (or radial) and longitudinal (or thermal) flow, another kind of collective motion is predicted in a dense medium: the *elliptic flow* due to anisotropy in particle emission in peripheral collisions (figure 1.6).

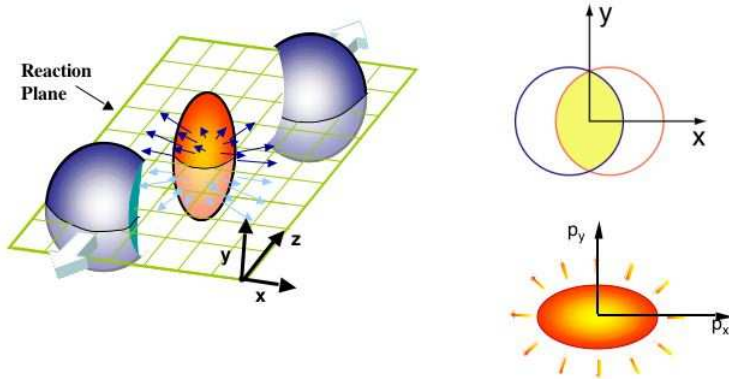


Figure 1.6: *Elliptic flow in peripheral collisions: almond shaped overlap zone generated just after an $A+A$ collision where incident nuclei are moving along the z axis (left). Spatial distribution (top right). Momentum distribution after elliptic flow develops (bottom right).*

1.4.3 Highlights from SPS and RHIC

The first evidences of a new state of matter compatible with the theoretically predicted QGP, emerged in February 2000 from the results obtained with the CERN SPS heavy ion program (started in 1986). Different experiments were designed for the study of specific signals and are summarized in figure 1.7.

SPS accelerator allowed Pb-Pb collisions at $\sqrt{s} = 17$ GeV and showed the eventual formation of a particular state with energy density of $\epsilon \approx 3$ GeV/fm 3 and mean particle momenta corresponding to $T \simeq 240$ MeV. Furthermore charmonia suppression and strangeness enhancement were actually observed.

Charmonium suppression: this phenomenon is the most evident indication that SPS experiments have reached the threshold energy density for deconfinement. J/Ψ cross-sections are normalized to the Drell-Yan process, since the latter scales with the number of collisions and does not undergo absorption, being not affected by nuclear effects. Charmonium suppression was studied in detail by the NA38 and NA50 collaborations and the results came out from the analysis of different observables. Figure 1.8 shows the measured ratio between J/Ψ and DY cross-sections as a function of L , the mean length of nuclear matter traversed by the $c\bar{c}$ pair. This geometrical quantity is strictly related to the impact parameter and increases with increasing centrality of the collision. The plot

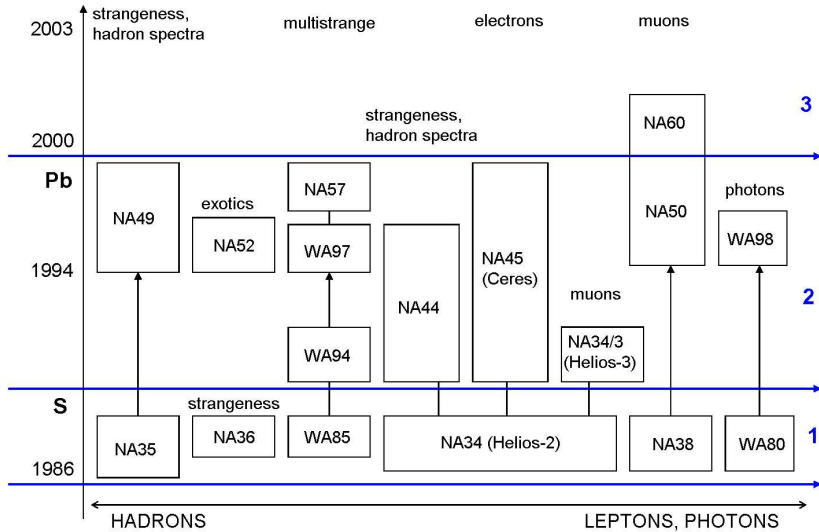


Figure 1.7: 3 generations of experiments at SPS.

clearly shows an exponential scaling law for proton-nucleus, sulfur-uranium and peripheral Pb-Pb reactions, compatible with the nuclear absorption of a pre-resonant $c\bar{c}$ state. On the contrary, in Pb-Pb central collisions (larger values of L) the experimental points abruptly deviate from this behaviour, indicating the onset of an anomalous J/Ψ suppression.

The same trend emerges as a function of the energy density released in the collision. In figure 1.9 J/Ψ measured cross sections are shown, normalized to the expected value of the cross-section for nuclear absorption only (fit to pA data). Above $\epsilon \approx 2.2$ GeV/fm³ experimental data indicate a deviation from the normal regime that can be explained with $c\bar{c}$ quarks deconfinement.

Strangeness enhancement: multistrange particles production at midrapidity has been studied by the WA97 and NA57 collaborations. In the past years a strangeness-enhanced phase was expected during statistical hadronization, causing each final state hadron to contain a larger number of strange quarks if referred to a state evolution without phase transition and no strangeness enhancement. Recent results achieved by WA97 using p-Be as a reference are shown in figure 1.10. Strange baryons enhancement is likely to increase smoothly with increasing collision energy, without any sharp discontinuity. Due to the lack of measurements in peripheral collisions, early results showed an approximate flatness of the enhancement for a number of participants $N_{part} > 100$, attracting some attention as an evidence of a pre-hadronic state.

Besides, a *global strangeness enhancement* emerges from the study of hyperons

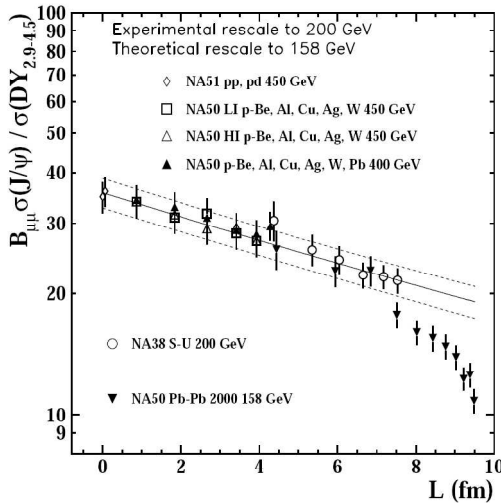


Figure 1.8: The ratio between J/Ψ and DY cross sections as a function of L , for several collision systems, compared to the normal nuclear absorption pattern.

in a large kinematic region. The NA49 experiment found a global enhancement factor of about 2 (figure 1.11) by studying K-meson production in Pb-Pb central collisions relatively to p-A (kaons carry about 75% of the strangeness content of the final state).

Final state evolution: the study of final state particles is a tool to understand the system evolution and dynamics. In particular the two topical observables are transverse mass distributions and identical particles correlations (HBT). These quantities are linked to the temperature of the system at the thermal freeze-out.

As shown in figure 1.12 the inverse slope T of the transverse mass distribution increases with the mass of the considered particles. This behaviour reflects the superposition of the thermal motion of the expanding system and a transverse collective flow, caused by the explosion of the fireball. The departure of the Ω from the systematics may be due to an early freeze-out of this particle, since it cannot form resonances with pions (having zero isospin) and therefore decouples very soon from the expanding hadron gas.

HBT analysis permits the measurement of the system radius at freeze-out, which is found to be 6 – 7 fm in Pb-Pb central collisions (and grows with event centrality). Contributions of thermal motion and radial flow can be separated by combining the informations from transverse mass spectra and Bose-Einstein interferometry. Experimental values for temperature at thermal decoupling and radial expansion velocity are $T = (120 \pm 12)$ MeV and 0.55 ± 0.12 respectively.

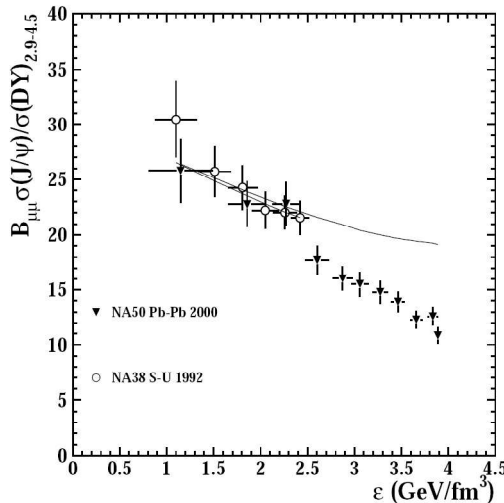


Figure 1.9: *Anomalous J/Ψ suppression as a function of energy density, for $S-U$ and $Pb-Pb$ collision systems, compared to the normal nuclear absorption pattern. Expected J/Ψ are extracted from a fit to pA data.*

The system has a transversal expansion with a speed about a half the speed of light, so it is usual to refer to deconfined matter expansion before adronization as *Little Bang*.

Another experimental evidence seems to point out at QGP formation: in the evolution of a hot and dense system towards equilibrium, chemical freeze-out is expected to happen before thermal freeze-out at a higher temperature. Besides, the temperature of chemical decoupling (at which particle multiplicities have reached their final configuration) is expected to be very close to the critical value T_C for the phase transition to take place. A simple *thermal model* can be considered, assuming that the system is at thermal equilibrium at the chemical freeze-out. In this case a *grand partition function* Z can be written. In a grand canonical ensemble the probability of a given state depends on the temperature T and on the chemical potential μ , according to the Gibbs distribution:

$$p_{i,j} = \frac{\exp\left[-\frac{(E_i - \mu N_j)}{K_B T}\right]}{Z} \quad (1.21)$$

consequently the grand partition function is given by:

$$Z = \sum_{i,j} \exp\left[-\frac{(E_i - \mu N_j)}{K_B T}\right] \quad (1.22)$$

Particle multiplicities for different species can be calculated from the partition

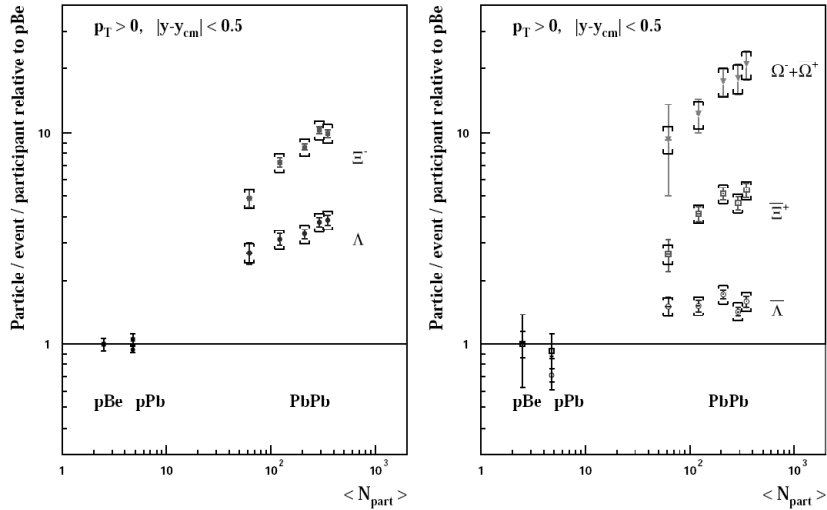


Figure 1.10: dN/dY at midrapidity as a function of the total number of participants for strange and multi-strange baryons.

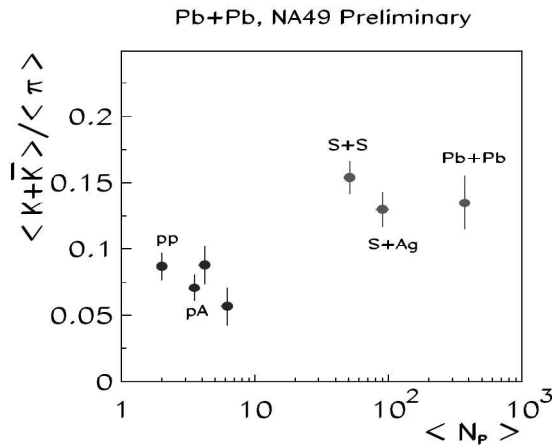


Figure 1.11: Phase-space integrated kaon to pion multiplicities from NA49 experiment.

function, obtaining a good fit of the measured ratios of particle numbers. The system temperature extracted from the fit to experimental data is about 160-

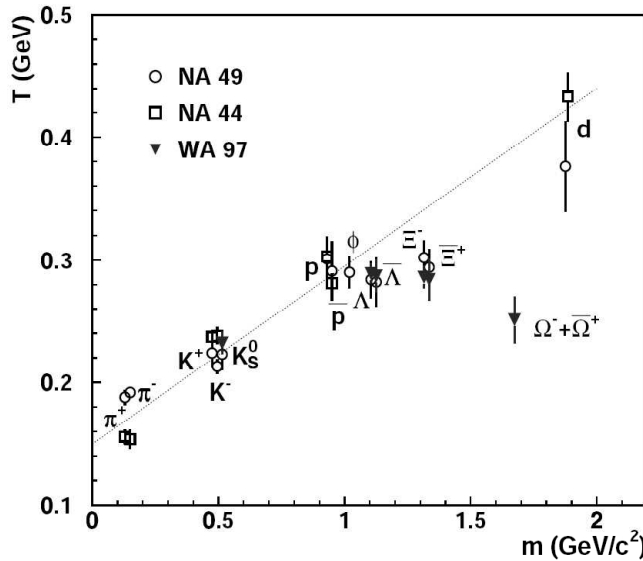


Figure 1.12: Inverse slope T of transverse mass spectra as a function of particle mass. Data are from WA97, NA44 and NA49 experiments in Pb-Pb collisions at CERN SPS.

170 MeV (higher than the one estimated for thermal freeze-out from radial flow analysis).

SPS data are not the only available results concerning ultra relativistic heavy ion collisions. Since year 2000 four experiments have started their activity at the Relativistic Heavy Ion Collider (RHIC) of Brookhaven laboratory: PHENIX, STAR, PHOBOS and BRAHMS. RHIC allowed Au-Au collisions at $\sqrt{s} = 200\text{ GeV}$ per nucleon pair and each experiment was designed for the study of a specific target of physics. Specifically:

- PHENIX is a general purpose experiment, allowing the measurement of direct photons and leptons
- STAR is a general purpose experiment, allowing the measurement of plasma signatures and event-by-event correlations between different observables
- PHOBOS measures fireball parameters (temperature, dimensions, density) and particle multiplicities

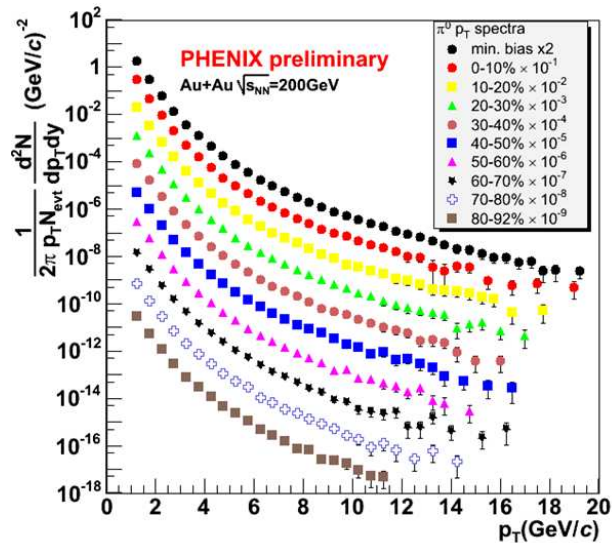


Figure 1.13: Transverse momentum distribution for charged hadrons. Data refer to different centrality hypothesis in Au-Au collisions: values of 0 – 5% indicate a truly central event, while values of the order of 80 – 92% represent a peripheral collision.

- BRAHMS is a spectrometer for high rapidity particles (especially charged hadrons)

An interesting result was obtained by the PHENIX collaboration and subsequently confirmed by all other experiments:

Jet quenching: this QGP signature shows up through high p_T particles suppression. Figure 1.13 shows p_T distributions for charged hadrons in different ranges of centrality: the yield of particles grows with increasing centrality. *Hard processes* at high p_T occur in the interaction between single partons and are expected to scale with the number of nucleon-nucleon collisions. Besides, *soft processes* ($p_T \ll 2$ GeV) should be considered: they scale with the number of participating nucleons and produce the bulk of charged particles in pp or pA interactions. With increasing collision energy, the contribution of the hard component of the spectrum becomes more and more important.

To test jet quenching a nuclear modification parameter R_{AA} is defined which represents the number of measured particles, normalized to the number of parti-

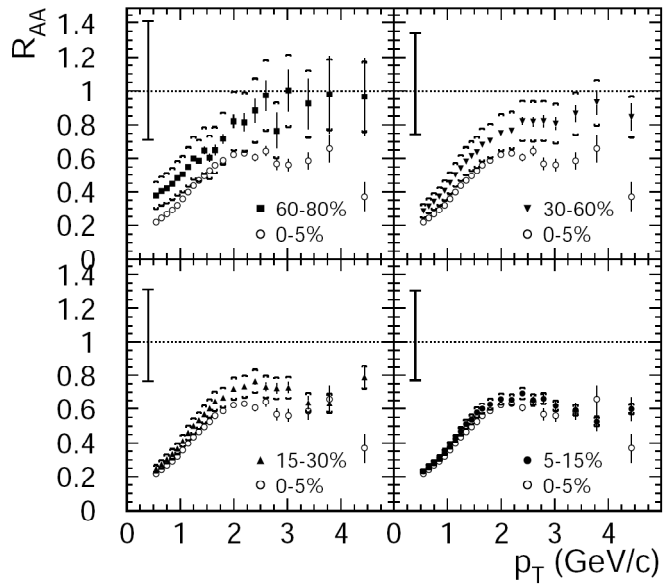


Figure 1.14: Nuclear modification factor R_{AA} in different centrality conditions. Data are referred to the highest centrality sample (0 – 5%).

cles expected to be produced in the case of incoherent nucleon-nucleon collisions:

$$R_{AA}(p_T) = \frac{\left(\frac{dN}{dp_T}\right)_{AA}}{N_{coll.} \left(\frac{dN}{dp_T}\right)_{pp}} \quad (1.23)$$

The value of R_{AA} at high p_T (where hard processes dominate) brings information about nuclear effects on particle production:

- $R_{AA} = 1$: the reaction is the result of incoherent binary reactions (no nuclear effect)
- $R_{AA} > 1$: the particle yield is enhanced with respect to the binary scale (Cronin effect [14] observed in pA collisions)
- $R_{AA} < 1$: indicates a suppression in hadron production at high p_T . This effect can be interpreted as a reaction between particles and deconfined matter and represents the phenomenon of jet quenching.

Figure 1.14 shows the values obtained for the ratio R_{AA} : even considering the enhancement due to the Cronin effect, the value at high p_T is still less than unity. For low transverse momenta ($p_T < 2\text{ GeV}$) this result is obvious since

particle yield scales with the number of participants; while for higher momenta the experimental data do not accord to the prediction of binary collisions and are compatible with jet quenching.

Flow: Radial and elliptic flow values show a good accord with models based on hydrodynamical evolution of a *perfect fluid*. A perfect fluid is a highly interacting system, which thermalizes in a very short time ($< 1 \text{ fm/c}$) and remains at equilibrium until thermal freeze-out.

1.5 Conclusions

To establish experimentally the collective properties of hot and dense matter created in nucleus-nucleus collisions, both systematic and luminosity problematics have to be taken into account. An efficiently designed experiment aims firstly at accumulating sufficient integrated luminosity in heavy nuclei collisions, to measure rare processes such as charmonia and jet transverse-energy spectra up to $\sim 100 \text{ GeV}$ and the pattern of medium induced modifications of bound states. Besides, the interpretation of experimental data relies considerably on a systematic comparison with the same observables measured in proton-proton or proton-nucleus collisions as well as in collisions of lighter ions. In this way the phenomena truly indicative of the hot equilibrating matter can be separated from other contributions. Having the purpose of probing a possible phase transition and the formation of QGP, future accelerators and detectors have to address precise physics topics, such as:

- the study of global event features by measuring multiplicity distributions and inclusive particle spectra
- mass measurements for heavy-flavour states with a very good resolution to improve the signal to background ratio in the study of heavy-quarkonia suppression (J/Ψ and Υ)
- improved momentum resolution to enhance the performance in the observation of jet production and jet quenching

Next chapter introduces the ALICE experiment at LHC (CERN), designed to cope with all these experimental requirements.

Bibliography

- [1] H. R. Schmidth and J. Schukraft, *The physics of ultra-relativistic heavy-ion collisions*
J. Phys. G: Nucl. Part. Phys. **19** (1993) 1705-1795
- [2] J. Schukraft (CERN), J. Stachel (Germany), *Nucleus-Nucleus Collisions and the Phase Transitions of Nuclear Matter*,
NuPECC Report-(97/12, rec. Mar. 98) 55-57
- [3] R. Hagedorn, Suppl. Nuovo Cimento **3** (1965) 147
- [4] J. Kaputsa, Phys. Rev. **D23** (1981) 2444
- [5] B. Müller, *Particle Production in Highly Excited Matter*, Ed. by Gutbrod and J. Rafelski, NATO ASI Series B: Physics, Vol. 303 (Plenum Press, N.Y., 1993)
- [6] E. Crescio, *Phd Thesis*, University of Torino 2001
- [7] E. Bruna, *Identificazione di particelle nell'esperimento ALICE mediante rivelatori di tracciamento*, Master Degree Thesis 2002
- [8] ALICE Physics Performance Report, Volume I-II
- [9] T. Matsui and H. Satz, Phys. Lett. **B 178** (1986) 416
- [10] B. Müller and X.-N. Wang, Phys. Rev. Lett. **68** (1992) 408
- [11] K. Kinder-Geiger, Phys. Rev. **D 48** (1993) 4129
- [12] G. Goldhaber, S. Goldhaber, W. Lee and A.Pais, Phys. Rev. **120** (1960) 300
- [13] M. J. Tannenbaum, *Recent results in relativistic heavy ion collisions: from "a new state of matter" to the "perfect fluid"*, arXiv:nucl-ex/0603003 v2 28 Jul 2006
- [14] E. Fermi, Phys. Rev. **81** (1951) 683
- [15] S. S. Balenki and L. D. Landau, Suppl. Nuovo Cimento **3** (1956) 15

- [16] PHENIX Collaboration, Phys. Rev. Lett. **88** (2002) 022301
- [17] NA50 collaboration, *A new mesurement of J/Ψ suppression in Pb-Pb collisions at 158 GeV per nucleon*, arXiv:hep-ex/0412036 v1 14 Dec 2004

Chapter 2

The ALICE experiment

ALICE (A Large Ion Collider Experiment) is a general purpose heavy-ion experiment designed to study the physics of strongly interacting matter and the quark-gluon plasma in nucleus-nucleus collisions at the LHC (CERN). It will start operating in 2007 with cosmic rays and in 2008 with first pp collisions at $\sqrt{s} = 900$ GeV. The experiment was approved in February 1997 and the detailed design of the different detector systems has been laid down between 1998 and the end of 2001. The design strategy and the detector optimizations are very different from the ones chosen for dedicated pp experiments (ATLAS, CMS, LHCb). ALICE's detectors can measure and identify mid-rapidity hadrons, leptons and photons produced in the interaction. Furthermore they allow tracking and identification of particles from very low (~ 100 MeV/c) up to fairly high (~ 100 GeV/c) transverse momenta, the reconstruction of short lived particles such as hyperons, D and B mesons. The detectors of the central barrel are designed to perform these tasks in an environment with large charged-particles multiplicities (up to 8000 particles per rapidity unit at mid-rapidity). Besides, a muon spectrometer measures the heavy-quark resonances spectrum and identify J/Ψ and Υ , Υ' and Υ'' particles. Production rates and decay geometry impose an acceptance which covers the full azimuth and more than one unit in rapidity. The features of ALICE experiment will be considered in section 2, with a particular attention to its Inner Tracking System (section 3), while section 1 introduces LHC Accelerator.

2.1 A Large Hadron Collider (LHC)

2.1.1 General considerations

The experimental programme at the LHC addresses one of the central problems of today's high energy physics: the connection between phase transitions involving elementary quantum fields, fundamental symmetries of nature and the origin of mass. The symmetry breaking mechanism should be faced considering

both symmetries of the dynamical laws of nature (which are described by the Lagrangian) and symmetries of the physical state with respect to which these dynamical laws are evaluated. LHC addresses both aspects through complementary experimental approaches. ATLAS and CMS experiments will search for the Higgs particle, which is made responsible for the spontaneous breaking of electroweak gauge symmetry and the generation of masses. LHCb focuses its attention on precision measurements with heavy b quarks and studies CP-symmetry violating processes. ALICE will investigate equilibrium and non-equilibrium physics of strong interacting matter, parton densities close to the phase-space saturation and their collective dynamical evolution towards hadronization in a dense nuclear environment, hoping to gain further insight into the structure of QCD phase diagram and QGP phase. Moreover, all LHC experiments are expected to have an impact on various astrophysical fields.

Standard pp collisions will be performed with a $\sqrt{s} = 14$ TeV, a beam energy of 7 TeV per nucleon (2808 bunches of $1.1 \cdot 10^{11}$ particles) and a luminosity of $\sim 5 \cdot 10^{30} \text{ cm}^{-2}\text{s}^{-1}$. In Pb-Pb collisions, a nucleon-nucleon center of mass energy of 5.5 TeV will be attained (exceeding that available at RHIC of a factor about 30), thus opening up a completely new scenario:

- *Initial conditions:* the heavy-ion programme accesses a wider range of Bjorken- x values if compared to RHIC and SPS (figure 2.1). In particular ALICE probes a continuous range of x as low as 10^{-5} attaining a regime where gluon shadowing is expected. Moreover the energy density will be $\epsilon \sim 500 \text{ GeV/fm}^3$ compared to the value estimated for RHIC of only $\epsilon \sim 35 \text{ GeV/fm}^3$. The number of charged particles produced is expected to be between 1100 and 8000 per rapidity unit. Of these events nearly 2 – 3% correspond to the most central collisions¹ (about 10^7 central events/year). Besides the estimated luminosity will be $\sim 10^{27} \text{ cm}^{-2}\text{s}^{-1}$.
- *Baryon density:* the central regions are expected to have $\mu_B \sim 0$ thus allowing the analysis of very different regions of the phase diagram.
- *Hard processes:* very hard strongly interacting probes are produced at sufficiently high rates for detailed measurements, especially through their attenuation in the medium in the early stages of the collision. In particular high p_t jets, heavy quarks, J/Ψ and Υ . Also photons, Z and W bosons are produced in hard processes and, since they do not have strong interactions with the colored medium, they provide informations about nuclear parton distributions at high Q^2 .
- *Event-by-event analysis:* it becomes a precision instrument at high particle multiplicity. Besides, due to the large number of secondaries produced, it will be possible to measure, on an event-by-event basis, different observables like impact parameter, dN/dy , particle ratios, p_t spectra, size and

¹For example 1.6 % of the events has an impact parameter $b < 2 \text{ fm}$, while 5 % has $b < 3.5 \text{ fm}$.

lifetime from interferometry. Each event can be treated as a thermodynamical system and variables such as flow or chemical composition of the final state will be measured with good precision.

- *Fireball expansion* and in general the collective features of the final state will be dominated by parton dynamics. The ratio of the lifetime of QGP to the time for thermalization is expected to be an order of magnitude larger than at RHIC.

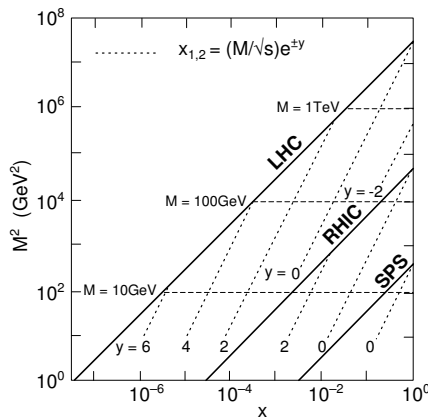


Figure 2.1: *The range of Bjorken x and M^2 in nucleus-nucleus collisions for SPS, RHIC and LHC. Lines of constant rapidity are shown.*

2.1.2 ALICE running strategy

A systematic study of different collision systems (pp , pA , $A - A$) will be performed at LHC at different beam energies. Each year the collider will start its operations with several months of pp running (10^7 s effective time), followed by several weeks of heavy-ion collisions (10^6 s) at the end of the year. Thus ALICE will take its first data with pp collisions because of LCH commissioning, but also because pp physics is an integral part of its programme (section 1.5). The initial ALICE programme is summarized below:

- LHC commissioning run at $\sqrt{s} = 900$ GeV
- regular pp runs at $\sqrt{s} = 14$ TeV
- initial heavy-ion programme
- Pb-Pb physics pilot run
- 1-2 years Pb-Pb

Table 2.1: *LHC machine parameters for pp and Pb–Pb runs for ALICE.*

	pp	Pb–Pb
Energy per nucleon (TeV)	7	2.76
β at the IP: β^* (m)	10	0.5
r.m.s. beam radius at IP: σ_t (μm)	71 ^a	15.9
r.m.s. bunch length: σ_l (cm)	7.7	7.7
Vertical crossing half-angle (μrad)		
for pos. (neg.) μ -spectr. dipole polarisation	150 (150)	150 (100)
Number of bunches	2808	592
Bunch spacing (ns)	24.95	99.8
Initial number of particles per bunch	1.1×10^{11}	7.0×10^7
Initial luminosity ($\text{cm}^{-2}\text{s}^{-1}$)	$< 5 \times 10^{30}$	10^{27} ^b

^aFor low-intensity runs β^* could be 0.5 m and $\sigma_t = 15.9 \mu\text{m}$ as in Pb–Pb.

^bEarly operation will be with 62 bunches and $\beta^* = 1$ m, which yields an initial luminosity of $5.4 \times 10^{25} \text{ cm}^{-2}\text{s}^{-1}$.

- 1 year pPb-like collisions (pPb, dPb or α Pb)
- 1-2 years Ar-Ar

At the end of the first year of operation LHC is expected to perform the first Pb–Pb collisions at a total center-of-mass energy of 1148 TeV , corresponding to 5.5 TeV per nucleon. Luminosity will reach values between $3 \times 10^{31} \text{ cm}^{-2}\text{s}^{-1}$ for light ions (^{16}O) and $1 \times 10^{27} \text{ cm}^{-2}\text{s}^{-1}$ for Pb ions. Table 2.1 quotes the most significative machine parameters for *pp* and Pb–Pb runs for ALICE.

2.2 The ALICE experiment

With the ALICE experiment, all the observables involved in the study of QGP formation, in Pb–Pb collisions, will become accessible. More specifically:

- global event features (multiplicities, pseudo-rapidity distributions)
- particle ratios and transverse-momentum distributions
- elliptic flow
- cross-section of high transverse momentum hadrons
- strangeness production
- open heavy flavours (D and B mesons) and quarkonia (J/Ψ and Υ families)
- prompt photons and lepton pairs
- multiplicity fluctuations

- particle correlation

In addition, proton-proton collisions are considered as an integrating part of the programme since they:

- contribute to pp physics in a new energy and energy-density domain
- provide pp data as a reference for ion-ion collisions
- provide low multiplicity data to commission and calibrate the various detector-systems
- contribute to precision measurements of the underlying characteristics of events in other LHC experiments (since ALICE acceptance at low p_T is a unique feature among all LHC experiments)
- improve models used for cosmic ray interactions at the highest energies

2.2.1 Design requirements from specific physics topics

Acceptance is defined as the ratio between particles *accepted* within the volume of the detector, and those effectively produced in the event. To attain higher acceptance values, detectors like ALICE are designed to cover the complete ϕ angle range. The range of pseudo-rapidity depends on the detector's position in the global structure of the experiment. A coverage of about two units of rapidity and adequate azimuthal coverage are required in order to detect the decay products of low-momentum particles and to collect a statistically significant sample of J/Ψ and Υ in the dielectron channel. Furthermore a good acceptance is required for an event-by-event analysis, where the sensitivity for single event observables is proportional to $\sqrt{\Delta y \times \Delta \phi}$ (y and ϕ are the rapidity and the azimuthal angle). Central detectors cover $|\eta| < 0.9$ and full azimuth, but to gain in sensitivity on the global event structure, charged-particle multiplicity will be measured in a larger rapidity domain ($-3.4 < \eta < 5.1$). Moreover a ϕ symmetry is desirable in order to check the azimuthal dependence of eventual non-statistical structures or collective flows.

Tracking relies on a set of high granularity detectors using mostly three-dimensional hit information and continuous tracking with many points in a moderate magnetic field. The ideal choice for the magnetic field should be 0.2 T to maximize hadron reconstruction efficiency, and 0.5 T for high p_t observables. Since the latter are limited in statistics, ALICE will run at the higher field for the majority of time.

Momentum cut-off should be imposed according to the following considerations: in the study of collective effects associated with large length scales ² cut-off should be as low as possible (< 100 MeV/c). Besides, a low p_t cut-off is also mandatory to reject the soft conversion and Dalitz background in the lepton-pair

²By the *uncertainty principle*, collective effects that occur over distances of $1 - 10$ fm are associated with small momenta (20 – 200 MeV/c).

spectrum (for example the electromagnetic decay $\pi^0 \rightarrow e^+e^-\gamma$) and in identical particle interferometry. At high momenta, resolution requirements are determined by measurements of jet spectra; while at intermediate momenta mass resolution should be of the order of the natural width of ω and ϕ , in order to maximize the signal-to-background ratio and to study mass and width of these mesons in a dense medium.

Finally the detection of hyperons, D and B mesons requires a high resolution vertex detector close to the beam pipe.

Particle Identification of hadrons with full acceptance and 3σ resolving power is provided in the central part of ALICE detector, up to momenta $p_t \leq 2.5$ GeV/c. Such an high precision is needed to measure HBT correlations, to identify hyperons and vector mesons and heavy-flavour mesons through their hadronic decay and to measure particle ratios on an event-by-event basis. Instead, at higher momenta a reduced acceptance and resolving power (3σ) will be sufficient to reconstruct particle ratios and p_t spectra with a statistical approach.

A good e/π rejection is needed in order to reduce the electron-pair combinatorial background (due to misidentified pions) below the level of unrejected Dalitz pairs. Besides it must be extended to high transverse momenta in order to identify electrons from Υ decays.

A high granularity and resolution calorimeter, covering the central rapidity zone, is needed in order to detect direct photons from the early stages of the collision, since they will be measured in a crowded background of decay photons. At $p_t < 10$ GeV/c the main source of systematic error is the accuracy in the reconstruction of neutral mesons (π^0 and η which subsequently decay in photons). A reasonable systematic uncertainty can be obtained if the channel occupancy of the calorimeter is low, which means a small *Molière radius*³ at about 5 m from the vertex.

Finally, for the study of J/Ψ , Ψ' , Υ , Υ' and Υ'' states, a muon spectrometer has been designed. The signal from vector meson decay in $\mu^+\mu^-$ will appear superimposed on a continuum due to D and B meson decays and Drell-Yan processes. The LHC environment prevents muon identification below momentum values of 4 GeV/c [2], so the rapidity coverage is chosen to be $-4.0 \leq \eta \leq -2.4$, corresponding to a region where muons are Lorentz boosted. Besides, a hadron absorber must shield the chambers from the high hadron multiplicity generated in a heavy ion collision and from secondary particles generated in the beam-pipe. The absorber material has to be selected to limit muon scattering in order to preserve the mass resolution needed to resolve the various states.

A final consideration on the data-acquisition system should be made: it will

³The Molière radius is defined as a function of the radiation length of the material X_0 and of its atomic number Z :

$$R_M = 0.0265 X_0 (Z + 1.2)$$

and is a good scaling variable in describing transverse dimensions of electromagnetic showers.

have to cope with an unprecedented data rate, especially due to the large data volume from high granularity tracking detectors. An overall data flow of about 1.25 GB/s is expected, depending on online data reduction, event size and trigger selectivity and composition.

2.2.2 Experimental Layout

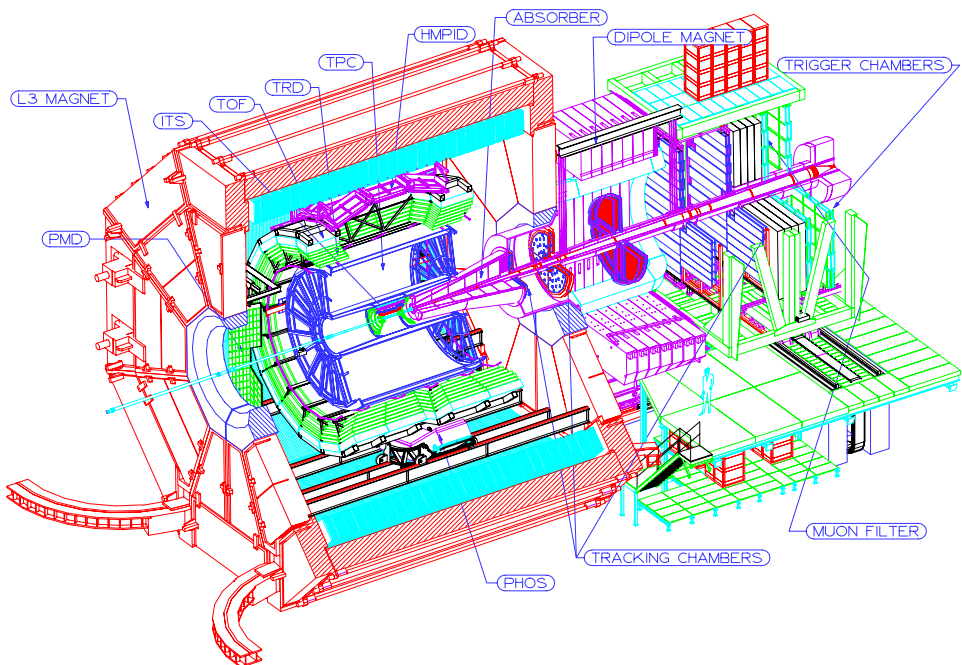


Figure 2.2: *Longitudinal view of the ALICE detector.*

The ALICE detector is housed in an underground cavern 40 m below ground level at the interaction point 2 of the LHC accelerator. At the top of the cavern special buildings are situated in order to supervise detector operations (control room) or to house part of the electronics (four floors of counting rooms, separated from the experiment cavern by a concrete shielding plug). Other services such as gas system, electricity, cooling and ventilation are distributed from the corresponding service buildings at the surface and by racks located on the cavern floor and along the cavern walls. In particular the ventilation system circulates 20000 m³/h of air through the cavern under normal operating conditions and keeps it at a temperature to within $\pm 2^\circ$ C at a relative humidity of $\sim 50\%$.

Magnetic Field

The central part of the detector is enclosed in a solenoid magnet originally built for the L3 experiment at LEP. The internal length of the magnet is 12 m and the radius is 5 m. The nominal field of the solenoid is 0.5 T and the field variations in the volume of the detectors (up to 2.5 m in radius and ± 2.5 m along the axis from the centre for the TPC) are below 2%. The choice of the magnetic field represents a compromise between momentum resolution, low momentum acceptance and tracking efficiency. Low momentum tracks resolution is governed by multiple scattering and its contribution to the relative momentum error is:

$$\left(\frac{\Delta p}{p} \right)_{MS} \propto \frac{1}{B \times l} \quad (2.1)$$

while the contribution from the resolution in the position measurement is:

$$\left(\frac{\Delta p}{p} \right)_{meas.} \propto \frac{1}{B \times l^2} \quad (2.2)$$

where B is the magnetic field and l the tracking length (its value is chosen to be rather large, $l = 2.5$ m, in order to reduce the uncertainty). So in a low magnetic field track finding will result more performing, especially at small momenta since the track curvature is smaller. The choice of tracking over a large distance is suitable for full tracking and particle identification down to $p_t \sim 200$ MeV/c; for lower momenta track reconstruction is committed to the ITS. The presence of a magnetic field implies a p_T cut-off:

$$p_{T,cut-off} = 0.3 B R = 200 \text{ MeV}/c \quad (2.3)$$

for a magnetic field $B = 0.5$ T and trajectories with a curvature radius $R = 1.25$ m (to have enough track points in the TPC).

Support structures inside the solenoid are produced from non-magnetic materials, either stainless-steel or aluminium, to avoid distortions of the magnetic field.

Moreover a large warm dipole magnet with resistive coils and horizontal field perpendicular to the beam axis is used for the muon spectrometer; the field integral in the forward direction is 3 T m.

Vacuum pipe

The vacuum pipe is a beryllium tube 0.8 mm thick with an outer diameter of 59.6 mm extending 0.4 m and 3.5 m from the interaction point towards the muon spectrometer and the opposite side respectively. Outside this region it is a stainless-steel (muon spectrometer direction) or copper (other direction) tube.

2.2.3 Detectors

A crucial feature in the design of ALICE is connected with the low interaction rate, which allows to use slow (but high granularity) sensors such as time-projection chambers or silicon drift detectors. The ALICE layout is showed in

figure 2.2 and consists of a central detector system and several forward systems. The *central system* covers mid-rapidity ($|\eta| \leq 0.9$) over the full azimuth and is located inside a large solenoidal magnet. It includes, from the interaction vertex to the outside:

- **Inner Tracking System (ITS):** composed by six layers of high resolution silicon detectors (it will be discussed in the next section).
- **Time-Projection Chamber (TPC):** the main tracking detector of the experiment. It measures charged-particle momenta with good two-track separation, performs particle identification and vertex determination (together with the ITS). The TPC allows the analysis of hadronic and leptonic signals for p_t up to 100 GeV/c and can track up to 20000 charged particles per event.
The TPC has a cylindrical design with an inner radius of 90 cm, given by the maximum acceptable hit density of 0.1 cm^{-2} , and an outer radius of 250 cm dictated by the requirement of a dE/dx resolution $< 10\%$ (necessary for electron identification). The overall length in the beam direction is 500 cm. The selection of materials was influenced by the need to reduce multiple scattering: for the counting gas a light mixture of Ne (90%) and CO_2 (10%) was chosen and particular attention was devoted to the choice of other materials composing the structure of the detector.
The read-out chambers cover the two end-caps of the TPC cylinder and are conventional multiwire proportional chambers with cathode pad readout.
- **Transition-Radiation Detector (TRD):** complementing ITS, TPC and TOF capability for electron identification. It consists of six layers of radiator foil stacks followed by Time Expansion Chambers, providing a e/π rejection power of 100 in high multiplicity operation. Besides, the fast tracking capability of the detector is useful to trigger on high p_t leptons.
- **Time of Flight (TOF):** is a hadron identification array in the intermediate momentum range from 0.2 to 2.5 GeV/c (where the majority of produced charged particles are emitted), allowing the study of the dynamical evolution of the system. The TOF detector is positioned at $r = 3.7$ m. Technically the array is composed of multigap resistive plate chambers (MRPC) since a large area has to be covered and the only possibility is to choose gaseous detectors. RPC detectors have resistive electrodes which quench the streamers, preventing spark breakdowns and allowing higher gains if compared to the proportional regime; a multigap RPC is made of a series of gas gaps with a single set of readout strips reading out all gaps in parallel. A key aspect of this configuration is that the electric field is high and uniform over the whole sensitive volume and the signal is the analog sum of signals from many gaps, resulting in a peak well separated from zero. A resolution of ~ 150 ps is expected, a fact that would guarantee a 3σ K/π separation up to $p_{3\sigma} = 1.7$ GeV/c.

Furthermore, the central system is complemented by two specialized detectors covering a limited region of azimuthal angle:

- **High-Momentum Particle Identification Detector (HMPID):** consisting of an array of ring-imaging Cherenkov (RICH) detectors with $|\eta| \leq 0.6$ and 57.6° of azimuthal coverage. The HMPID is positioned at a distance of about 4.5 m from the beam axis and uses a C_6F_{14} radiator and a MWPC with pad readout for detecting ultraviolet photons. The RICH is expected to extend the 3σ limit of K/π separation to ~ 3.4 GeV/c.
- **Photon Spectrometer (PHOS):** is an electromagnetic calorimeter consisting of an array of high density crystals. The rapidity coverage is $|\eta| \leq 0.12$ and the azimuthal coverage is 100° . It will be located at 5 m vertically beneath the interaction region and will be made of $PbWO_4$, a material with small Molière radius and high light output. The PHOS will provide photon identification as well as neutral mesons identification through the 2-photon decay channel, requiring high granularity and good energy and spatial resolution. The occupancy must not exceed 3%.
- **Electromagnetic calorimeter (EMCal):** it is an upgrade proposed to complete the mid-rapidity capabilities of ALICE [1]. It has been designed to measure the neutral portion of jet energy over a wide acceptance and to provide an efficient and unbiased fast trigger for high energy jets. It is a large Pb-scintillator sampling calorimeter with cylindrical geometry, located adjacent to the ALICE magnet coil. Its rapidity coverage is $|\eta| \leq 0.7$ and its azimuthal coverage is 110° .

The *large rapidity system* includes:

- **Muon Spectrometer:** covering $-4.0 \leq \eta \leq -2.4$. It consists of a composite absorber ($\sim 10\lambda_{INT}$) located at about 1 m from the interaction point to reduce the background due to π and K decays. The absorber is designed to maximize hadron absorption without introducing too much muon multiple scattering with layers of both high and low Z materials. The absorber is followed by a dipole magnet which accepts muons at angles smaller than 9° . A small angle absorber with a central hole will shield the angles from 0° to 2° and allow the non-interacting Pb ions to traverse the spectrometer. Tracking information will be provided by ten planes of multiwire proportional chambers with cathode pad readout. Finally the muons will be identified as the particles crossing a second absorber ($\sim 10\lambda_{INT}$) at the end of the spectrometer, and revealed by two resistive plate chamber planes (which also trigger the spectrometer).
- **Photon Multiplicity Detector (PMD):** is a preshower detector that measures the multiplicity and spatial distribution of photons on an event-by-event basis. It is situated in the forward region of ALICE (on the opposite side of the solenoid with respect to the muon spectrometer) in order to extend the η coverage of the central barrel for $dN/d\eta$ measurements.

This detector addresses physics issues related to single event fluctuations and flow and provides estimates of transverse electromagnetic energy. The PMD consists of two identical planes of detectors with a $3X_0$ thick lead converter between them. The front detector plane rejects charged-particle hits, while the detector plane behind the converter is the preshower plane. The detector technology is a gas proportional counter with honeycomb structure and wire readout, designed to meet the following requirements: minimize the shower transverse spread, avoid cross-talk among adjacent channels, be insensitive to neutrons, confine charged particles to one cell and cover large areas.

- **Foward Multiplicity Detector (FMD):** is an array of silicon strip detectors covering the large rapidity region up to $\eta = 5.1$. The system consists of 51200 silicon strips channels distributed over 5 ring counters formed by 20 or 40 sectors in azimuthal angle. Each sector is read out independently and contains 512 or 256 detector strips at constant radius. This detector will allow the study of multiplicity fluctuations on an event-by-event basis and flow analysis relying on the azimuthal segmentation in the considered pseudo-rapidity range.
- **Trigger detectors (T0, V0):** a system of scintillators and quartz counters, providing fast trigger signals.
- **Zero-Degree Calorimeter (ZDC):** is composed by two sets of neutron and hadron calorimeters, located at 0° at about 90 m away from the interaction vertex. It will allow the measurement of the impact parameter.

Trigger System

ALICE will have a pre-trigger signal, three levels of trigger with a fixed latency (L0, L1 and L2) and a high-level trigger (HLT).

The pre-trigger is based on T0 and V0 detectors and it is used to switch TRD electronics on. The signal is generated in less than 100 ns after the collision.

L0 trigger signals an interaction at the earliest possible time (after about 1.2 μs). It is not a very selective trigger and runs at a rate up to a few times 10^4 Hz depending on the beam type. It can be used to strobe the detector front-end electronics.

L1 trigger leads to a considerable reduction in the rate (< 1000 Hz); its latency is 5.5 μs . With this trigger level, all the remaining detectors will be strobed and L1 can be used by the data acquisition system to allow readout to start from the detector front-end electronics.

L2 trigger is used to avoid pile-up events. It has a latency of about 88 μs and more selective algorithms can be applied, provided they are completed in less than 100 μs corresponding to the TPC drift time.

Besides, data from the central barrel detectors will be used to generate a fast online High-Level-Trigger (HLT) for the selection of low cross-section signals.

In ion-ion collisions, event pile-up is not tolerable, due to the considerable multiplicities. So the trigger system must ensure that for each sub-detector no other event occurs during the read-out or drift time of the detector, either before or after the event of interest. This period has been chosen to be $200\ \mu\text{s}$, considering that the slowest detector is the TPC, which has a drift time of $100\ \mu\text{s}$. Moreover, the trigger system should operate also in proton-proton mode. In this case it has to select minimum bias events, with the possibility to define a *priority stream* of rare event types (for example dimuons).

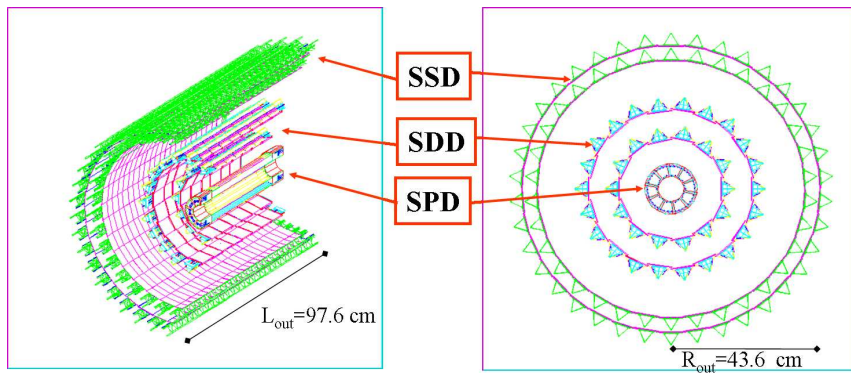
2.3 The Inner Tracking System

The Inner Tracking System is composed by six cylindrical layers of bidimensional silicon detectors, covering the rapidity range of $|\eta| < 0.9$ for all vertices situated in the *interaction diamond* ($\pm 1\sigma$) of 10.6 cm along the beam direction. Its design has been studied to provide secondary vertex reconstruction for hyperon and charmed meson decays, tracking and identification by species of low p_t particles and optimal momentum resolution for the higher p_t particles. The number, position and segmentation of the layers are optimized for efficient track finding and high impact parameter⁴ resolution. Since a resolution below $100\ \mu\text{m}$ for the impact parameter is required from the ALICE experimental strategy, and considering the high particle density in a Pb-Pb collision (up to 80 particles per cm^2), silicon detectors are the most suitable choice for sensors in the ITS. In particular, pixel technology (SPDs) has been chosen for the innermost two layers, silicon drift detectors (SDDs) for the following two and double-sided microstrip detectors (SSDs) for the outermost two layers (where track densities are below 1 particle per cm^2). Microstrip and drift detectors will have analog readout to allow particle identification via dE/dx measurements in the $1/\beta^2$ region (section 3.1), giving to the ITS a stand-alone capability as a low p_t particle spectrometer.

2.3.1 Design considerations

The study of all physics topics addressed by the ALICE experiment (section 1.2.1), depends in a crucial way from the ITS particle identification and tracking capabilities, since low momentum particles ($p_t \sim 100\ \text{MeV}/c$) are detectable only by the ITS. A particular attention should be given to angular resolution, essential for the measurement of primary vertex position and of the first points of a track, which is expected to be 1 mrad. The accuracy of the measurement depends on precision, position and thickness (because of multiple scattering) of the first layers. The ITS design has been optimized to enable the identification, on a statistical basis, of displaced secondary vertices of charm and beauty mesons and the identification of hyperons on a track-by-track basis (via impact

⁴In this case the impact parameter is defined as the minimum distance between a given trajectory and the primary vertex.

Figure 2.3: *Layout of the ITS.*

parameter measurements); furthermore a good double track resolution will allow the measurement of large radii with particle interferometry.

The specific tasks of the ITS are summarized below:

- to localize the primary vertex with a resolution better than $100 \mu\text{m}$, depending on the number of tracks used to estimate it
- to reconstruct the secondary vertices from decays of hyperons and D and B mesons
- to track and identify particles with momentum below 200 MeV, to suppress the background in the electron-pair analysis
- to improve the momentum and angle resolution for the high p_t particles ($p_t > 100 \text{ MeV}/c$). A tracking efficiency of 90% is required to have a sufficient statistics in a single event for event-by-event analysis and for rare or large background signals
- to reconstruct, even if with limited momentum resolution, particles traversing dead regions of the TPC.

The choice of detector technology for the ITS was dictated by several requirements such as granularity, spatial resolution and energy loss measurements. The following factors were taken into account:

Geometry

The six layers of silicon detectors are located at radii of 4, 7, 15, 24, 39 and 44 cm respectively. The inner radius is the minimum allowed by the extention of the beam pipe ($r = 3 \text{ cm}$). The pseudo-rapidity coverage of the first layer is extended with respect to the other layers ($|\eta| < 1.98$) to provide a continuous coverage, together with FMD, for charged-particle multiplicity measurements.

The outer radius is determined by the necessity to match tracks with those from the TPC (whose inner radius is fixed at 84.1 cm by the maximum acceptable occupancy).

The acceptance should allow the study, on event-by-event basis, of particle ratios, transverse momentum spectra, particle correlations and the decay of large mass and low transverse momentum particles. Besides, an efficient rejection of low-mass Dalitz decays can only be implemented if the detector provides full azimuthal coverage.

Spatial resolution and granularity

The spatial precision of the ITS is a key element in the momentum resolution of decay products of charmed mesons and high mass quarkonia, and in general for momenta larger than 3 GeV/c. Particularly the resolution of the impact parameter measurement, determined by the spatial resolution of the detectors, is significant in the reconstruction of charmed and beauty decays, where it has to be $\leq 100 \mu\text{m}$ in the $r\phi$ plane. ITS detectors have a spatial resolution of the order of a few tens of micron, with the best precision of $12 \mu\text{m}$ for the SPD (closest to the primary vertex), as shown in table 2.4. For the SSD the double-sided technology has been preferred to the single-sided one in order to minimize the material and to exploit the correlation of the pulse heights readout from the two sides to recognize the ghost hits caused by the projective readout. ITS resolution in the bending plane is about one order of magnitude better than that of the TPC, which in turn provides many more points.

Impositions on granularity come from the requirement of low detector occupancy, which is strictly linked to the fact that the ITS would detect simultaneously more than 15000 tracks (the maximum theoretically predicted track density is 8000 tracks per unit of rapidity). The occupancy must be of the order of a few percent, resulting in several millions of effective cells in each layer of the ITS.

dE/dx reconstruction

For the study of specific energy loss all detectors should have analog readout. Unfortunately in the case of SPD this requirement could not be met because of technological difficulties and excessive costs of fabrication.

Material budget

The amount of material in the active area of the ITS should be reduced at minimum, since the resolution on track parameters for small- p_t particles is strongly influenced by multiple scattering. The maximum thickness allowed for silicon detectors used to measure ionization densities (SDDs and SSDs) is $300 \mu\text{m}$, in order to provide a reasonable signal-to-noise ratio. Furthermore, detectors should overlap to cover the entire solid angle. Considering the incidence angle of tracks, the effective thickness of detectors amounts to 0.4% of X_0 for each

Table 2.2: *ITS material budget traversed by straight tracks perpendicularly to the detector surface. Units are percentages of radiation length.*

Detector	Pixel		Drift		Strip	
	Inner	Outer	Inner	Outer	Inner	Outer
Layer	1.0	1.0	1.1	1.1	0.81	0.83
Thermal shield/Support		0.36	0.29		0.42	
Total				7.0		

layer, while the effect of additional material in the active volume (electronics, cabling, support and cooling system) is limited to a comparable effective thickness. The material budget of the 6 ITS layers is summarized in table 2.2 and amounts to $\sim 7\%$ of an interaction length.

Radiation levels

Components used in the ITS were tested for their radiation hardness to levels exceeding significantly the expected dose. Namely the total dose received during the entire duration of the experiment ranges from a few krad⁵ (tens of Gy) for the outer parts to about 220 krad (2.2 kGy) for the inner parts. These values are low, but still enough to justify the use of radiation-tolerant design for the front-end electronics; otherwise the enhancement of the leakage current would lead to an excessive power consumption.

Readout rate

The ALICE system would exploit two different readout configurations, operated simultaneously with two different triggers. The readout of the whole experiment will be activated by a *centrality trigger* (the second level trigger L2 for the central barrel) operating at a rate of about 25 Hz, while a subset of fast readout detectors will be governed by the *dimuon trigger* at a rate of about 1 kHz. In the second case it is necessary to acquire data from the two ITS inner layers in order to reconstruct the primary vertex and reach the required mass resolution on dimuon signals. For this reason, the two layers of SPD need a readout faster than 400 μ s.

Table 2.3: Dimensions of the ITS detectors (active areas).

Layer	Type	r (cm)	$\pm z$ (cm)	Area (m^2)
1	pixel	3.9	14.1	0.07
2	pixel	7.6	14.1	0.14
3	drift	15.0	22.2	0.42
4	drift	23.9	29.7	0.89
5	strip	37.8/38.4	43.1	2.09
6	strip	42.8/43.4	48.9	2.68
Total area				6.28
Layer	Ladders	Lad./stave	Det./ladder	Channels
1	80	4	1	3 276 800
2	160	4	1	6 553 600
3	14	—	6	43 008
4	22	—	8	90 112
5	34	—	22	1 148 928
6	38	—	25	1 459 200

Table 2.4: Parameters of the various detector types. A module represents a single sensor element.

Parameter		Silicon Pixel	Silicon Drift	Silicon Strip
Spatial precision $r\varphi$	(μm)	12	38	20
Spatial precision z	(μm)	100	28	830
Two track resolution $r\varphi$	(μm)	100	200	300
Two track resolution z	(μm)	850	600	2400
Cell size	(μm^2)	50×425	150×300	95×40000
Active area per module	(mm^2)	12.8×69.6	72.5×75.3	73×40
Readout channels per module		40 960	2×256	2×768
Total number of modules		240	260	1698
Total number of readout channels	(k)	9 835	133	2608
Total number of cells	(M)	9.84	23	2.6
Average occupancy (inner layer)	(%)	2.1	2.5	4
Average occupancy (outer layer)	(%)	0.6	1.0	3.3
Power dissipation in barrel	(W)	1500	1060	1100
Power dissipation end-cap	(W)	500	1750	1500

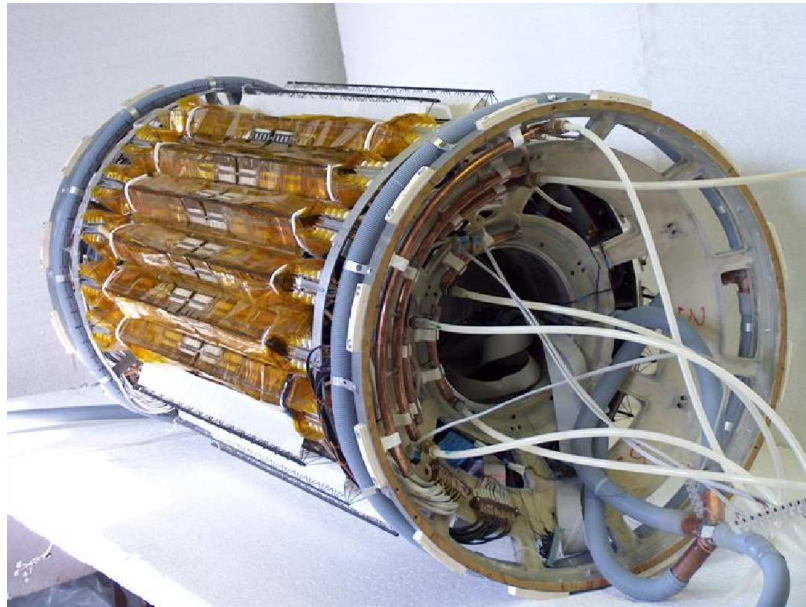


Figure 2.4: Prototype of the ITS SDDs with all detectors and the cooling system.

2.3.2 Experimental layout

The six cylindrical layers of silicon detectors of the ITS are held by lightweight carbon-fibre structures, since both silicon and carbon-fibre have little impact on multiple scattering. Detector dimensions and parameters are listed in tables 2.3 and 2.4.

The large number of readout channels of the modules requires a huge number of connections between detectors, front-end electronics and readout. The use of conventional copper cables near the active surfaces of the detectors is not allowed from the requirement of minimum material within the acceptance; thus Tape Automatic Bonded (TAB) aluminium-polyamide microcables are used (with a thickness of $12 - 20 \mu\text{m}$ except for the $400 \mu\text{m}$ thick high voltage cable). All the ITS front-end electronics is made up of ASICs implemented in a commercial $0.25 \mu\text{m}$ CMOS technology, using radiation-tolerant layout techniques developed at CERN. All the six layers have extra support electronics at their extremities devoted to voltage regulation, readout control, zero suppression and interfacing

⁵The *rad* measures the quantity of radiation absorbed and depends on the energy deposited in a body of mass 1 Kg, according to:

$$1\text{rad} = 0.01\text{jouleKg}^{-1} = 6.24 \times 10^{10} \text{MeVKg}^{-1}$$

Alternatively the *gray* (Gy) is:

$$1\text{Gy} = 100\text{rad}$$

with external systems (data acquisition, trigger and slow detector control). Besides, ITS cooling system has been designed with a particular care due to the sensitivity of SDDs to temperature. Electronics hybrids cooling is performed with water circulating in specific pipes, while the detectors are cooled through a direct air flux.

Bibliography

- [1] ALICE Physics Performance Report, Volume I
- [2] E. Crescio, *Phd Thesis*, University of Torino 2001
- [3] Technical Design Report of the Inner Tracking System, ALICE Collaboration, CERN/LHCC 99-12
- [4] ALICE Collaboration, CERN-LHCC-2006-014, CERN/LHCC 96-32-Add3 (2006)

Chapter 3

Silicon Drift Detectors

3.1 An overview on Silicon Sensors

Silicon detectors have been used in almost all High-Energy or Nuclear Physics experiments in the last two decades. Their success has increased along with the progress of the technology of microelectronics and interconnections, which has had an impact both on the quality of the fabrication technology of the detectors and on the possibility of reading out detectors more and more complex in a faster way. The most commonly used configurations are silicon strip and pixel sensors. The underlying principle of operation of these detectors, as well as silicon drift sensors, is a reverse biased $n-p$ junction. The general characteristics of silicon sensors, independently from the specific detector type, are:

- response of the order of 10 ns
- spatial resolution of the order of 10 μm
- segmentability in any shape
- small amount of material (a typical thickness of 300 μm , corresponding to $0.003X_0$)
- excellent mechanical properties
- linearity of the response vs. deposited energy
- good resolution in the deposited energy (3.6 eV are needed to create a pair of charges, vs. 30 eV in a gas detector)
- tolerance to high radiation doses
- flexibility of design

These properties make silicon detectors excellent devices for both energy and position measurements. Besides, since the fabrication technology of such sensors is analogous to the one of integrated electronics circuits, detectors can be implemented with additional features (substrate resistors, capacitors, injectors).

3.1.1 Energy response

Silicon detectors are generally referred to as *linear detectors*, since they produce a signal that is proportional to the energy deposited in their volume. Besides, the energy required to produce a charge pair is very small, which translates in a very good ratio signal/energy-deposit. The signal released by a traversing particle in a thin silicon detector is usually small, so the possibility to profit of these features depends strongly on the noise of the read-out electronics connected to it. The energy resolution which can be achieved is given by the quadratic sum of two factors: the noise of the read-out chain (including the leakage current in the detector) and statistical fluctuations in the generation of charge carriers. For small signals the main source of electronic noise could be in the digitization phase, due to the quantization error introduced by the width of the lowest significant bit in the ADC.

In a low-energy regime almost all of the particle's energy is deposited in the detector volume and the resolution (σ) of the generated charge is the square root of the number of generated charges. The number of generated charges is E/δ , where E is the energy of the particle and δ the average energy needed for the creation of an electron-hole pair¹. In a high-energy regime particles traverse the detector exchanging a small fraction of their energy. For charged particles most of the energy loss is due to ionization; photons may lose their energy via photoelectric, Compton or pair production effect, depending on the energy range. Electrons lose most of their energy through bremsstrahlung, while for other relativistic particles the Bethe-Bloch formula [3] can be applied:

$$-\frac{dE}{dx} = K z^2 \frac{Z}{A} \frac{1}{\beta^2} \left[\frac{1}{2} \ln \left(\frac{2m_e c^2 \beta \gamma^2 T_{max}}{I^2} \right) - \beta^2 - \frac{\delta(\beta \gamma)}{2} \right] \quad (3.1)$$

where z is the charge of the incident particle, Z the atomic number of the medium, A the atomic mass of the medium, β and γ the kinematic variables of the incident particle and $m_e c^2$ the electron mass. The variable I is the mean excitation energy, T_{max} is the maximum kinetic energy which can be transferred to a free electron in one collision and δ is a density correction factor.

For low energies (β less than 1) the energy loss decreases as β^2 and after a minimum it grows slowly. Particles with energy above the so-called $1/\beta^2$ region are called minimum ionizing particles (MIPs). For a MIP, the statistical fluctuations in the energy deposited follow a distribution which is usually referred to as a Landau curve (even if it is a bit wider and physically much more complex).

3.1.2 Applications

Tracking is one of the most important applications of silicon detectors. Their linear energy response allows the possibility of improving the spatial resolution of these detectors which are segmented to a pitch comparable to the spatial

¹This expression should be multiplied by the Fano factor F (which ranges between 0 and 1, depending on the material) to take into account the fact that charges are not generated in a fully uncorrelated way.

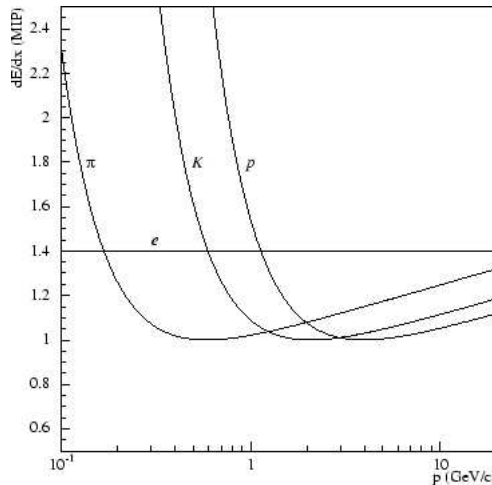


Figure 3.1: Energy loss as a function of the particle momentum.

spread of the collected charge. Charge is shared among several electrodes and the impact point of the particle is reconstructed as the centroid of the signals. If the noise is low, this method can achieve resolutions down to few microns. Besides, silicon detectors can be used for particle identification. From the Bethe-Bloch formula, it is clear that dE/dx depends on the particle velocity. Thus the knowledge of the particle momentum and of the energy released allows particle identification, if particle velocity is low ($1/\beta^2$ region of plot 3.1). Therefore a system of silicon detectors in a magnetic field can provide a full stand-alone spectrometer, measuring the trajectory of the particle, the momentum and the mass. What is normally done is to use a few measurements of energy deposition (for example in a tracking system each particle crosses several detector layers) to extract independent probabilities for a given particle identity and then to combine the results with a bayesian approach. Finally, silicon detectors can be used for spectroscopic measurements of low-energy X-rays in several applications in which spatial resolution and simple installation are important factors, namely for imaging detectors for medical diagnostics.

3.1.3 Radiation damage effects

Silicon detectors are generally exposed to high radiation environments, causing two well distinguished effects: *bulk* (or displacement) damage and *surface* damage. The first one is caused by the non-ionizing energy loss of the traversing particles and results in defects to the crystal lattice. The relevant variable is the fluence of particles through the detector, measured as particles per cm^2 . When the detector is exposed to a non-ionizing radiation, two macroscopic ef-

fects can affect its performance: leakage current increases and depletion voltage² changes. Physically, the energy transferred to the crystal by the traversing particles damages the lattice, creating interstitials or vacancies which can combine to form more stable defects. One of the prominent consequences is the build-up of negative space charge in the detector volume due to the introduction of deep energy levels. This effect can change the effective doping concentration, which is directly related to the detector depletion voltage. In n-type silicon the effective concentration initially decreases, until it crosses zero and then changes the sign of the effective doping (from n-type to p-type), generating the so-called *type inversion*. After type inversion the trend goes on, resulting in a continuous increase of the p-type doping. Thus high fluences of particles eventually cause an increase of the depletion voltage of the detector, demanding higher detector bias voltage, potentially up to a point at which it becomes impossible to fully deplete it. Nevertheless, inverted detectors can operate successfully as long as the power supplies are able to provide full depletion. The build-up of negative space charge continues also in the periods without irradiation (*reverse annealing*) and the only way to stop this phenomenon is to keep the detector at low temperature ($\sim -5^\circ \text{C}$).

The increase of leakage current is due to radiation induced generation centers. This effect scales linearly with received radiation fluence. A too high leakage current can limit detector performance, since it increases the noise of the readout system. The main remedies are a very fine segmentation of the detector (since current is a volume effect) and the operation at low temperature. Finally the last important bulk damage is the loss of charge collection efficiency due to charge trapping at fluences larger than 10^{14} cm^{-2} .

Surface damages consist in the ionization of the insulating oxide, resulting in the build-up of positive charge in the oxide itself and in the degradation of its quality. Furthermore, the ionising radiation can create new energy levels in the band gap at the Si/SiO₂ interface. Surface damage can potentially degrade the performance of the readout system.

3.2 SDDs underlying principles of operation

Among all the different types of silicon detectors, SDDs offer two-dimensional position reconstruction with a limited number of read-out channels, high granularity and a good multitrack capability, besides a large area coverage. For these reasons they are well adapted to the high multiplicity environment created by heavy-ion collisions at the LHC. They were proposed in the early eighties by Gatti and Rehak [4, 1]. The operating principle is based on the measurement of the time necessary for the electrons produced by the ionization of the crossing particle to drift from the generation point to the collecting anodes, by applying an adequate electrostatic field. A drift channel in the middle of the depleted bulk of a silicon wafer performs the transport of the electrons, in a direction

²The *depletion voltage* is the inverse biasing required by the p-n junction to extend the depletion region to the entire detector thickness.

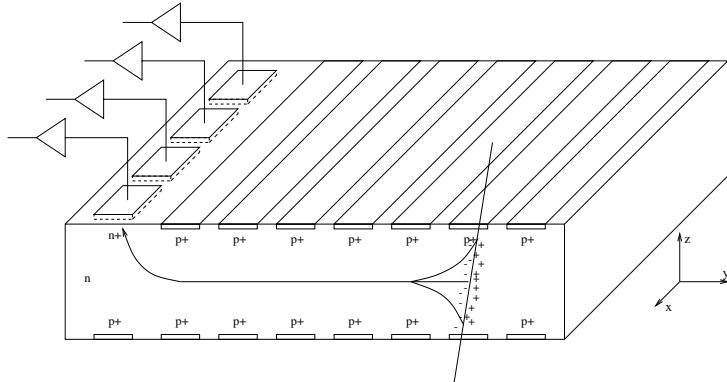


Figure 3.2: Principle of operation of a silicon drift detector.

parallel to the surface of the detector along distances of few centimetres. At the edge of the sensitive area electrons are collected by an array of small size anodes. The design of silicon drift detectors is dictated by two crucial requirements:

- the creation of a potential distribution within the silicon wafer able to focus the electrons from the generation point to the middle plane
- the creation of a drift field to transport the charge towards the anodes

So, the mean drift time of electrons, from the point where charge is generated to the anodes, provides the position along one direction, while the centroid of the charge collected by anodes gives the position along the other direction. Moreover the total collected charge represents an energy loss sample used for particle identification.

3.2.1 Focusing potential

The focusing of the electrons in the center of the detector is achieved by fully depleting a thin, large area silicon wafer through a small contact called *virtual electrode*. Specifically, two p^+ n junctions can be created with two n-doped silicon wafers of thickness w with one surface biased at ground with a n^+ contact and a p^+ implant on the other side (figure 3.3).

If the two junctions are reverse biased, in each wafer a depletion region of extension d is formed. The n^+ contacts of the two wafers may be joined without modifying their electrostatic condition.

The practical realization of this principle is to create two p^+ cathodes on a single wafer of thickness of w by placing the n^+ depletion contact at the edge of the wafer, still without modifying the potential distribution within the wafer. When the negative potential applied to the cathodes reaches a value V :

$$V = \frac{eN_D}{2\epsilon} \left(\frac{d}{2} \right)^2 \quad (3.2)$$

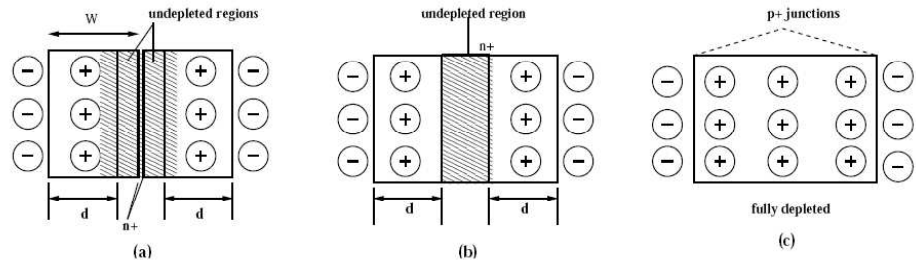


Figure 3.3: Double p^+n junction: not fully depleted (a), of a not fully depleted single semiconductor wafer with two p^+n junctions at the two sides (b) and fully depleted single semiconductor wafer with two p^+n junctions at the two sides (c).

the wafer is *fully depleted* and the potential distribution within its volume (figure 3.4) represents the solution of the one-dimensional Poisson's equation:

$$\frac{\partial^2 \phi_1}{\partial z^2} = -\frac{qN_D}{\epsilon} \quad (3.3)$$

where ϕ_1 is the electric potential, z is the direction along the wafer thickness as shown in figure 3.2, q is the electric charge, N_D the donor concentration and ϵ the dielectric constant of silicon. The solution of the above equation follows the parabolic profile:

$$\phi_1(z) = -\frac{qN_D}{\epsilon}(z - z_0)^2 + \phi_1^2 \quad (3.4)$$

where $z_0 = w/2$ is the middle plane of the wafer.

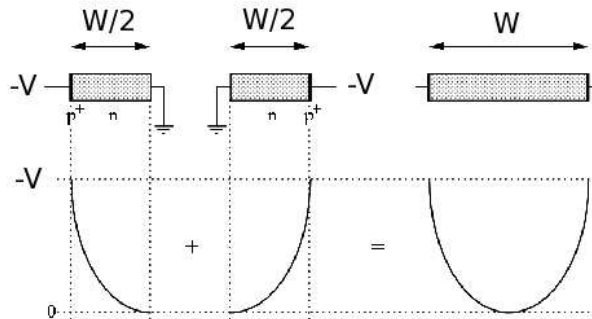


Figure 3.4: Parabolic profile of the potential distribution in a fully depleted junction with a p^+ cathode on each side.

3.2.2 Drift potential

The electrostatic field is constant along x and y directions³, since the potential $\phi_1(z)$ is a function of the z direction exclusively. A constant drift channel along the y direction, in the middle plane of the wafer, is created with the simple superimposition of an electrostatic field of components:

$$E_x(x, y, z) = 0 \quad (3.5)$$

$$E_y(x, y, z) = E_{DRIFT} \quad (3.6)$$

$$E_z(x, y, z) = 0 \quad (3.7)$$

E is governed by the equation:

$$E = -\nabla\phi_2 \quad (3.8)$$

with the solution:

$$\phi_2(x, y, z) = \phi_2(y) = -E_y + \phi_2^0 \quad (3.9)$$

and the potential ϕ_2 satisfies the Laplace's equation:

$$\frac{\partial^2 \phi_2}{\partial y^2} = 0 \quad (3.10)$$

Therefore, a bidimensional potential distribution is needed in order to meet the requirements for SDDs field design. The correct configuration is given by the sum of the two components $\phi_1(z)$ and $\phi_2(y)$, which satisfies the two-dimensional Poisson's equation:

$$\frac{\partial^2 \phi(y, z)}{\partial y^2} + \frac{\partial^2 \phi(y, z)}{\partial z^2} = \frac{\rho}{\epsilon} = -\frac{qN_D}{\epsilon} \quad (3.11)$$

With the imposition of linear boundary conditions, the potential ϕ can be expressed as:

$$\phi(y, w) = E_y + \phi_0 + \frac{w}{2} \frac{qN_D}{\epsilon} = -E_y + const. \quad (3.12)$$

where ϕ_0 is a constant. In this case a numerical solution to the two-dimensional Poisson's equation can be found (figure 3.5(a)), which has a characteristic *gutter shape*. This peculiar potential distribution focuses the electrons released by the crossing particle in the middle plane of the device and transports them towards the collecting regions.

3.2.3 Actual potential distribution

The linear potential boundary condition introduced in section 3.2.2 is not realistic, since the actual drift field is obtained by polarizing p^+ cathodes of finite

³As shown in figure 3.2, a cartesian system is used to describe the detector coordinates: x is the anodic direction, y is the drift direction and z is the direction perpendicular to the detector surface.

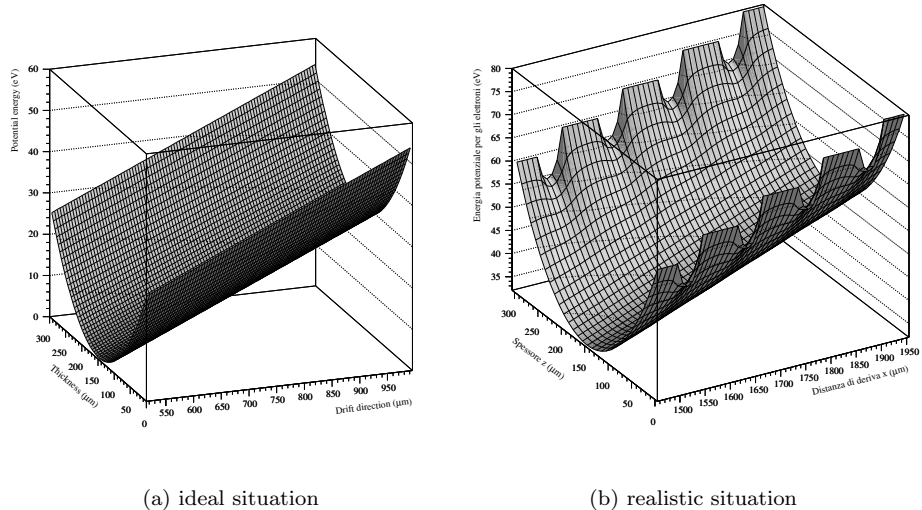


Figure 3.5: Numerical simulation of the potential distribution in the drift region of a silicon drift detector.

width h with negative voltages in proportion to their distance from the collecting region, as showed in figure 3.5(b) for a fully depleted detector. The discretization of the potential distribution near the detector surface differs considerably from the ideal case of superposition of two one-dimensional contributes. Between each pair of p^+ implants there is a parabolic decrease of the potential with a minimum whose depth depends on the polarization of the cathodes. This configuration, with a minimum potential between each couple of cathodes, guarantees electric isolation by preventing the possibility of a hole current passing between the strips, provided that they are polarized with the correct voltage. Besides, the cathodes polarization should be chosen in order to create a uniform drift field. The voltage between two strips with a pitch s is given by: $\Delta V = E \times s$, being E the drift field. A key requirement for an optimal performance of the drift field, is that the effect of discretization of cathodes shoud vanish in the middle plane of the wafer, where electrons drift. In this perspective the value of the strip pitch s should maintain an appropriate s/w ratio between s and the detector thickness w .

The numerical solution of Poisson's equation (eq. 3.11) gives the expected values for the electric field in the drift channel in the middle of the detector bulk. The results are shown in figure 3.6(a) as a function of the drift direction for four different values of $r = s/w$, maintaining a fixed and realistic value for s of $120 \mu\text{m}$ and variating the detector thickness. The field uniformity improves for lower values of r and a ratio $r \leq 0.4$ guarantees the deviation from uniformity of the field to be below 1% in the middle plane, similarly to the ideal case of

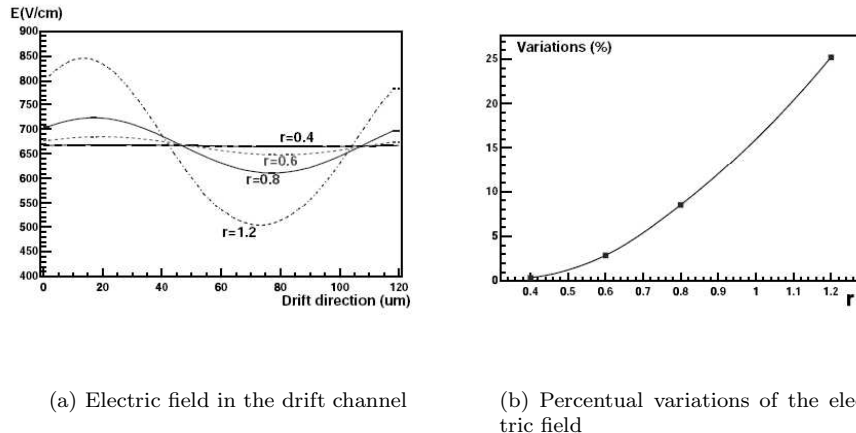


Figure 3.6: *Uniformity of electric field in the drift channel of a SDD for different values of the ratio r between cathode pitch and detector thickness.*

linear boundary conditions (figure 3.6(b)).

3.2.4 Collection zone

An example of potential simulation in the collection zone is shown in figure 3.7, where the effect of *kick-up* cathodes in front of the anodes is particularly evident. This configuration has been optimized to channel the drifting charge towards the anode array with the aid of a complex polarization scheme. In order to guide electrons from the middle plane towards the detector surface, a set of cathode strips is used on both faces of the wafer with carefully chosen voltages. Besides, it is necessary to avoid both the generation of non-depleted areas, which may block the electrons, and over-biasing (or under-biasing), which may drive the electrons to the surface far from the anodes, losing part of the signal.

3.3 Detector layout for the ALICE experiment

The ALICE SDDs are produced ⁴ from 300 μm thick silicon wafers characterized by a good homogeneity and high resistivity (3 k Ωcm). The required doping concentration is achieved by means of a neutron transmutation process (NTD) within the silicon isotope ^{30}Si and thermal neutrons, producing the phosphorus isotope ^{31}P [5]. The final SDD prototype ⁵ has a sensitive area of 70.17 \times 75.26 mm², corresponding to the 88% of the total detector area. It is split into

⁴The ALICE SDDs are produced by the *Canberra Semiconductors* (Olen, Belgium)

⁵The final prototype is the so called ALICE-D2, designed by the INFN DSI project starting from 1992.

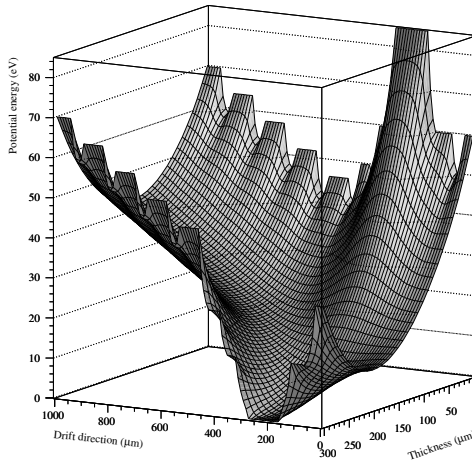


Figure 3.7: *Typical real potential distribution in the collection zone of a silicon drift detector (numerical simulation).*

two drift regions by a central cathode strip. Each drift region has 256 collection anodes with $294 \mu\text{m}$ pitch and 291 p⁺ cathode strips with $120 \mu\text{m}$ pitch (on both sides of the detector). Cathodes fully deplete the detector volume and generate a bidirectional drift field parallel to the wafer surface, causing the electrons to migrate from the middle of the detector towards the two linear arrays of anodes (figure 3.8). The drift field is achieved by gradually scaling cathode biasing down with a potential difference of 8 V between adjacent cathodes, corresponding to a drift field of about 670 V/cm. The drift time is sampled with 256 time bins of 25 ns, corresponding to a maximum allowable drift time of $6.4 \mu\text{s}$. Therefore, the minimum electron speed permitted to cross a half detector (35 mm) is about $5.5 \mu\text{m}/\text{ns}$. A drift field of 666 V/cm gives drift velocity at 20° C of about $8 \mu\text{m}/\text{ns}$, corresponding to a 8 V potential difference between adjacent cathodes. The maximum drift results to be about $4.4 \mu\text{s}$. In order to limit the HV value, a different configuration has been developed. It uses a potential difference between cathodes of 6 V/GAP, resulting in a drift field of about 500 V/cm. In this case the drift velocity is about $6 \mu\text{m}/\text{ns}$ and the maximum drift time results to be $\sim 5.8 \mu\text{s}$, which is acceptable because it is $< 6.4 \mu\text{s}$. During detector test measurements described in the followed chapters, a potential gap of 8 V between adjacent cathodes was chosen. In this way, due to the higher drift speed, the electron cloud dimension is reduced and the 256 time bins are not completely exploited. The required potential configuration is obtained with a set of integrated voltage dividers made of p⁺ resistive implants (170 kΩ each) connecting adjacent cathodes, a peculiar feature of ALICE SDDs

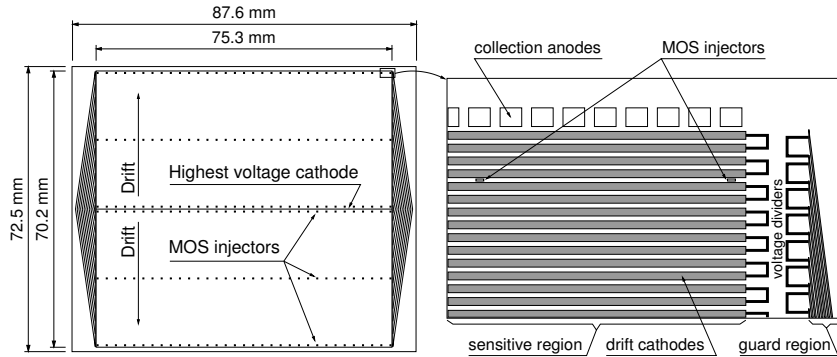


Figure 3.8: *Layout of the ALICE SDD. The sensitive area is split into two different regions by the central, highest voltage, cathode. Each drift region has one row of 256 collection anodes and three rows of 33 point-like MOS charge injectors for monitoring the drift velocity. Drift and guard regions have independent built-in voltage dividers.*

design. A medium voltage of -40 V is applied to cathode number 291. The central cathode should have a nominal high voltage biasing of -2368 V, resulting from the 291 gaps of 8 V between cathode 291 and the center of the detector. In the collection region a few cathodes closest to the anodes, pull-up cathodes, are externally biased to bring drifting charges efficiently from the middle plane of the detector towards the surface, where anodes collect them. These pull-up cathodes are called W1, W2 and W1. During detector testing the two W1 cathodes are biased at -64 V (like cathode 288), while the W2 cathode is biased at -80V (like cathode 286). In the case of polarization with 6 V/GAP a higher value of medium voltage (-45 V) is chosen, so as to have a high enough voltage on cathodes W1 and W2. Pull-up cathodes polarization should ensure the complete depletion of the collection region, therefore it depends on the wafer resistivity. The above voltages are referred to a resistivity of 3 k Ω cm. For higher values of resistivity lower biasing is required to fully deplete the same silicon thickness. Besides, the degrading of the high voltage to the zero potential of the detector boundary is implemented by two guard regions composed by 145 cathode strips with a 32 μ m pitch.

Furthermore, each drift region has three rows of point-like ($20 \times 100 \mu\text{m}^2$ for the metal gate) MOS charge injectors, which will be illustrated in paragraph 3.3.2.

3.3.1 Systematic effects

The reconstruction of particle impact point along drift coordinate could be affected by systematic deviations caused by:

- non-linearity of the integrated voltage divider

Table 3.1: *The main characteristics of the ALICE silicon drift detectors.*

Sensitive area	$70.17 \times 75.26 \text{ mm}^2$
Total area	$72.50 \times 87.59 \text{ mm}^2$
Collection anodes (readout channels)	2×256
Anode pitch	$294 \mu\text{m}$
Nominal operating voltage	-2.4 kV
Nominal bias of the collection region	-40 V
Nominal drift velocity	$8.1 \mu\text{m/ns}$
Nominal maximum drift time	$4.3 \mu\text{s}$
Cell size at nominal drift velocity	$294 \times 202 \mu\text{m}^2$
Cells per detector at nominal drift velocity	$2 \times 256 \times 174$
Total number of cells (260 SDDs)	$23.16 \cdot 10^6$
Average resolution along the drift ($r\varphi$)	$35 \mu\text{m}$
Average resolution along the anode (z)	$25 \mu\text{m}$
Detection efficiency	99.5%
Average double-track resolution at 70% efficiency	$700 \mu\text{m}$

- fluctuations of dopant concentrations

Non-linearity of the voltage divider

If the drift potential distribution is non-linear, the relationship between drift time and distance will consequently be non-linear. The phenomenon which could alter the linearity of the potential distribution is the *leakage current* (in its hole component) entering the cathode chain. The leakage current [6] is a dark current generated, both at the surface or in the depleted bulk, by lattice imperfections such as impurities or crystal damage from wafer processing, detector production or irradiation. Ideally the voltage drop between two adjacent cathodes is:

$$\Delta V = RI_{DIV} \quad (3.13)$$

where $I_{DIV} = V_{TOT}/(NR)$ is the current flowing in the divider, R the resistor value V_{TOT} the total potential and N the number of resistors. The voltage drop on a resistor n , when a hole current enters the cathode chain, is:

$$\Delta V_n = R(I'_{DIV} + ni_{PAR}) \quad (3.14)$$

with i_{PAR} the parasitic current on the cathode. The total potential can be written as:

$$V_{TOT} = NRI'_{DIV} + Ri_{PAR} \sum_{n=1}^N n \quad (3.15)$$

and for the total current flowing in the divider:

$$I'_{DIV} = \frac{V_{TOT}}{NR} - \frac{i_{PAR} \sum_{n=1}^N n}{n} = I_{DIV} - i_{PAR} \frac{N+1}{2} \quad (3.16)$$

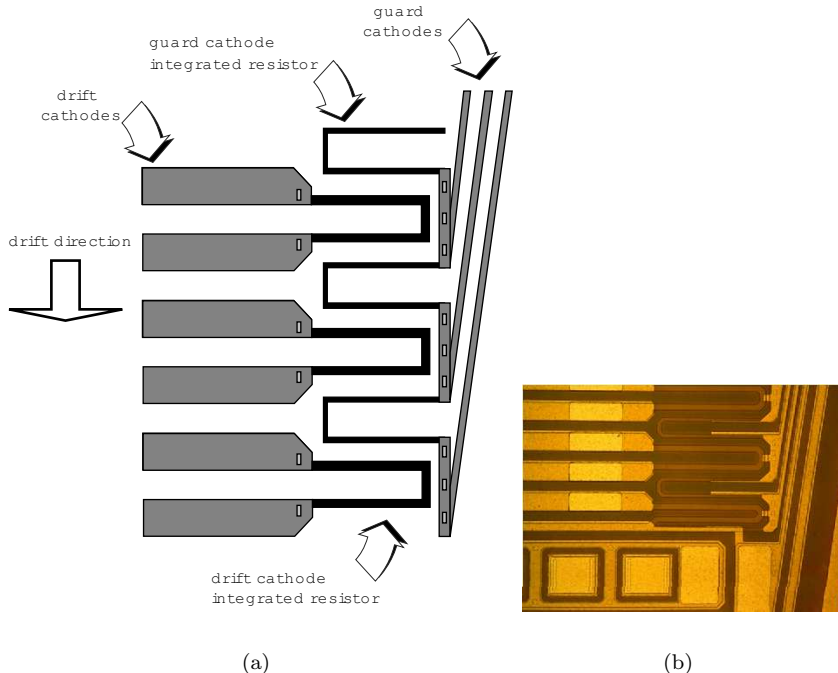


Figure 3.9: High voltage divider at the cathodes and guard region (a detail).

So the voltage on the cathode n results in:

$$\begin{aligned}
 V(n) &= \sum_{n'=1}^N R \left(I_{DIV} - i_{PAR} \frac{N+1}{2} + n' i_{PAR} \right) = \\
 &= V_{IDEAL}(n) - Ri_{PAR} \sum_{n'=1}^N \left(\frac{N+1}{2} - n' \right) = \\
 &= V_{IDEAL}(n) - Ri_{PAR} \frac{n(N-n)}{2}
 \end{aligned} \tag{3.17}$$

showing that the voltage drop between adjacent cathodes is no longer constant and the voltage on cathode n is expected to have a parabolic dependence on n . Unfortunately the real potential distribution is more complicated than a simple parabola, nevertheless the systematic error introduced by the non-linearity of the voltage divider could be corrected off-line using the results of detector laser mapping, as it will be explained in Chapter 6.

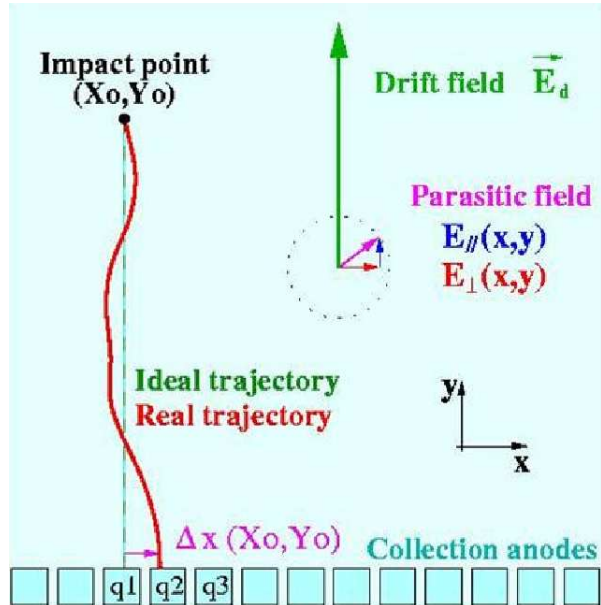


Figure 3.10: Effect of doping inhomogeneities on the particle trajectory.

Doping inhomogeneities

In SDDs, doping inhomogeneities affect the performance of the detector, since variations in the potential distribution cause a non-uniformity of the drift field along both the drift and the anode direction. The non-uniformity along the drift axis alters the proportionality between the drift time and the distance of the crossing point of the particle from the anode, introducing an uncertainty on the drift axis coordinate. On the other hand, the presence of parasitic transversal electric field in the wafer introduces deviations of the electron trajectories from the ideal linear path, introducing systematic errors in the determination of the x coordinate, as shown in figure 3.10.

Even though the NTD technique guarantees very good doping uniformity, it was found that the performance of the first ALICE SDD prototypes was affected by the systematic deviations of the electron trajectories produced by inhomogeneities [9]. For this reason, all modules produced for the SDD ladders have been tested with a laser to measure these systematic deviations, as it will be described in Chapter 6. Fortunately the effects of doping inhomogeneities are not present in the final prototype mounted on the ALICE ITS.

3.3.2 Mos charge injectors

An injection structure, capable to inject a controlled amount of charge in the detector bulk at a precisely known distance from the anodes, is a powerful

instrument to characterise and calibrate the detector. A MOS (Metal Oxide

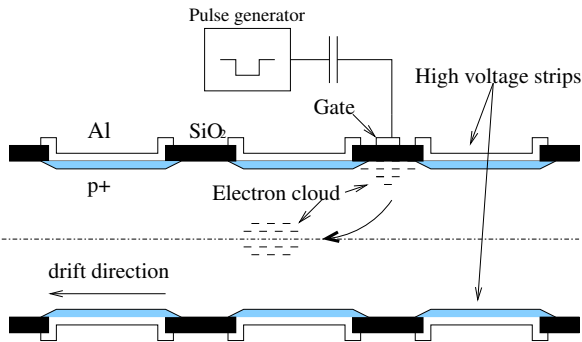


Figure 3.11: Principle of operation of the MOS charge injectors.

Semiconductor) structure can be used as an electron injector by exploiting the electrons which can be accumulated in the potential *pocket* below the oxide, created by the positive oxide charge. By applying a negative pulse to the metal gate, the electrons can overcome the potential saddle point and be injected in the silicon bulk [7]. The operating principle of MOS charge injectors is showed in figure 3.11.

A p^+ implant runs below the metal and the oxide in order to prevent the formation of the electron accumulation layer; in fact this is allowed only in certain areas where the p^+ implant is interrupted. These rectangular areas constitute the real injectors. The metal gate is $100\ \mu m$ long and $20\ \mu m$ wide. The first and last injector of each row are placed in such a way that they inject charge in the divider region, where power dissipation (and hence temperature) are expected to be higher with respect to the rest of the sensitive area, in order to allow an evaluation of the possible drift time differences. In the final detector design the three injector rows are placed at 3.225 , 17.625 and 34.425 mm from the anodes. The use of such devices in drift velocity calibration will be dealed in Chapter 6.

3.4 Readout electronics

Three ASICs implement the SDD front-end electronics: PASCAL, AMBRA and CARLOS. They have been designed using a radiation-tolerant layout technique based on a commercial deep-submicron process ($0.25\ \mu m$).

PASCAL is assembled on the front-end hybrid and has three functional blocks: preamplifier, analog storage and Analog-to-Digital Converter (ADC). The transimpedance preamplifier has a peaking time of about 40 ns, which has been chosen according to the following considerations: it must be long enough to have at least five samples for the evaluation of the time centroid, in order to ensure the resolution required by ALICE. On the other hand, a too long shaping time would affect the two track separation. The preamplifier dynamic range is

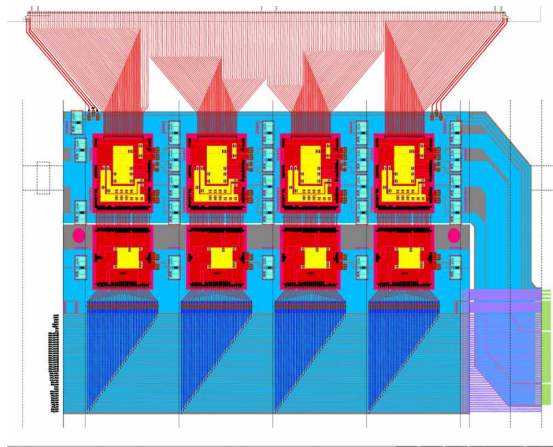


Figure 3.12: *Schematic representation of a SDD hybrid: the 4 pairs of PASCAL and AMBRA are shown. The upper part of the figure represents the connections with detector anodes.*

32 fC, since simulation results show that particles having a probability > 20% of being reconstructed produce anode signals ranging from 8 times the charge released by a MIP near the anodes (8×4 fC) down to a small fraction of the charge released by a MIP far from the anodes. Besides, a signal to noise ratio of at least 10 should be ensured for the smallest signal of interest, in order to achieve the spatial precision and the efficiency required. The signal to noise ratio decreases with increasing distance of the crossing point from the anodes, thus its value can be critical in the signal tail, especially in the anode direction. The chosen goal for the r.m.s. noise is 0.04 fC, corresponding to about 250 electrons. AMBRA chip is also assembled on the hybrid. It is a digital four-event buffer performing data derandomisation and transition to CARLOS chip, which is a zero-suppressor and data-compressor mounted on the end-ladder boards. Each PASCAL/AMBRA pair manages the signals from 64 anodes, resulting in 4 couples of chips in each hybrid, as shown in figure 3.12. The signal generated by an anode feeds the PASCAL preamplifier, then the amplifier output is sampled at 40.08 MHz by an analog ring memory with 256 cells per anode. When a L0 trigger is received, the cells are freezed and their contents are digitised (in about 230 μ s) by a set of 10-bit linear successive-approximation ADCs, which write the data in one of the free AMBRA buffers. AMBRA derandomizes the events and implements a 10-bit to 8-bit data compression. When an L2 trigger is received, all the AMBRAs transmit the data in parallel to the CARLOS chips on the end-ladder in 1.24 ms. CARLOS chips then reduce the SDD raw event size (22.1 MB) by more than one order of magnitude by suppressing the zeros. The advantages of a front-end A/D conversion are:

- noise immunity during signal transmission

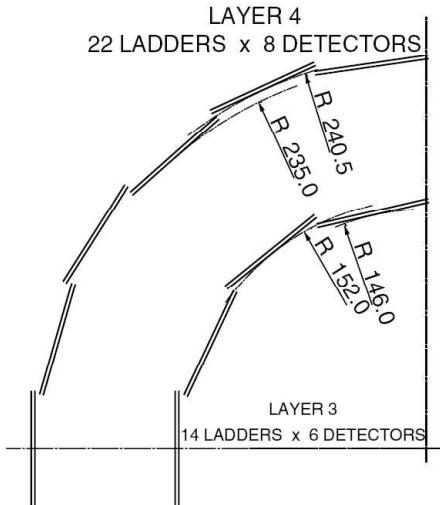


Figure 3.13: *The SDD are mounted at different radii in both r_z and $r\phi$ planes to obtain the full coverage in the acceptance region (units are millimetres).*

- possibility of inserting a multi-event buffer to derandomise data and to slow down the transfer rate to the DAQ system

Furthermore, the three ASICs embody a JTAG standard interface, in order to allow full testability at the board and system levels.

The readout architecture was designed in order to minimize cabling, due to the low space available on the ladders. Besides, ALICE requirements impose the use of very light structures, limiting the use of cooling systems. Therefore, since SDDs are very sensitive to temperature variations, power consumption should be kept at very low levels. Each PASCAL/AMBRA channel is estimated to have an average power dissipation of about 6 mW.

3.5 Silicon Drift layers

The Silicon Drift Detectors will equip Layer 3 and Layer 4 of the ITS, where the charged particle density is expected to reach 7 cm^{-2} . They have a very good multitrack capability and provide two out of the four dE/dx samples needed for the ITS particle identification. SDDs are mounted on linear structures called *ladders*. There are 14 ladders with 6 detectors on Layer 3 and 22 ladders with 8 detectors on Layer 4 (260 detectors as total). This structures are assembled to have an overlap of the sensitive regions larger than $580 \mu\text{m}$ in both $r\phi$ and z directions. This ensures full angular coverage for vertices located in the inter-

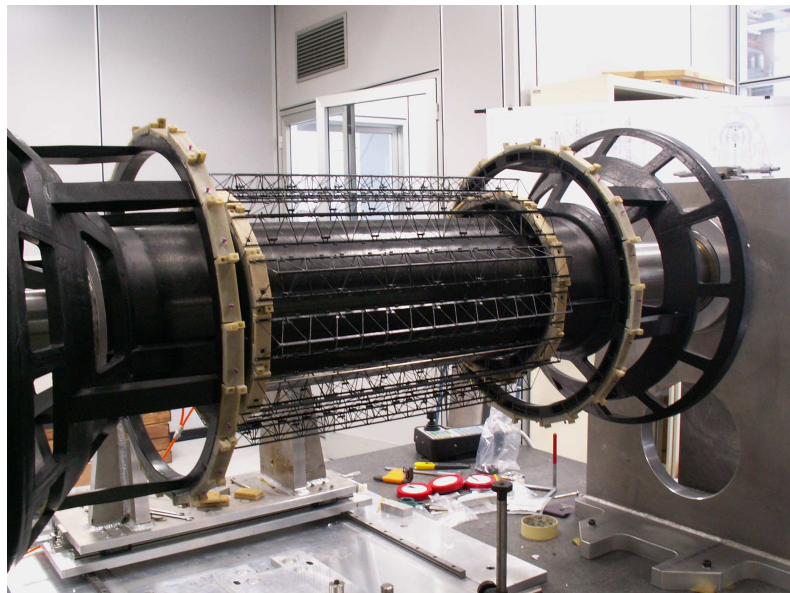


Figure 3.14: *Support structure of the SDD ladders (with a layer of ladders already mounted).*

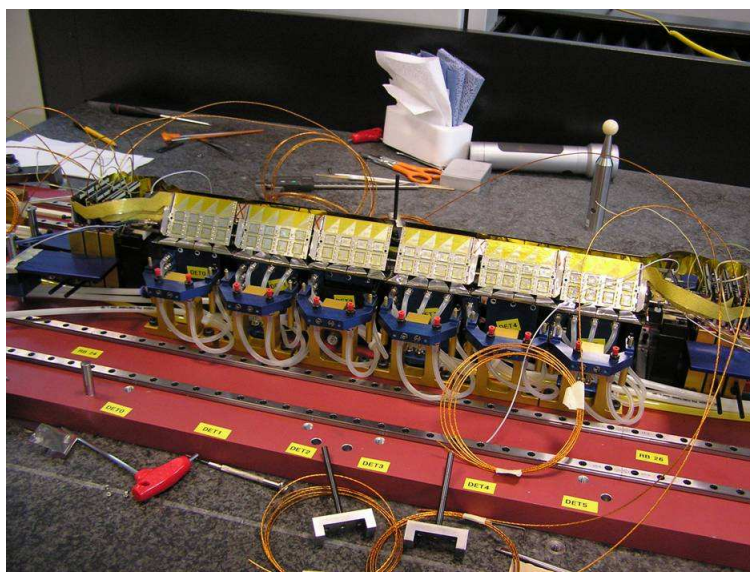


Figure 3.15: *Detector module mounted on a ladder: the front-end boards are shown folded to the two sides of the structure. Microcables are not shown.*

action diamond.

The ladder space-frame is a lightweight triangular truss made of Carbon-Fibre Reinforced Plastic (CFRP) and has a protective coating against humidity absorption. The same material has been used for the structure sustaining the ladders, which is composed by a cylinder, two cones and four support rings (picture 3.14). The cones provide the links to the outer SSD barrel and have windows for the passage of the SSD services. Detectors are attached to the space-frame using ryton pins with their anode rows parallel to the ladder longitudinal (z) axis.

The front-end electronics is assembled on two *hybrid circuits*, one per anode row, glued on rigid carbon fibre heat exchangers clipped to the cooling pipes running along the ladder structure. The coolant is demineralised water. End-ladder boards provide the interface between the SDD module and the external sub-systems such as data acquisition (DAQ), trigger, Detector Control System (DCS) and low and high voltage supplies. Each hybrid circuit has its own low-voltage board, carrying the rad-hard low voltage regulators, the Low Voltage Differential Signalling (LVDS) signal-receivers and the interface with the DCS. Each detector has its own high voltage board, containing the filtering of the high voltage bias, the drivers of the MOS injector lines and an external voltage divider.

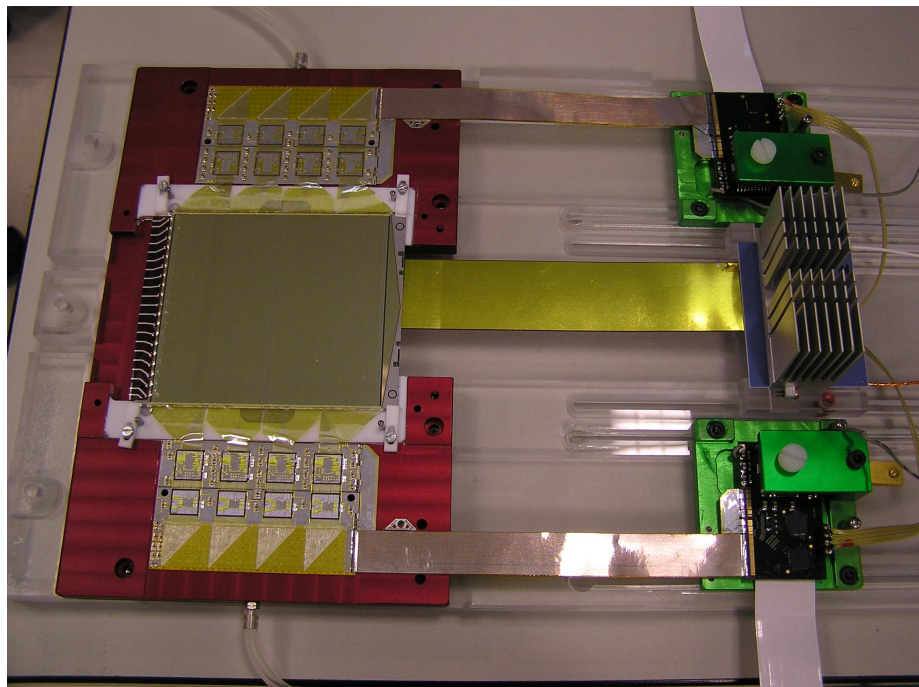
Each detector has been first assembled with its front-end electronics, the high-voltage connections and the related end-ladder boards as a unit, called *module*. Before its mounting on the ladder every module has been fully tested.

Table 3.2: *The main parameters of the ALICE SDD layers and ladders.*

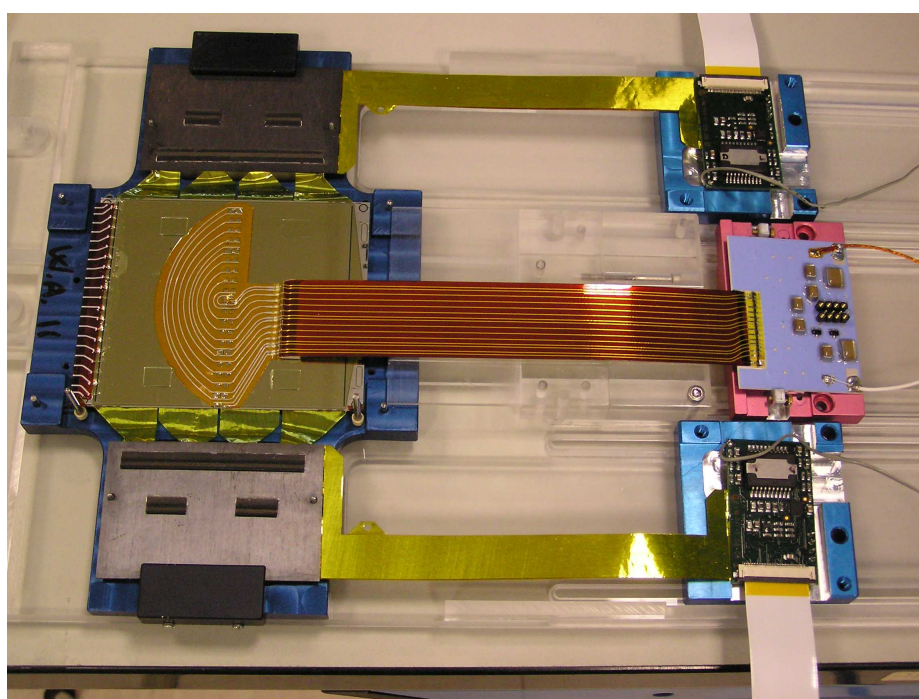
	layer 3	layer 4
Detectors per ladder	6	8
Ladders per layer	14	22
Detectors per layer	84	176
Ladder sensitive half-length (cm)	22.16	29.64
Ladder length (cm)	45.56	60.52
Average layer radius (cm)	15.03	23.91
Ladder space-frame weight (g)	11	15
Weight of ladder components (g)	87	121

3.5.1 SDDs modules

The SDD module is the basic building element of the SDD subsystem in the ITS frame. The hybrid circuits, which hold the front-end chips, are connected to the detector anodes through microcables. Each hybrid is connected to a LV card, placed in the end-ladder, providing individual power supply regulation and signal interfacing to the data-reduction electronics. Low voltage (LV) cables carry the A/D converted signal to the LV cards at the end-ladder. High voltage (HV) is supplied through a specific HV cable, which connects the detector to an



(a) upperside



(b) underside

Figure 3.16: *The SSD module.*

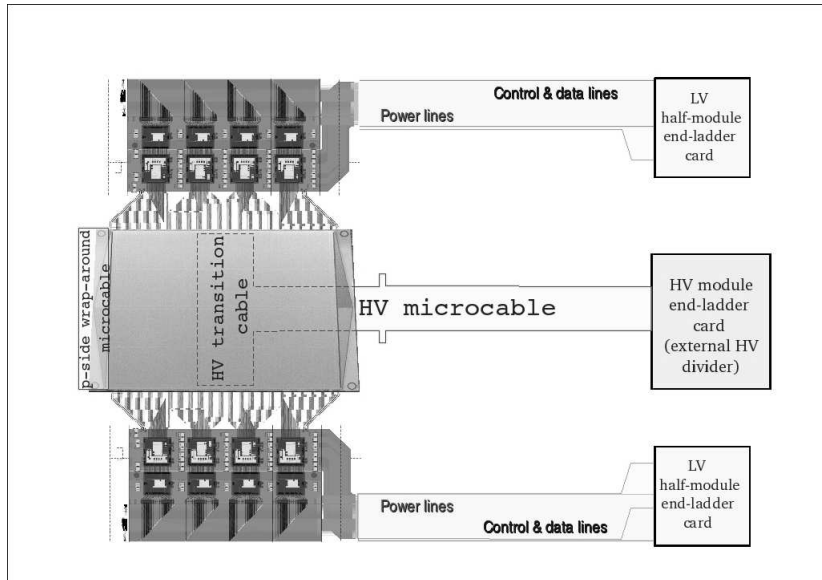


Figure 3.17: *Schematic layout of a SDD front-end module.*

HV card and carries the signals for the injectors. An external voltage divider is placed on the HV card, which bias some cathodes to specific reference voltages through the so called *transition cable*, placed on the underside detector surface. A *wrap-around cable* carries cathodes biasing from one side of the detector to the other. Injector pulses are generated from JFET devices placed on the LV cards⁶. Figure 3.17 shows schematically the layout of a front-end module. The full testing of modules will be analyzed in Chapter 6.

⁶LV card and HV cards are connected via pins, which are visible in figure 3.16(b).

Bibliography

- [1] P. Giubellino, E. Crescio et al., *Silicon detectors*, AIP Conference Proceedings **536** (2000) 35
- [2] *Review of Particle Physics*, Journal of Physics G: Nuclear and Particle Physics, Volume 33 July 2006
- [3] E. Gatti, P. Rehak, Nucl. Instr. and Meth. **A 225** (1984) 608
- [4] P. Rehak et al., Nucl. Instr. and Meth. **A 235** (1985) 224
- [5] E. W. Haas, M. S. Schnöller, *Phosphorus Doping of Silicon by Means of Neutron Irradiation*, IEEE Trans. Electron Devices, vol. ed-23, no. 8, August 1976
- [6] C. Piemonte, A. Rashevsky, D. Nouais, ALICE-INT-00-09
- [7] V. Bonvicini, P. Burger et al., *Characterising large area silicon drift detectors with MOS injectors*, Il Nuovo Cimento **112 A** (1999) n.1-2
- [8] ALICE Physics Performance Report, Volume I
- [9] E. Crescio, *Phd Thesis*, University of Torino 2001
- [10] Technical Design Report of the Inner Tracking System, ALICE Collaboration, CERN/LHCC 99-12

Chapter 4

Experimental system

4.1 Introduction

As discussed in Chapter 3, the SDD spatial resolution can be affected by two main systematic errors. The first one is the fluctuation of the effective doping concentration in the silicon crystal, introducing electrical parasitic fields which deviate the electrons from their straight trajectory towards the anodes. The second effect is the non-linearity of the voltage divider, which gives a non-linearity of the drift field and thus of the drift time as a function of the drift distance. Beam tests [2] performed at CERN have shown that errors as large as $700 \mu\text{m}$ can affect the reconstructed position of the impact point. Therefore, since the position resolution required by the ALICE experiment is $30 \mu\text{m}$, systematic errors on position measurements due to these effects must be corrected. The dopant concentration and the characteristics of the voltage divider can in principle be measured once and then used to correct the data during the off-line analysis, since it has been demonstrated that these quantities are stable in time. A laser mapping consists in the generation of charges with a laser on precisely known spots on the detector surface, in order to estimate the difference between the measured positions and the real ones. In the period from May to December 2006 about 300 SDDs have been laser-scanned in order to test them and extract the *map of deviations*. The mapping system has been conceived in order to meet the following requirements:

- simplicity (short development time, simple analysis and reliability)
- short scan time (since several SDDs had to be mapped)
- systematic effects negligible with respect to the detector required resolution of $30 \mu\text{m}$

This chapter describes the experimental system used to test and extract the deviation map of SDDs, which was also employed in the study of electron cloud diffusion inside the detector (as it will be discussed in Chapter 5). The laser

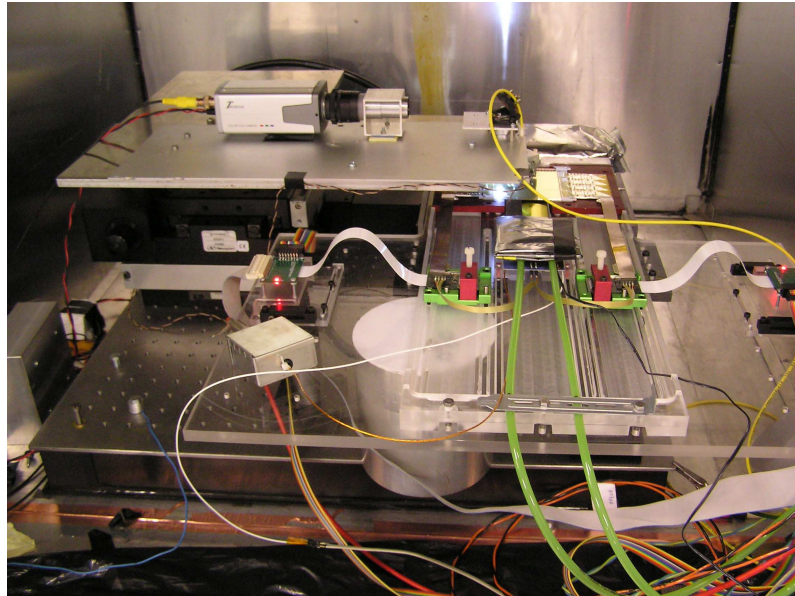


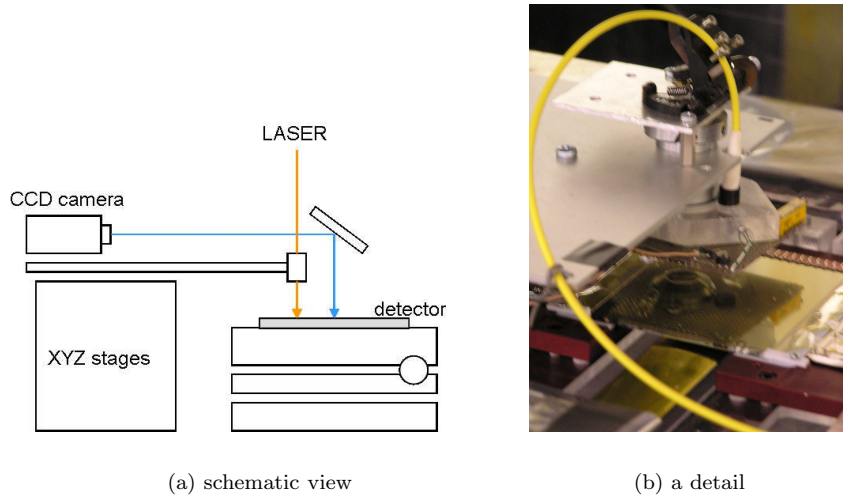
Figure 4.1: *Experimental set-up for laser mapping and diffusion measurements.*

is moved along the detector surface following a trajectory remotely controlled by a computer, which is different in the case of preliminary tests, mapping or diffusion measurements. The data acquisition software used is DATE [3], in order to reproduce ALICE read-out and acquisition system (DAQ).

4.2 Set-up

Figure 4.2(a) shows a schematic representation of the set-up. During all measurements, the SDD module is fixed upon a special support, which allows micrometric rotations of the detector surface, in order to align manually the detector plane with the reference system of the laser trajectories. The laser light, carried by an optical fibre, is moved over the wafer surface by means of micrometric XYZ stage with an accuracy of $2\text{-}3 \mu\text{m}$ ¹. The movement of the XYZ stage is driven by a motor controller interfaced to a remote computer. On the same structure a CCD camera is positioned, which follows (through a set of lenses) the laser spot trajectory with a fixed offset in x , y and z directions. Besides, since measurements are performed with the module biased at nominal voltages, the HV card is cooled by a system of circulating water. The entire set-up is positioned inside a Faraday cage in order to avoid electronic noise from the en-

¹A precision of $2\text{-}3 \mu\text{m}$ is achieved for absolute movements, while in the case of relative shifting even a better accuracy is attained. This mechanical system has been developed at the INFN in Turin.

Figure 4.2: *Laser-camera system.*

vironment. Furthermore the enclosure prevents the detector to undergo sudden break-downs due to direct light when it is biased.

4.2.1 Trigger and data acquisition

A schematic representation of the set-up, including trigger and DAQ, is shown in figure 4.3. The front-end electronics of the SDD module sends data to CARLOS board, which generates the signals to control the readout electronics and compress the data before sending them to CARLOSRx board. A CARLOSRx board can receive data from up to 12 CARLOS boards (i.e. 12 modules) and send them to the DAQ system via a DDL card². A data generator (DG2020) generates the clock for the front-end chips and synchronizes the trigger for CARLOS boards to this clock, resulting in a very good time resolution of the system (1 ns). The trigger logic is represented in figure 4.4. When motors reach the required position, the motor controller (MM4006 in figure 4.4) generates a trigger signal, which is synchronized to the clock by the DG2020. This signal triggers both the acquisition boards and the laser driver or alternatively the injectors or the test-pulse, depending on the measurement to be performed. Specifically, the test-pulse is used only in the first phase of detector testing. The trigger type (laser, injectors or test pulse) can be selected by means of control bits (Bit 0, Bit 1 and Bit 2 in figure 4.4), which are set by means of a LabView interface through the parallel port of the acquisition PC. Another way to set these bits is to implement specific commands in the file defining the trajectory of the mo-

²Detector Data Link interface card, consisting of a Source Interface Unit (SIU), a Destination Interface Unit and a duplex optical cable between them.

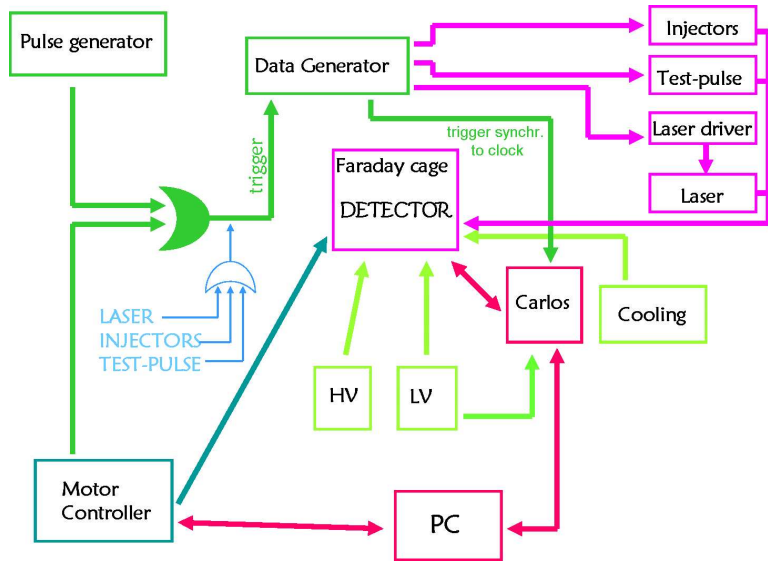


Figure 4.3: Schematic representation of the set-up.

tors.

A second possibility is to trigger the system directly with a pulse generator (indicated as *standalone* in figure 4.4) with a signal of variable frequency. During the tests we used a period of ~ 10 ms, corresponding to an event rate of about 90 ev/s. During the mapping the event rate was 80-85 ev/s, resulting in an amount of data of ~ 12 Mbyte/s. Three computers are used: a first one is strictly dedicated to data acquisition with DATE, a second one allows the monitoring with a full-custom LabView program and a third one performs data analysis and storage.

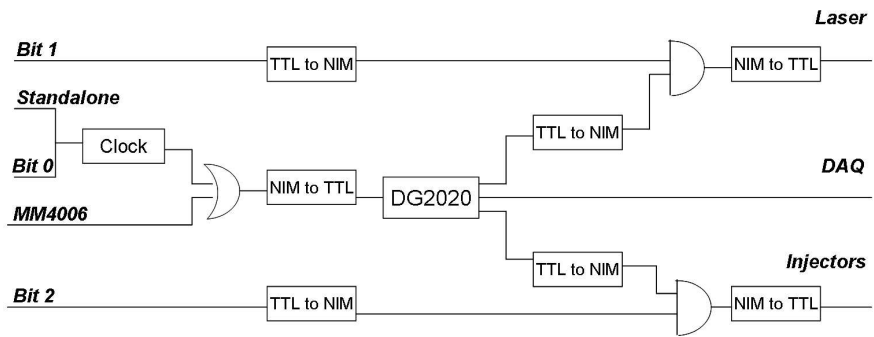


Figure 4.4: Trigger system.

4.3 Trajectory definition

In order to define a particular trajectory for the laser, the motor controller needs to be programmed. A LabView interface allows the execution of the trajectory and the storage of the data concerning the effective positions performed by the motors. Trajectories are written on specific ASCII files containing the sequence of commands to be executed. These files have to be written line by line or with the help of a C program in the case of very long trajectories. They also contain the trigger bit settings (laser or injectors) for the parallel port. In the full testing of a module, a set of test measurements has to be performed in order to measure baselines, noise, gain and to tag dead anodes, requiring a particular short scan run. Furthermore, for electron diffusion measurements and mapping two different trajectories are required.

4.3.1 Test scan

The trajectory followed by the laser is composed by 4 segments as shown in figure 4.5. When moving perpendicularly to the drift direction (segments A and C), the laser shoots exactly in front of each anode, i.e. every $294\ \mu\text{m}$, in order to determine if each channel is working. A channel is considered dead if the laser signal is not seen on it. When moving along the segment B of the trajectory, the laser is switched off and 573 injector triggers are collected. These events are used to tag the working injectors. When moving along D, both laser and injectors are switched off and 573 *empty* events are collected. These events are used to measure baselines, raw noise and common mode noise coefficients. The total number of collected events is thus given by:

$$256(A) + 573(B) + 256(C) + 573(D) = 1658 \quad (4.1)$$

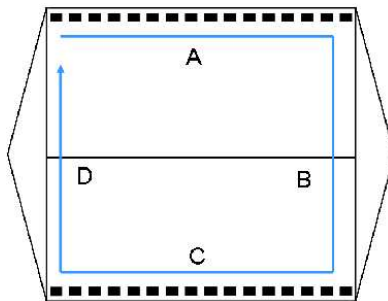


Figure 4.5: *Laser trajectory for preliminary measurements.*

4.3.2 Diffusion measurements

The corresponding trajectory is shown in figure 4.6. Along the anode direction the trajectory covers 601 points with a step of $5 \mu\text{m}$, scanning 3 mm (approximately 10 anodes) along anodes for every position in the drift direction. In the other direction the laser goes along 288 different positions with a step of $120 \mu\text{m}$, shooting exactly in the space between two adjacent cathodes. It is mandatory to shoot in this space (of about $40 \mu\text{m}$) because if the laser spot hits the cathode metallization (about $80 \mu\text{m}$ wide), photons are reflected backwards and the detector does not register any signal. For every point of the trajectory a laser event is acquired by the DAQ.

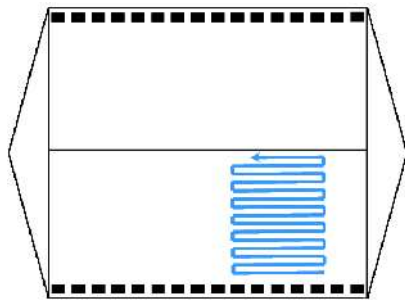


Figure 4.6: *Laser trajectory for diffusion measurements.*

4.3.3 Mapping required resolution

According to ALICE requirements, SDDs resolution in the $r\phi$ and z directions should be:

$$\begin{cases} \Delta(r\phi) = 38 \mu\text{m} \\ \Delta z = 28 \mu\text{m} \end{cases} \quad (4.2)$$

where the z coordinate in the ALICE reference system is measured by the anodes, while the $r\phi$ coordinate is the drift direction. Therefore the required resolution in the detector system is approximately:

$$\Delta x = \Delta y \simeq 30 \mu\text{m} \quad (4.3)$$

where x is the anodic coordinate and y the drift direction.

In our study the interesting variable is the difference δx between the real position of the laser shoot and the one reconstructed by the detector. So, the scan granularity should guarantee a resolution of $30 \mu\text{m}$ on the sampling length. In the most general case $\delta x = f(x, y)$ and the uncertainty on a measurement can be expressed as:

$$(\Delta \delta x)^2 = \left(\frac{\partial \delta x}{\partial x} \right)^2 (\Delta x)^2 + \left(\frac{\partial \delta x}{\partial y} \right)^2 (\Delta y)^2 + 2 \frac{\partial \delta x}{\partial x} \frac{\partial \delta x}{\partial y} \text{Cov}(x, y) \quad (4.4)$$

and similarly for the y coordinate. Assuming $Cov(x, y) = 0$, and $\Delta x = \Delta y$ we obtain:

$$\begin{cases} \Delta\delta x = \sqrt{\left(\frac{\partial\delta x}{\partial x}\right)^2 + \left(\frac{\partial\delta x}{\partial y}\right)^2} \Delta x \\ \Delta\delta y = \sqrt{\left(\frac{\partial\delta y}{\partial x}\right)^2 + \left(\frac{\partial\delta y}{\partial y}\right)^2} \Delta x \end{cases} \quad (4.5)$$

In August 2003, a mapping of the central part of one detector was performed during a Beam Test, giving the following result:

$$\sqrt{\left(\frac{\partial\delta x}{\partial x}\right)^2 + \left(\frac{\partial\delta x}{\partial y}\right)^2} = \sqrt{\left(\frac{\partial\delta y}{\partial x}\right)^2 + \left(\frac{\partial\delta y}{\partial y}\right)^2} = 200 \mu m/mm \quad (4.6)$$

Thus, in order to obtain the required precision $\Delta\delta x = 30 \mu m$, the sampling length should be at least $\Delta x = 150 \mu m$ corresponding to nearly a half anode spacing. Along drift direction y a sampling length of $120 \mu m$ has been chosen, corresponding to the cathode spacing, to avoid laser reflections on the cathode metallizations. If the wafer has no doping inhomogeneities, we do not expect deviations δx along the anodic coordinate and the sampling length along this direction can be more than a half anode spacing. In this case along the drift direction the deviations δy are due to the non-linearity of the voltage divider exclusively.

4.3.4 Mapping trajectory

The trajectory is showed in figure 4.7. In this case the laser scans 257 lines in between two adjacent anodes. Each line is composed of 581 points along the drift direction, with a step of $120 \mu m$; the motor speed is 10 mm/s . The total number of laser events is $257 \times 581 = 149317$, giving a raw data size of about 22 GB. This particular choice of trajectory, with lines parallel to the drift direction, is the most suitable for an efficient mapping. During a complete laser-scan, lasting about 40 minutes, detector temperature may vary significantly due to power dissipation of the front-end electronics and of the integrated voltage divider, causing variations in the electron drift speed and thus in the reconstructed position along drift direction. Nevertheless, if the events concerning the same position along anodes are taken in a short interval of time (about 10 s), we can make the approximation of a constant drift speed in each line, and use the same velocity for every point of the line to reconstruct the position along drift direction. The sampling lengths are $\Delta x = 294 \mu m$ along anodes and $\Delta y = 120 \mu m$ along drift direction, corresponding to:

$$\begin{cases} \Delta\delta x \simeq 39 \mu m \\ \Delta\delta y \simeq 24 \mu m \end{cases} \quad (4.7)$$

if equation 4.6 is assumed.

At the end of each line of mapping an injector event is registered. Injector events will be used to extract the electron drift speed, which will be compared

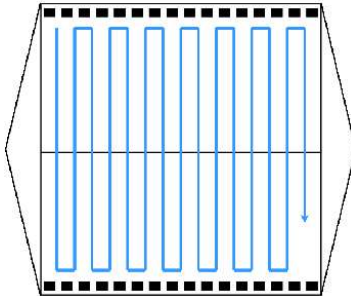


Figure 4.7: *Laser trajectory for mapping.*

to the one estimated from laser events.

Since the detectors under study do not show doping inhomogeneities, after some month of testing a shorter mapping trajectory has been introduced with a step of $294 \times 2 \mu\text{m}$ along anodes, which limits the time of a map to 20 minutes and the raw data file size to 11 GB.

4.4 Set-up optimization

In this section a set of preliminary measurements and considerations used for the tuning and the optimization of the test system are discussed.

4.4.1 Laser wavelength

Particular care should be taken in the selection of laser wavelength: it must be chosen in order to allow the release of charge along the whole thickness of the detector, so as to simulate a real crossing particle. A photon is able to release an electron from the silicon crystal if its energy is at least:

$$E_{GAP} = \frac{hc}{\lambda} = 1.1\text{eV} \quad (4.8)$$

corresponding to a wavelength of about $1.13 \mu\text{m}$. As shown in figure 4.8, if the wavelength is too large, i. e. the photon energy is too low, photons have a high probability to reach the opposite side of the wafer and to be reflected by the transition cable. The effect is clearly visible in the plot of charge collection as a function of the position on the SDD sensor represented in figure 4.9. For a wavelength of 1060 nm, the regions corresponding to the transition cable scatter the laser back, resulting in an increased collected charge (4.9(a)). Thus, a smaller wavelength of 980 nm has been chosen for all measurements and the charge released is uniform over all the detector volume (4.9(b)).

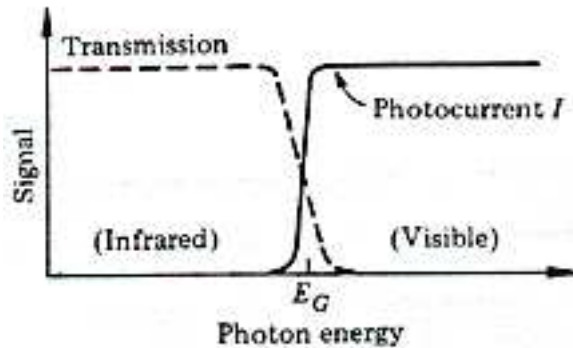


Figure 4.8: Probability of transmission as a function of photon energy.

4.4.2 Laser centering and focusing

In order to precisely position the detector on its mechanical support when mounting the modules, in the production of the sensor cross-shaped cuts are applied in the metallization of some particular cathodes. These crosses may be used as reference points during the geometrical measurements. During the complete testing, the detector is aligned with respect to the motor axis system. The alignment is performed with the aid of the CCD camera using the crosses A, B, C and D showed in figure 4.11. A scan over a restricted area ($\sim 200 \times 150 \mu\text{m}^2$) around a cross allows the reconstruction of the relative position of the laser spot with respect to the camera lens. The detector image from the CCD camera is properly enlarged by the lens and then projected on a TV screen, where a fixed reference point is marked. Thus, the zero coordinate for the scan is assumed to be the center of the cross when overlapping to the mark on the TV screen. It represents the center of the camera's reference frame. Figure 4.10(b) shows the result of a laser scan of the region around the cross. The reconstructed position of the center of the cross from the laser scan is exactly the distance between the spot pointed by the lens and the laser spot. The measured values for this offset in the anode and drift direction are respectively (0.933 ± 0.002) mm and (19.065 ± 0.002) mm.

Furthermore the scan should be performed at different values of z coordinate (normal to the detector surface) in order to determine focus and inclination of the laser beam. The laser scan showing the best cross resolution corresponds to the minimum beam spot extention (laser focus) and it is located at a distance of 1.3 mm along z from lens focus. Since the step of the z scan is $100 \mu\text{m}$, the precision on the laser focus position is $\pm 100 \mu\text{m}$. It has been verified that there is no difference in the mapping results if the laser focus is positioned at $\pm 100 \mu\text{m}$ from the estimated optimal coordinate. Besides, since the measured cross position is the same for each z coordinate, the laser direction is assumed to be perpendicular to the detector surface.

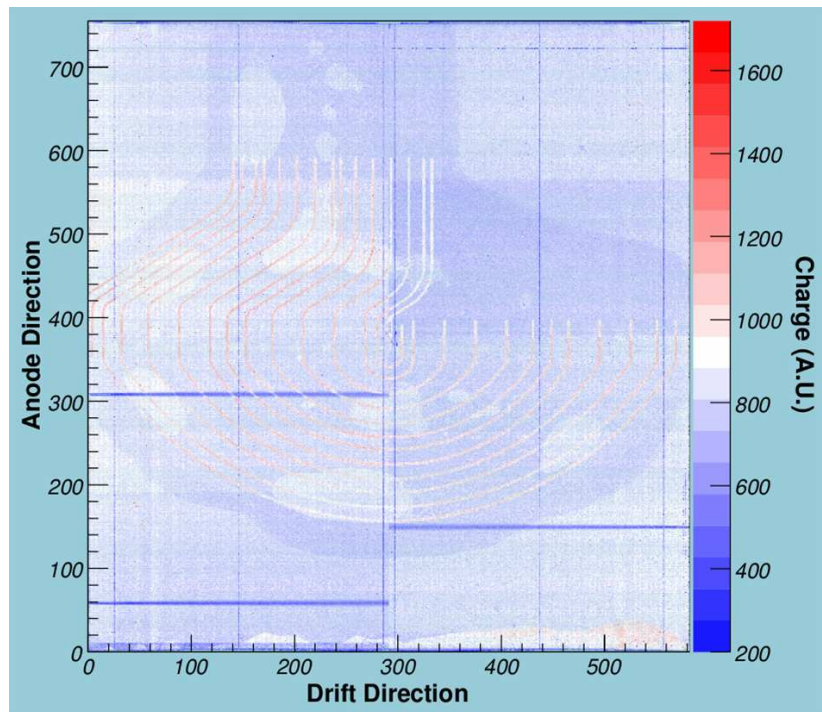
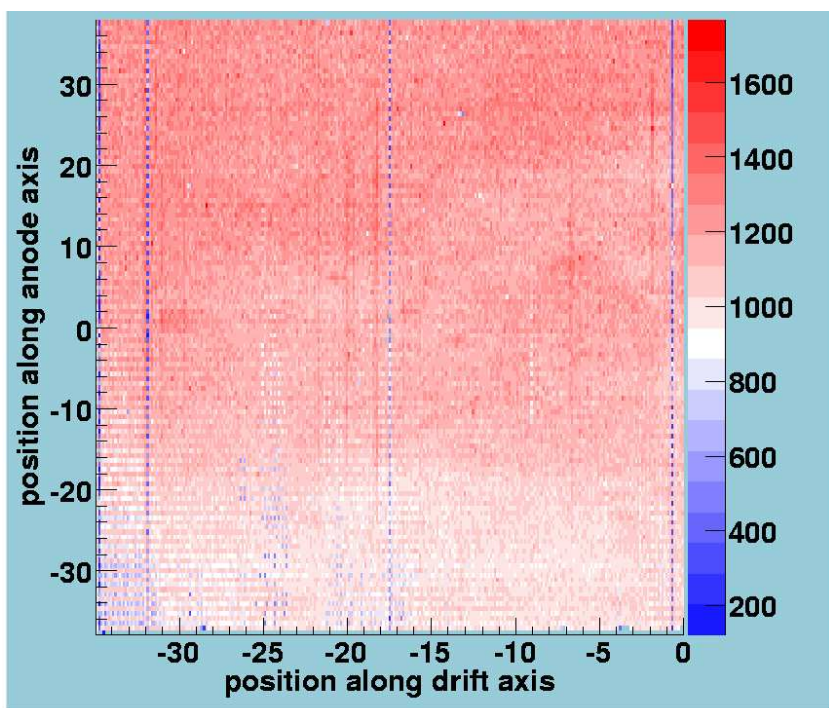
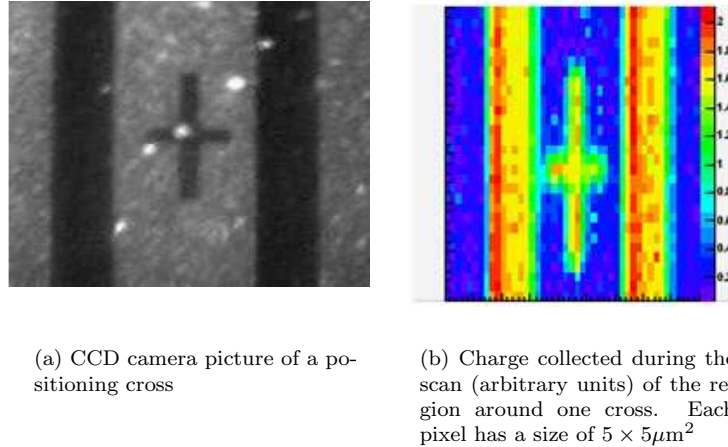
(a) $\lambda = 1060$ nm(b) $\lambda = 980$ nm

Figure 4.9: Map of the charge collected by the detector for different laser wavelengths.

Figure 4.10: *Determination of the laser-camera offset.*

4.4.3 Motor axis angle

The x and y motor axes, parallel to the detector plane, are not exactly perpendicular. In the case of laser-mapping, detector drift direction y is aligned with the motor y axis and there is a θ angle between motor and detector x axes. Thus, during all measurements, trajectory positions should be set taking into account this angle. In each mapping line, motors should move precisely perpendicular to the anodes row, so that the laser shoot in front of the same anode during the entire path along the drift direction. Thus, before a laser mapping, cross A and B must be manually aligned to the motor y axis. On the contrary, for electron diffusion measurements, motor axis should be aligned parallel to the anodes row; otherwise during each line of the trajectory the misaligned laser could hit a cathode metallization, losing all the signal or part of it. In the case of laser mapping y_D is parallel to y_M (see figure 4.12) and the relationship between the two reference frames is:

$$\begin{cases} x_D = x_M \cos \theta \\ y_D = y_M + x_M \sin \theta \end{cases} \quad (4.9)$$

Where x_D and y_D are the orthogonal axes on the sensor and x_M and y_M are the motor axes (x_M is not perpendicular to y_M). Equivalently:

$$\begin{cases} x_M = \frac{x_D}{\cos \theta} \\ y_M = y_D - x_D \tan \theta \end{cases} \quad (4.10)$$

where (x_M, y_M) are the corrected coordinates defining the mapping trajectory and (x_D, y_D) are the real positions on the detector surface. The measured value for the θ angle is obtained by measuring the distance CC' represented in figure

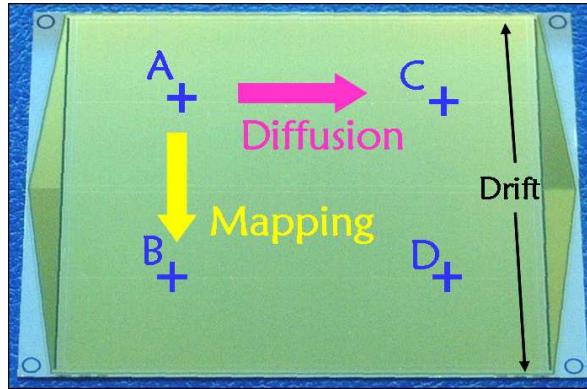


Figure 4.11: Reference crosses for detector alignment on the top side of the SDD sensor.

4.13. It is easily measured with the CCD camera as a shift between the position of the cross C and the position C' on the detector when the motors are moved in the nominal coordinates of cross C. The value of CC' is $(60 \pm 2) \mu\text{m}$ and the nominal AC distance is 39 mm, so:

$$\theta = \tan^{-1} \left(\frac{60 \mu\text{m}}{39 \text{mm}} \right) = 0.0015 \pm 0.0001 \text{ rad} \quad (4.11)$$

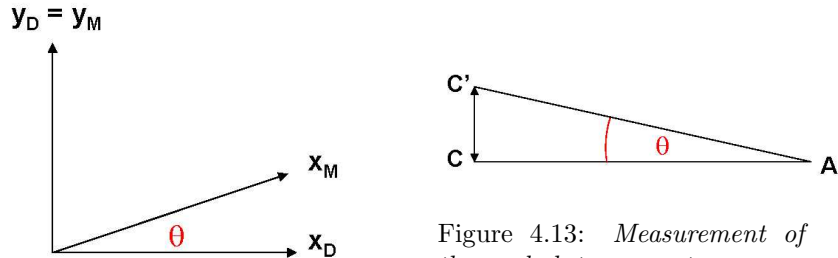


Figure 4.12: The angle θ between detector and motors axes.

Figure 4.13: Measurement of the angle between motors.

Bibliography

- [1] G. Batigne, *9th ICATPP Conference Proceedings*, Villa Olmo (Como), October 2005
- [2] E. Crescio et al., Nucl. Instr. and Meth. **A 539** (2005) 250
- [3] <http://ph-dep-aid.web.cern.ch/ph-dep-aid>

Chapter 5

Electron diffusion

5.1 Introduction

In Silicon Drift Detectors used in the ALICE experiment the electron drift time is of the order of few μs and the charge cloud ¹, released by the crossing particle, spreads in the detector volume while drifting because of diffusion and Coulomb repulsion. In the z direction, perpendicular to the detector surface, these phenomena are compensated by the parabolic potential, while they cause an increase of the electron cloud size in both the other directions. The effect of diffusion plays a crucial role in the determination of the anodic coordinate. If the particle crosses the detector near the anodes the charge released is typically collected by only one anode (narrow Gaussian-like signal). In this case the resolution on the anodic coordinate is $1/\sqrt{12}$ times the anode pitch. For longer drift distances the charge can be collected by up to three anodes, because of diffusion, producing a wide Gaussian-like signal. Therefore, the impact point along the anodic coordinate can be reconstructed from the centroid of the charge collected by the hit channels. In this case the measurement precision is considerably improved with respect to the case of a single hit channel. Besides, an excessive broadening of the pulses can affect the resolution along the drift coordinate and double particle resolution, as well as working parameters of front end electronics. For a fixed amount of charge released, a wide signal has a lower amplitude than a narrow one. If the signal pulse is lower than the electronic noise, detector efficiency is seriously compromised. Figure 5.1 represents the evolution of the charge cloud size during drift, showing that, depending on the drift distance, it can be collected by a different number of anodes and be extended over different numbers of time bins.

Next section analyzes the problem of electron diffusion making some important approximations:

- assume a fixed value for electron mobility

¹The charge cloud is generally defined a *cluster*.

- neglect Coulomb repulsion
- ignore holes, which are instantaneously collected by the p^+ electrodes
- assume constant electric field along drift (y) direction, which is not completely true because of the discreteness of the field electrodes on the detector surface, the non-linearities of the voltage divider and the possible dopant inhomogeneities.

Section 5.3 shows the most representative experimental results obtained with the laser scan system. In section 5.4 the results are compared to similar measurements performed on the SDDs of the STAR experiment at RHIC. Finally, in section 5.5 some conclusive considerations are exposed, justifying the obtained results.

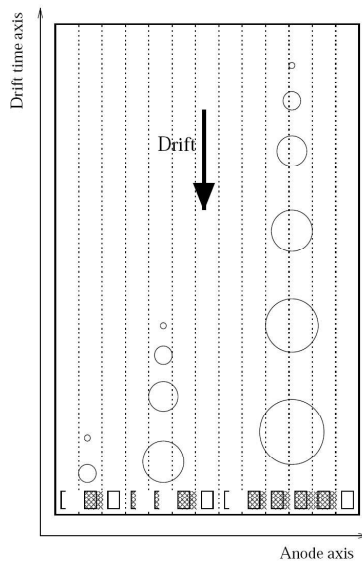


Figure 5.1: *Evolution of the electron cloud during the drift.*

5.2 Electron dynamics

In a silicon drift detector electron dynamics is determined by three main factors: external electric field, diffusion and Coulomb repulsion. In a first approximation Coulomb repulsion can be neglected, in order to get a simple understanding of the diffusion contribution to the cloud expansion. The external electric field \vec{E}

may be expressed through its components:

$$\begin{aligned} E_x &= 0 \\ E_y &= \text{constant} \\ E_z &= \frac{qN_D}{\epsilon}z \end{aligned} \quad (5.1)$$

where q is the elementary charge and E_z is the field component perpendicular to the detector surface, related to the fixed electrostatic charge of the depleted region. Thus, electron motion is separated into three contributions along the different axes. Considering diffusion and drift currents along z direction only, a *continuity equation* can be written:

$$\frac{\partial^2 n}{\partial z^2} - \frac{1}{D} \frac{\partial n}{\partial t} + \frac{K}{V_T} \left(n + z \frac{\partial n}{\partial z} \right) = 0 \quad (5.2)$$

where D is the diffusion constant, V_T the thermal voltage ² and $n(z, t)$ the electron density per unit length in the direction perpendicular to the surface. A formal solution of eq. 5.2 is represented by a series expansion in terms of Hermite polynomials. If the diffusion is compensated by the focusing electric field (steady situation), an asymptotic solution can be written:

$$n(z, \infty) = A_0 \exp \left\{ \frac{-Kz^2}{2V_T} \right\} \quad (5.3)$$

Along the drift direction y , electron dynamics is given by the superposition of free diffusion and drift; while in x direction motion is due to free diffusion only, without confining forces. In the (x, y) plane electron distribution is given by the product of two Gaussian shapes:

$$n(x, t)n(y, t) = \frac{1}{2\pi} \frac{1}{2Dt} \exp \left\{ -\frac{x^2}{4Dt} \right\} \exp \left\{ -\frac{(y - \mu E_y t)^2}{4Dt} \right\} \quad (5.4)$$

being μ the electron mobility in silicon. The cloud width is given by $\sigma = \sqrt{2Dt}$. The charge released by a crossing particle is confined in the middle plane of the detector within a few tens of nanoseconds. Charge density is expressed as:

$$\rho(\vec{r}, t) = \frac{Q}{2\pi\sigma^2(t)} \exp \left\{ -\frac{[\vec{r} - \vec{r}_0(t)]^2}{2\sigma^2(t)} \right\} \quad (5.5)$$

where Q is the total charge and $\sigma(t)$ is the charge cloud size at time t . Under the common assumption of small charge released ³ a possible parametrization for

²The *thermal voltage* is given by:

$$\frac{K_B T}{q}$$

with K_B the Boltzmann constant and T the absolute temperature.

³A MIP produces ~ 25000 electrons in a $300 \mu\text{m}$ thick silicon wafer

the time dependence of the cloud size, taking into account Coulomb repulsion, could be:

$$\sigma(t) = \sqrt{2Dt + \sigma_0^2} \quad (5.6)$$

being D the *diffusion coefficient*:

$$D = \frac{K_B T}{q} \mu \quad (5.7)$$

with K_B the Boltzmann constant and T the absolute temperature.

Coulomb repulsion, which is expected to be significative only for small drift times, is taken into account by the parameter σ_0 , representing the effective initial size of the cloud.

5.3 Experimental results

Diffusion measurements are performed on a restricted selection of detectors, with the purpose of estimating the diffusion coefficient and the detector temperature, as well as the electron drift speed. Each line of the laser trajectory scans 3 mm along anode direction covering about 10 anodes, as explained in section 4.3.2. Figure 5.2 shows the charge collected by a single anode, in units of ADC counts versus the laser position along the anode direction for one line of the trajectory. The zero coordinate corresponds to the edge of the detector. The complete scan gives 288 plots similar to the one of figure 5.2. The black solid line is the fit to data. If x is the distance from the cloud center to the edge of the considered anode, Q_{TOT} the total charge of the cloud and $n(x,t)$ the normalized electron density, then the charge collected by the anode is given by:

$$Q(x) = Q_{TOT} \int_x^{x+\Delta} n(x', t) dx' \quad (5.8)$$

where Δ is the effective anode lenght along x axis, i.e. 294 μm .

In practice, for every laser position (x) this quantity is evaluated by summing the contents of all the time-bins exceeding a fixed threshold. The measurement is performed after baseline subtraction.

5.3.1 Fit to data

The shape of plot 5.2 is expected to be the convolution of a *step function*, representing the anode response, and a *Gaussian function*, describing the electron distribution within the cloud. Let x be the coordinate along anodes, $A(x)$ the anode shape and $B(x)$ the laser beam shape. The anode shape $A(x)$ is a rectangle function whose value is 1 if $-\Delta/2 < x < \Delta/2$ and 0 elsewhere, with $\Delta = 294$

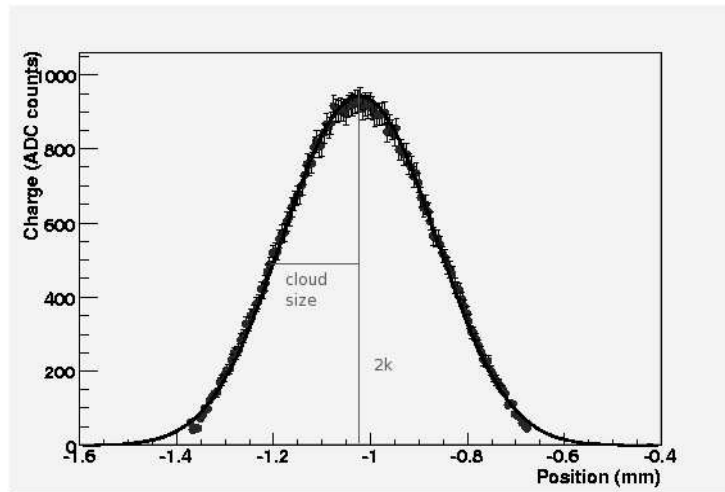


Figure 5.2: Charge collected (ADC counts) by the anode under study vs. laser position along anode coordinate for a single scanning line.

μm . Thus the charge collected by the anode is:

$$\begin{aligned}
 Q(x) &= \int_{-\infty}^{\infty} A(z)B(z-x)dz = \\
 &= \int_{-\Delta/2}^{\Delta/2} B(z-x)dz = \\
 &= \int_{-\Delta/2}^0 B(z-x)dz + \int_0^{\Delta/2} B(z-x)dz = \\
 &= \int_0^{\Delta/2} [B(-z-x) + B(z-x)] dz
 \end{aligned} \tag{5.9}$$

where x is the center of the beam spot along anode coordinate and z is directed along anodes. Assuming a Gaussian beam shape:

$$B(z) = \frac{k}{\sqrt{2\pi}\sigma} \exp\left(-\frac{z^2}{2\sigma^2}\right) \tag{5.10}$$

then:

$$Q(x) = \frac{k}{\sqrt{2\pi}\sigma} \int_0^{\Delta/2} \left\{ \exp\left[-\frac{(z+x)^2}{2\sigma^2}\right] + \exp\left[-\frac{(z-x)^2}{2\sigma^2}\right] \right\} dz \tag{5.11}$$

We introduce the Error function, which is defined as:

$$Erf(x) = \frac{2}{\sqrt{\pi}} \int_0^x e^{-t^2} dt \tag{5.12}$$

so:

$$\begin{aligned} Q(x) &= 2k \left\{ \left[\operatorname{Erf} \left(\frac{\Delta/2 + x}{\sqrt{2}\sigma} \right) - \operatorname{Erf} \left(\frac{x}{\sqrt{2}\sigma} \right) \right] + \right. \\ &\quad \left. + \left[\operatorname{Erf} \left(\frac{\Delta/2 - x}{\sqrt{2}\sigma} \right) - \operatorname{Erf} \left(\frac{-x}{\sqrt{2}\sigma} \right) \right] \right\} \end{aligned} \quad (5.13)$$

Since $\operatorname{Erf}(x) = -\operatorname{Erf}(-x)$, the convolution shape is:

$$\begin{aligned} Q(x) &= 2k \left[\operatorname{Erf} \left(\frac{\Delta/2 + x}{\sqrt{2}\sigma} \right) + \operatorname{Erf} \left(\frac{\Delta/2 - x}{\sqrt{2}\sigma} \right) \right] = \\ &= 2k \left[\operatorname{Erf} \left(\frac{x + \Delta/2}{\sqrt{2}\sigma} \right) - \operatorname{Erf} \left(\frac{x - \Delta/2}{\sqrt{2}\sigma} \right) \right] \end{aligned} \quad (5.14)$$

where k is half the distribution amplitude, Δ the anode pitch and σ the expected electron cloud size.

Fit parameters

We introduce a parameter x_0 in order to center the fit around the center of the experimental plot. Therefore $x = X - x_0$ where X is the reference frame centered in the middle of the anode under study. So, the effective fit function is:

$$Q(x) = 2k \left[\operatorname{Erf} \left(\frac{X - x_0 + \Delta/2}{\sqrt{2}\sigma} \right) - \operatorname{Erf} \left(\frac{X - x_0 - \Delta/2}{\sqrt{2}\sigma} \right) \right] \quad (5.15)$$

which in principle has four free parameters: x_0 , k , σ and Δ .

The anode pitch Δ may be either fixed at its nominal value of 294 μm or treated as a free parameter, since fabrication processes could introduce small variations in its value. Several fits have been performed for different positions along the drift direction. Generally fits with the anode pitch as free parameter show better χ^2 values than the ones with a fixed pitch value of 294 μm . Nevertheless, far from the anodes the obtained values for σ and Δ are completely unreasonable. The reason is that these two parameters are anti-correlated and the best fit value could result for a completely unphysical value of the anode pitch. It was also tried to force the parameter Δ to vary in a narrow range around 294 μm , but the minimization procedure was always converging towards larger values of Δ (and lower for σ). For this reason, the Δ pitch has been fixed to the nominal value of 294 μm and only 3 free parameters (k , x_0 and σ) were used. In this way the fits show increasing values of σ while the laser moves away from the anodes along the drift direction. This result corresponds to the expected behaviour for the anode response, since for longer drift times the electron cloud is widespread and part of its charge is collected by the channels adjacent to the one under study. Thus the beam shape shows decreasing height $2k$ and increasing cloud size σ while moving away from the anodes. This effect is evident in figure 5.5, where the charge collected for several lines of scanning is shown for one of the particular anodes.

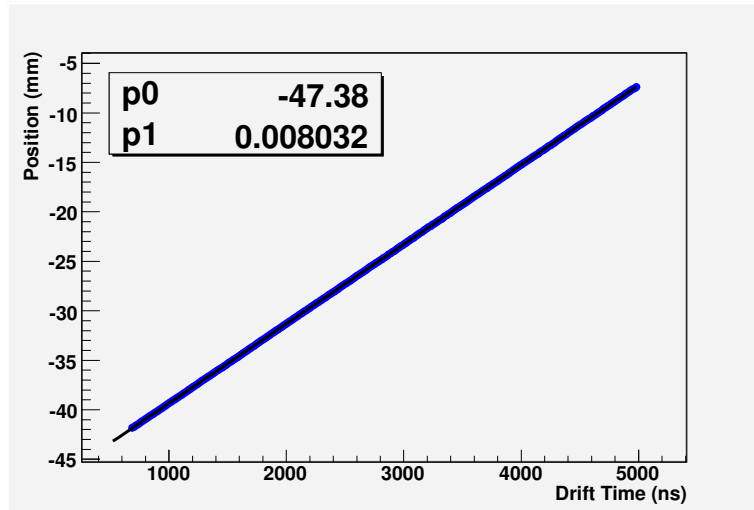


Figure 5.3: *Position along drift direction (mm) vs. drift time (time bins).*

5.3.2 Drift speed

Figure 5.3 shows a typical plot of the laser position as a function of the measured drift time for 288 lines of scanning. The values of the y positions are the coordinates of the trajectory points, while the drift times correspond to the mean over all the measured time-bin centroids of a single line of the trajectory. The dependence is linear and the slope of the fit gives the electron speed, which is then converted in physical units taking into account that each time-bin corresponds to 25 ns. Data were taken from May to July 2006 on different detectors in different temperature conditions. Since a direct measurement of the detector temperature is not possible, drift velocity measurements can give an indirect estimation of this parameter. Measurements were performed at normal room temperature ($\sim 20^\circ\text{C}$) both with and without a fan inside the Faraday cage in May and at a very high room temperature ($\sim 28^\circ\text{C}$) in July. The effect of the fan is to carry away from the detector the heat produced by the voltage divider, the wrap-around cable and the front-end chips. Figure 6.8 shows the values obtained for the drift speed relative to each scanned anode. As expected, the higher the temperature, the lower the drift velocity. The errors are given by the fit parameter errors. Since the fit is performed on a large number of data the errors are very small, of the order of 0.02 % and they are not visible in the plot.

5.3.3 Detector temperature

Electron drift speed v is linked to the electron mobility μ and to the drift electric field E through the relation: $\mu = v/E$. At a detector temperature of 20°C (293

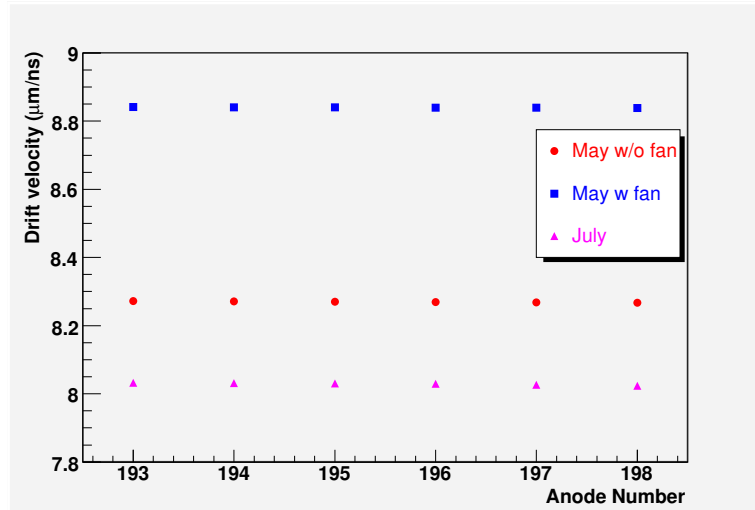


Figure 5.4: Drift speed vs. anode number for different experimental conditions.

K) the electron mobility for the resistivity of the SDD detectors is $1350 \text{ cm}^2 \text{ V}^{-1} \text{ s}^{-1}$. Besides $\mu(t) \propto T^{-2.4}$, thus:

$$\frac{\mu}{\mu_{20^\circ C}} = \left(\frac{T}{293} \right)^{-2.4} \quad (5.16)$$

The electric field is 666 V/cm. According to these considerations, detector temperature can be estimated. Table 5.1 summarizes the results obtained for drift speed, electron mobility and detector temperature under the three different experimental conditions. Errors on drift velocity are not quoted because they are negligible. The values of temperature are only estimations because of the assumptions on the electron mobility value at $20^\circ C$ and on its dependence on the temperature (5.16). However the estimated values are reasonable. In May the room temperature was about $20^\circ C$ and the measured value of $\sim 22^\circ C$ for the detector indicates that the fan was efficient in removing the heat and cooling the detector at about room temperature. In July the room temperature was about 5-6°C higher than in May, causing a similar increase in the detector temperature.

5.3.4 Diffusion coefficient

The diffusion coefficient D can be estimated from the width of the fitting function described in section 5.3.1 at different drift times, using the relation:

$$[\sigma(t)]^2 = 2Dt + \sigma_0 \quad (5.17)$$

Table 5.1: *Measured drift speed and estimated electron mobility and detector temperature under different experimental conditions.*

	Drift speed ($\mu\text{m}/\text{ns}$)	Electron mobility ($\text{cm}^2\text{s}^{-1}\text{V}^{-1}$)	Temperature (C)
May (no fan)	8.3	1246	30°
May (fan)	8.8	1321	22°
July (no fan)	8.0	1201	34°

where σ is the cloud size from the fit to data (paragraph 5.3.1) and σ_0 is a fixed offset used to account for the Coulomb repulsion effect. Figure 5.6 shows a plot of $\sigma(t)^2$ as a function of drift time for a single anode, the slope of the linear fit being two times the diffusion coefficient. A linear fit is not suitable, at least if the first points (at small drift times) are included. This indicates that the parametrization of Coulomb repulsion is not optimal to fully describe experimental results. Assuming Coulomb effect to be more influent at short drift times, a second fit is performed, neglecting the first points with a drift time < 2 ns, which show a non-linear behaviour. For the plot in figure 5.6(a) the χ^2/ndf value for the fit performed on all the data is about 66, while it is reduced to 35 if the first points are excluded (figure 5.6(b)). The diffusion coefficient has been estimated from the fit slope when short drift times data are excluded.

Table 5.2 shows the estimated values of the diffusion coefficient for a particular anode. Fit parameter errors are quoted. The systematic error introduced by neglecting the first data is about 11 %, which corresponds to the fluctuation of the value of D when the fit range is varied. The expected value for the diffusion coefficient, quoted in table 5.2, is calculated from equation 5.7. Measured values of D are systematically higher than the expected ones, probably because a wrong parametrization of the Coulomb effect has been chosen.

Table 5.2: *Temperature, electron mobility and diffusion coefficient under different experimental conditions.*

	Temperature (C)	Electron mobility ($\text{cm}^2\text{s}^{-1}\text{V}^{-1}$)	Expected D ($\mu\text{m}^2/\text{ns}$)	Measured D ($\mu\text{m}^2/\text{ns}$)
May (no fan)	30°	1246	3.34	5.450 ± 0.005
May (fan)	22°	1321	3.25	5.235 ± 0.005
July (no fan)	34°	1201	3.18	5.825 ± 0.005

5.4 Comparison with STAR SDDs results

Cloud size measurements were performed also by the STAR-SVT (the Silicon Vertex Tracker of the STAR experiment) collaboration. The STAR2.9 silicon drift detector was used, which was produced from a 300 μm thick NTD silicon

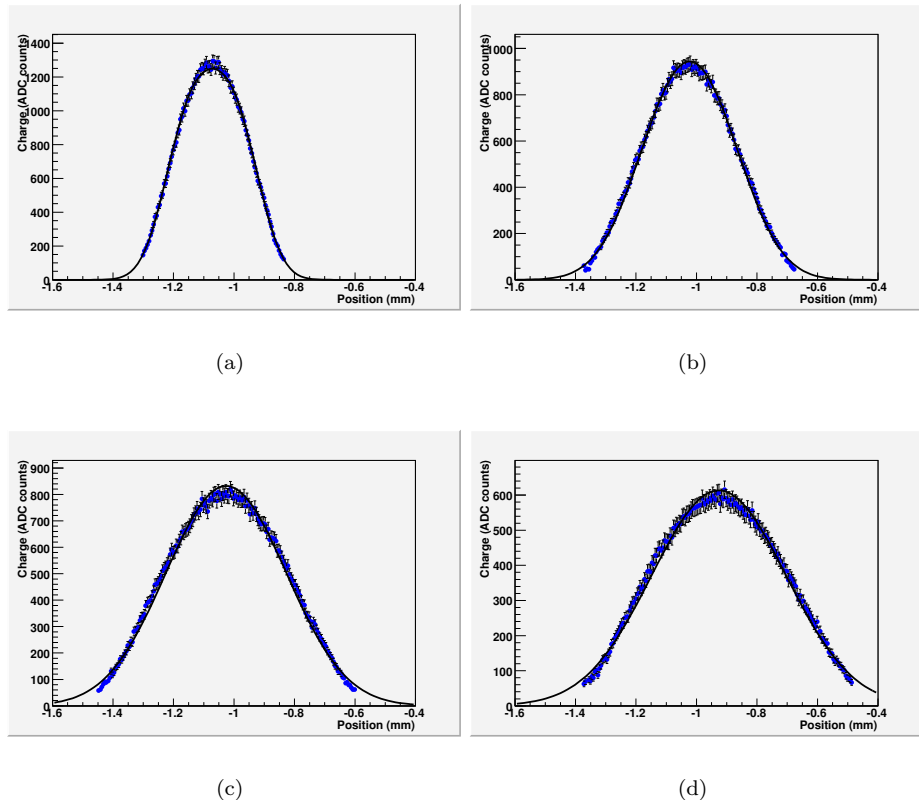
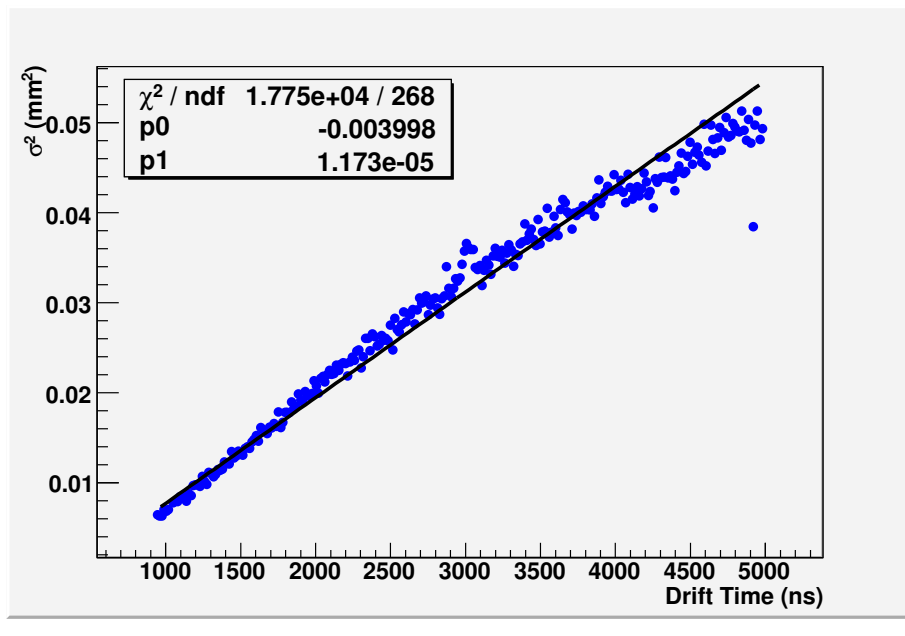


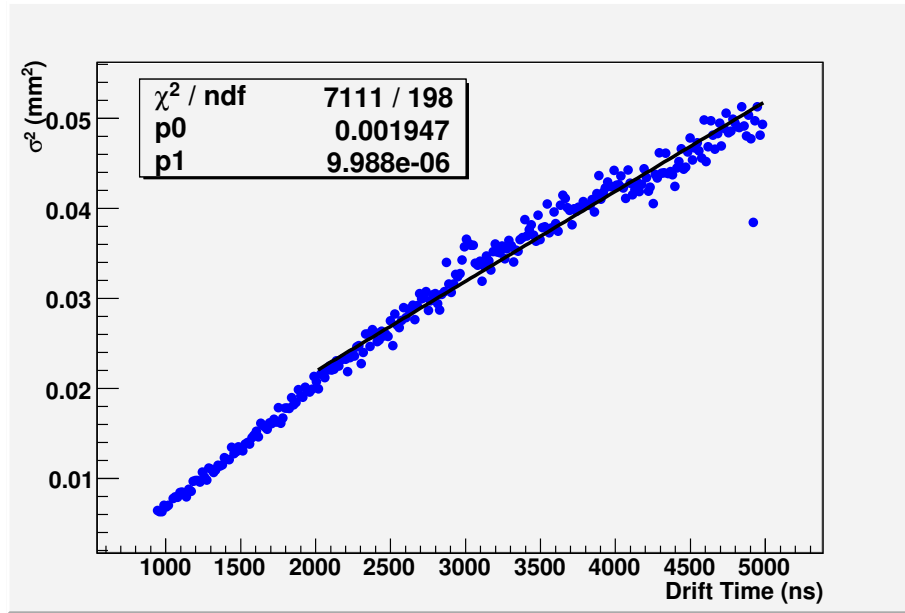
Figure 5.5: Charge collected (ADC counts) by a single anode vs. laser position along anode coordinate for different scanning lines. Far from the anodes the electron cloud diffusion effect shows up in the charge distribution broadening and lowering.

wafer with an approximate resistivity of $3 \text{ k}\Omega \text{ cm}$. Its electrical properties should be very similar to those of the ALICE-D2, while the detector design is rather different⁴. In particular, the maximum drift distance is 30 mm, the anode pitch is $250 \mu\text{m}$ and the cathode pitch is $135 \mu\text{m}$. Two methods were used to measure the cloud size. The method of cumulative functions was used to extract the electron cloud profiles. The second method is the same we used to obtain the cloud width from measurements of the charge collected on a single anode as a function of the anodic coordinate of the laser spot.

⁴A detailed description of the STAR-SVT SDDs can be found in ref. [3].



(a) linear fit to all data



(b) linear fit neglecting the first points

Figure 5.6: $\sigma(t)^2$ in mm 2 vs. drift time in ns. The black solid line represents the linear fit to data.

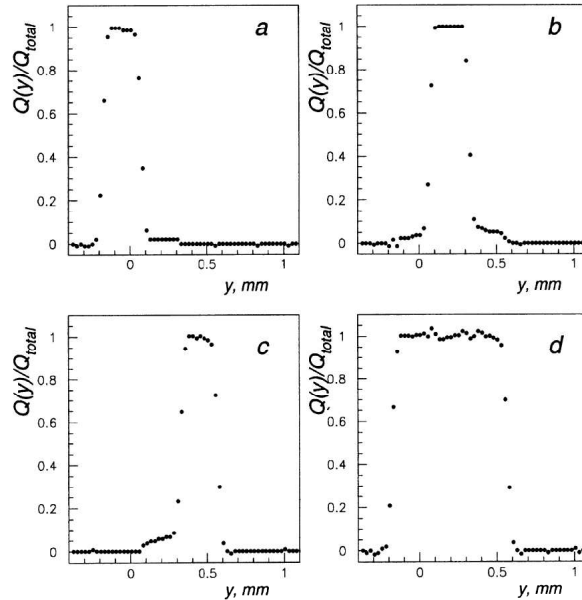


Figure 5.7: Fraction of the charge collected (cumulative function) vs. position of the light spot. (a)-(c) individual anodes, (d) sum over three anodes.

Set-up

An IR LED of wavelength 820 nm was used to generate electrons near the detector surface. The light pulse duration was less than 8 ns and the repetition rate was 0.2 Hz. Data were read out via a 500 MHz digital oscilloscope. The LED light was focused by a microscope into a spot of about 20 μm in diameter. One light pulse generated about 6.2×10^4 electrons, i.e. 2.5 times of a MIP crossing the detector plane. The detector was placed on a XY stage with a position resolution of 0.5 μm for both axes. Measurements were performed in eleven positions along the drift length. At each drift distance the light spot was moved along the anode axis with a step of 25 μm and 40-65 points were taken. The transport field was 400 V/cm. From the drift time versus drift distance plot a drift velocity of 5.2 $\mu\text{m}/\text{ns}$ was estimated.

Cumulative functions method

The *cloud profile* is defined as the charge density of the electron cloud projected onto the drift or anodic axis ($n(y,t)$ and $n(x,t)$ respectively). If the anode dimension is larger than the cloud size or a sum over enough anodes to cover the cloud is performed, equation 5.8 can be rewritten in terms of the cumulative

function $\Phi(x,t)$:

$$\Phi(x, t) = \frac{Q(x)}{Q_{TOT}} \int_x^\infty n(x', t) dx' \quad (5.18)$$

The cumulative function varies in the range [0, 1]. Its value is zero when the cloud distance from the readout anodes is larger than the cloud size and 1 when the cloud is completely covered by the readout anodes. The average electron cloud profile is given by the derivative of the cumulative function with respect to the anodic coordinate:

$$n(x, t) = \frac{\partial \Phi(x, t)}{\partial x} \quad (5.19)$$

The cumulative function can be measured directly by moving the light spot along x . Figure 5.7 shows the results obtained by three different anodes when the laser scans the closest positions from the anodes, since this method can be used only for those drift times where the cloud is fully covered by three anodes. The cumulative function is plotted versus the position of the light spot along anodic coordinate. Each anode provides two measurements of the cumulative function: the left edge gives $\Phi(x)$ and the right one gives $1-\Phi(x)$. Figure 5.8 shows the cloud profiles $n(x,t)$ and $-n(x,t)$ for the same laser positions, calculated by numerical differentiation of $\Phi(x)$ and $1-\Phi(x)$. As expected the profiles have Gaussian-like form. At that drift distance the measured cloud width is $\sigma \simeq 20 \mu\text{m}$, which is in agreement with the light spot size. Factors limiting the accuracy of measurements are the fluctuations of the laser intensity, the electronic noise, the accuracy in the positioning of the XY stage and the precision of the calibration.

Single anode method

The method is the same used for the ALICE SDD diffusion measurements. The fitting function has the same shape as equation 5.14 and the fit free parameters are the total charge released by the laser Q_{TOT} and the cloud size σ , assuming a Gaussian distribution of electrons inside the cloud. For each laser position along the drift time, the experimental values for the cloud size from both methods are in good agreement.

Results

Figure 5.9 shows a plot of the electron cloud size as a function of the drift time. Experimental data are in good agreement with the solution of a continuity equation which takes into account both diffusion and Coulomb repulsion contributions for a total released charge of 6.2×10^4 electrons (solid line). The values of diffusion coefficient and electron mobility used in the calculation to reproduce the experimental measurements are:

$$D = 3.5 \mu\text{m}^2/\text{ns}$$

$$\mu = 1350 \text{ cm}^2\text{s}^{-1}\text{V}^{-1}$$

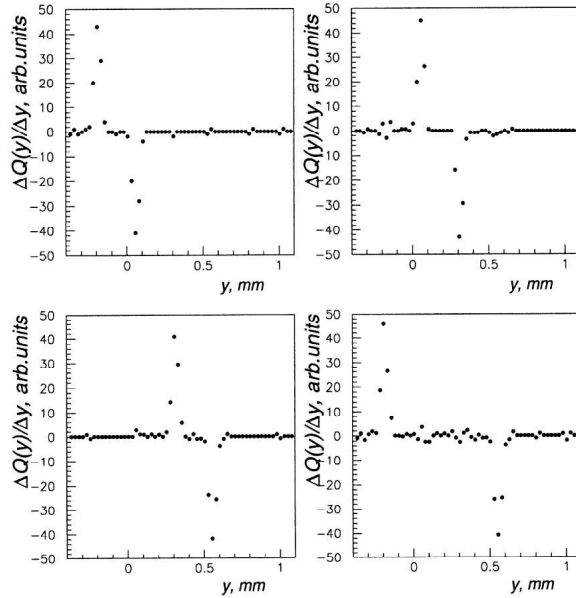


Figure 5.8: *Cloud profiles (y is the anode coordinate).*

Therefore even at this low ionization the contribution of Coulomb repulsion is significant, particularly at short times while the cloud size is small ($< 100 \mu\text{m}$).

5.5 Conclusions

During the complete tests of the ~ 300 SDD modules, electron diffusion has been studied on a subsample of detectors. We performed a laser scan along anode direction at different positions along the drift direction. Fits to experimental data allowed the measurement of: electron drift speed, diffusion coefficient and detector temperature. As expected, measurements performed at different detector temperatures show that the drift speed increases with decreasing temperature. The diffusion coefficient has been estimated neglecting Coulomb repulsion. This assumption is correct only in the case of small charge released in the detector volume or alternatively for large drift times. The exact amount of charge released by the laser could not be determined since this measurement requires an absolute calibration of PASCAL ADC which was not yet achieved during the test phase. To account for the Coulomb repulsion, data corresponding to short drift times (< 200 ns) have been excluded from the analysis. Therefore the results described in this section should be considered as a raw approximation of the diffusion coefficient. More precise results could be achieved in a future

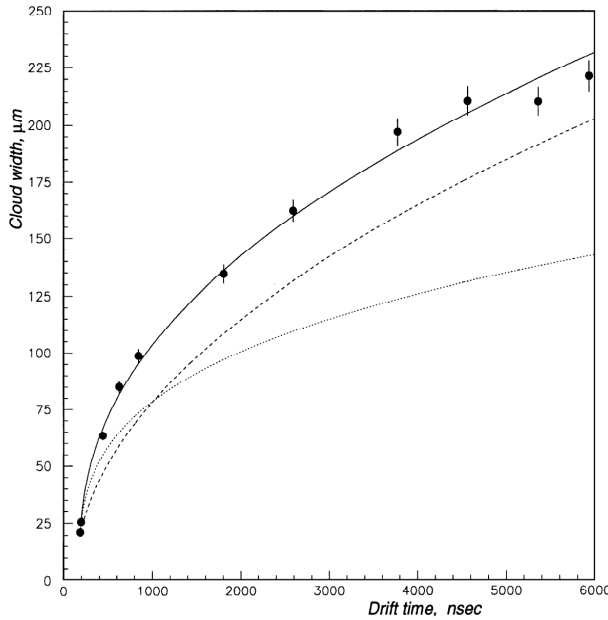


Figure 5.9: *Dependence of the cloud size on drift time. Points are data. Solid line shows a solution of the continuity equation with both diffusion and Coulomb repulsion contributions. Dashed line shows the diffusion only. Dotted line shows Coulomb repulsion only.*

analysis using an appropriate parametrization of the Coulomb effect and by repeating the measurements with lower laser intensity. Also the size of the laser spot has not been measured up to now.

Similar measurements have been performed on the SDD used in the STAR experiment at RHIC, using a rather different experimental set-up. In particular the number of steps and therefore of laser shots are different. At RHIC for each point of the trajectory the laser shot at a high repetition rate, while in our measurements the laser shot only once on each position, but a higher statistics could be achieved because of the longer scan trajectory. Besides, the beam spot dimension and the amount of charge released were well-known. Assuming a given value for the diffusion coefficient, the electron cloud size has been estimated using two different methods, pointing out at the same result compatible with the laser spot dimension.

Bibliography

- [1] E. Gatti, A. Longoni et al., *Dynamics of electrons in drift detectors*, Nucl. Instr. and Meth. **A 253** (1987) 393-399
- [2] STAR-SVT Collaboration, *Silicon Drift Detectors for the STAR-SVT experiment at RHIC*, Nucl. Instr. and Meth. **A 439** (2000) 497-506
- [3] STAR-SVT Collaboration, *Studies of dynamics of electron clouds in STAR silicon drift detectors*, Nucl. Instr. and Meth. **A 439** (2000) 507-512

Chapter 6

Detector full-test

6.1 Standard procedure

In this Chapter the test procedure of the SDD modules will be described. Measurements were performed on 328 modules, 260 of which have been mounted on the ITS. The complete test of the modules has started in June 2006. All the ladders of Layer 3 were completed in October 2006 and those of Layer 4 in December 2006. The module assembly started with sensors already selected from previous tests. They were bonded to the front-end hybrids equipped with the AMBRA and PASCAL chips, which had already been tested. Afterwards a *semimodule* test was performed before the bonding of HV microcables to the detector and to the end-ladder cards (previously checked). Then the laser test and mapping was performed and the modules were finally mounted on the ladders.

The standard full-test procedure has a preliminary phase of geometrical optimization of the setup, in which the detector is aligned to one of the motor axis, the laser spot is focused on the detector surface and the laser intensity is tuned to obtain the proper signal-to-noise ratio. First the electronic noise and baselines are measured. Then the gain of PASCAL preamplifier is measured with the help of a test-pulse signal. Afterwards a short laser scan is done to tag dead channels and to check the injectors behaviour. For some module the injectors need a few time to start working. When all injector signals are seen, 200 events are registered to gather a good statistics of data for detector calibration. Finally a complete laser scan of the sensitive area is performed (the *mapping*) to determine the map of deviations of the reconstructed positions from the real ones.

6.2 Detector testing

With the help of the CCD camera the SDD surface is aligned to the trajectory plane. Then the detector drift direction is lined up to one of the motor axis

and the laser beam spot is focused on the surface plane, as explained in section 4.4.3. These operations are performed by moving the module support with micrometric screws.

Afterwards the electronic hybrids are biased at nominal values and a run of 200 events with laser and injectors switched off is acquired to measure the baselines of the anode channels. A single event gives two 256×256 (anodes) matrices, one for each half detector. A monitoring program is used to visualize on-line the events during the acquisition.

Baselines and noise measurements

Figure 6.1 shows the baselines of all the 256 channels of a half detector. For each channel the baseline value can be calculated from:

$$B_i = \frac{1}{N_{ev}} \sum_{n=1}^{N_{ev}} \frac{1}{256} \sum_j C_{i,j} \quad (6.1)$$

where n is the event number, N_{ev} in our case is 200 and $C_{i,j}$ is the measured signal in anode i and time bin j . In the plot the four regions delimited by vertical lines (anodes 64, 128 and 192) correspond to the four pairs of AMBRA/PASCAL chips. It can be seen that a clear discontinuity in the baseline mean value is present between the 2nd and the 3rd AMBRA/PASCAL pair (channel 128). The AMBRA chip can be programmed (via JTAG) to equalize the baselines of all the channels. This is done starting from the raw baseline measurement (as the one displayed in figure 6.1) and subtracting from each of the 256 anodes a proper value to have all the baselines equal to the lowest one. This baseline equalization is useful for simplifying the analysis of the subsequent measures with laser and test-pulse.

In all the tested modules the raw noise ¹ is very low, about 2-3 ADC counts versus the ~ 200 ADC counts of a laser shoot. Nevertheless a peculiar behaviour is observed at the boundary between different pairs of AMBRA/PASCAL, i.e. every 64 channels, as it is shown in figure 6.2(a) (where there are no noisy channels). This effect can be partially avoided with the subtraction of common-mode noise. Common-mode noise may originate from any external source in the proximity of the detector and leads to coherent variations in the signals across groups of channels. If the readout is analogue the common-mode noise contribution can easily be deduced from the pedestal heights and subtracted from the signals on an event-by-event basis. The noise of an anode is:

$$N_i(t) = N_i^0(t) + \alpha_i < N > (t) \quad (6.2)$$

where N_i^0 is the noise without common-mode contribution, α_i is the common-mode coefficient and $< N >$ is the mean over the noise of all the channels. Specifically the calculation of common-mode coefficients is performed independently for odd and even channels because of the design of the chips. The mean

¹The raw noise is the r.m.s. noise of the anode channels.

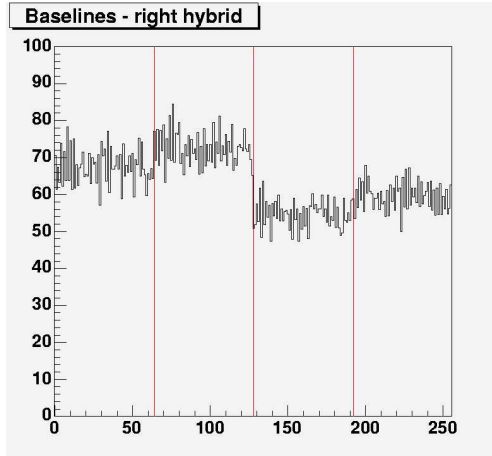


Figure 6.1: *Baselines before equalization vs. anode number. The 4 regions correspond to the 4 AMBRA/PASCAL pairs.*

value of the noise of all the odd or even channels is:

$$\langle N \rangle(t) = \frac{1}{128} \sum_i N_i(t) \quad (6.3)$$

The common-mode coefficient is the parameter of a linear fit performed on $N_i(t)$, thus:

$$\begin{aligned} \alpha_i &= \frac{\sum \langle N \rangle(t) N_i(t) - \sum \langle N \rangle(t) \sum N_i(t)}{\sum (\langle N \rangle(t))^2 - (\sum \langle N \rangle(t))^2} = \\ &= \frac{\sum_t \left(\frac{1}{128} \sum_i N_i(t) \right) N_i(t) - \left(\sum_t \frac{1}{128} \sum_i N_i(t) \right) \left(\sum_t N_i(t) \right)}{\sum_t \left(\frac{1}{128} \sum_i N_i(t) \right)^2 - \left(\sum_t \frac{1}{128} \sum_i N_i(t) \right)^2} \end{aligned}$$

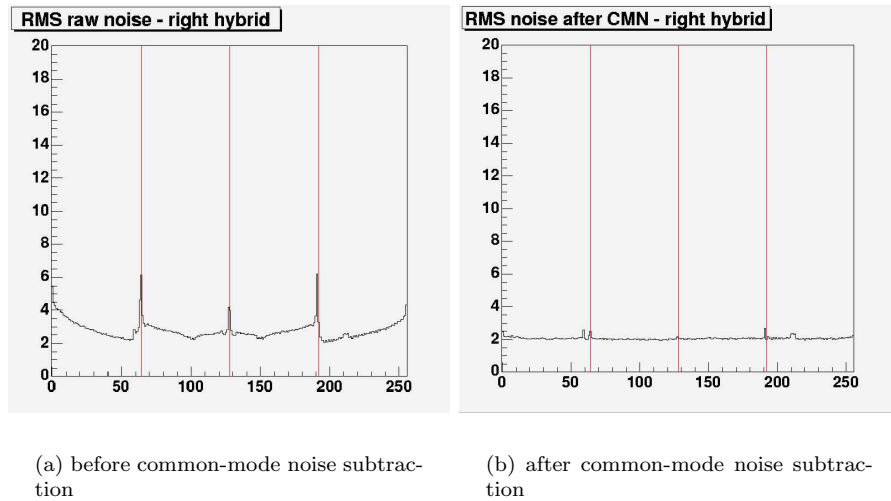
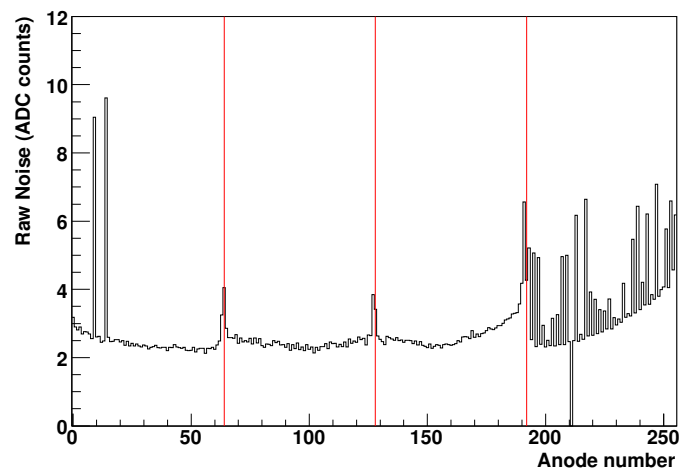
if the calculation is performed after subtracting the baseline values to the measured signals:

$$\alpha_i = \frac{\sum_t N_i(t) \langle N \rangle(t)}{\sum_t (\langle N \rangle(t))^2} \quad (6.4)$$

Figure 6.2(b) shows the r.m.s. noise after the subtraction of the common-mode noise. It can be seen that the level of noise is the same for all the channels. Figure 6.3 shows the r.m.s. noise before equalization for a detector with one dead and many noisy channels.

Gain measurement

After baseline equalization 200 events are collected to measure the preamplifier gain for all the 256 channels of a half detector. This test is done by using the

Figure 6.2: *Electronics r.m.s. noise vs. anode number.*Figure 6.3: *Electronics r.m.s. noise vs. anode number. In the 4th sector 1 dead and many noisy channels are visible.*

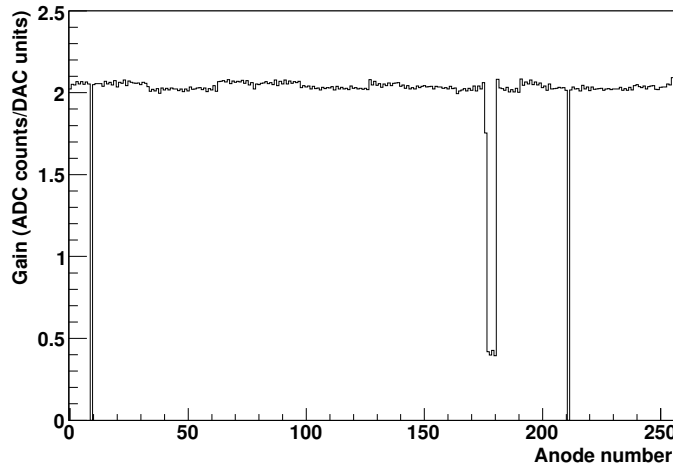


Figure 6.4: *PASCAL gain for the 256 channels of a half detector.*

internal test-pulse generator. PASCAL is equipped with a system that allows the generation of a programmable voltage step which is fed through calibration capacitors to the input of each preamplifier. The calibration circuit delivers input signals up to a maximum of 32 fC with a step of 0.06 fC. Gain values measured with the test-pulse will be used during the ALICE off-line analysis to equalize the gain of the different channels. This equalization allows a consistent measurement of the energy released in the detector by the crossing particles which is used for PID. The test-pulse charge is set to three different values (411, 311, 211 in Digital to Analog Converter units ²) and for each configuration 200 events are acquired. For each anode channel the mean value of the peak amplitude of the registered signals is plotted versus the test-pulse charge and a linear fit is performed (figure 6.5). The fit slope gives the PASCAL gain. Figure 6.4 shows the gain value for all the 256 channels. The dead channels are visible as channels with gain = 0. The plot also shows some channels with low gain. Generally the dead channels are grouped by ~ 5 and have some adjacent noisy channel. This may be due to physical imperfections of the silicon wafer, causing an excessive current to circulate at the input of PASCAL preamplifier (shifting its working point from the optimal value), or to some broken chip-cable.

Short scan

The laser trajectory is the one described in section 4.3.1. This test allows a measurement of the baselines and of the noise while the motors are moving, so as to reproduce the total noise that could affect measurements during the

²A DAC unit corresponds to 0.06 fC.

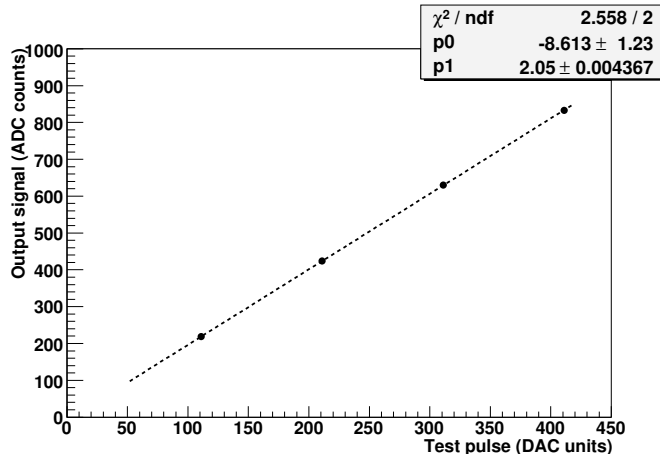


Figure 6.5: Registered signal vs. test-pulse charge for a single anode.

mapping. Furthermore raw noise and common-mode noise are estimated and dead channels tagging is performed. Typically the sensors mounted on Layer 3 had 2 or 3 dead channels on average, while some second choice³ modules (32) have been mounted on Layer 4.

Before the laser scan the baselines are set to their original value and the laser amplitude is properly tuned to ensure a signal-to-noise ratio > 30 without saturating the ADC, which allows a maximum of 1008 counts.

6.3 Mapping

6.3.1 Typical mapping results

In this section the results of the mapping test on a typical module are presented. Figure 6.6 shows the charge collected by the detector for each position of the laser. In the plot three vertical lines can be distinguished, where a smaller amount of charge is collected. These lines are due to laser reflection on the injector metallizations. Besides, in the lower zone of the map there is a large area, corresponding to the last positions performed by the trajectory, with less charge collected with respect to the rest of the detector surface. This may be due both to different surface characteristics of the sensor or to the fact that during the mapping, lasting about 40 minutes, the sensor may move from its position progressively losing the correct alignment with the motor axes. A possible reason for this misalignment effect could be the mechanical stress due to

³According to the selection criteria applied during sensor characterization measurements a *second choice* module is a class B sensor (with a high leakage current on a number of channels ranging from 2% to 4 % of the total and potential drop between correspondent cathodes on both sides of the wafer between 35 V and 60 V).

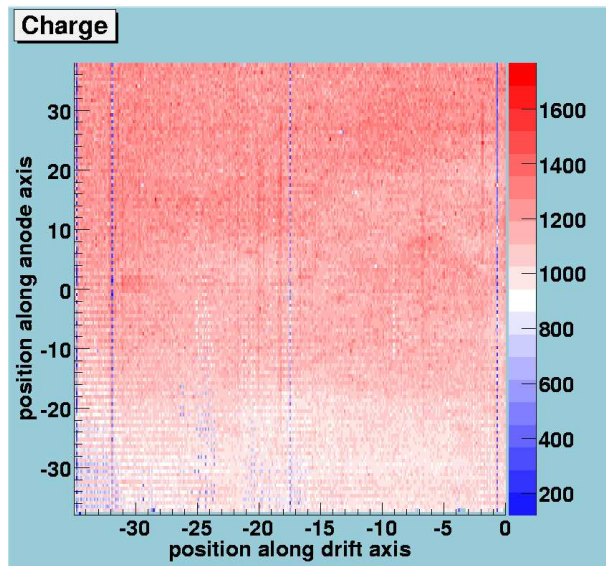


Figure 6.6: *Collected charge for a typical module.*

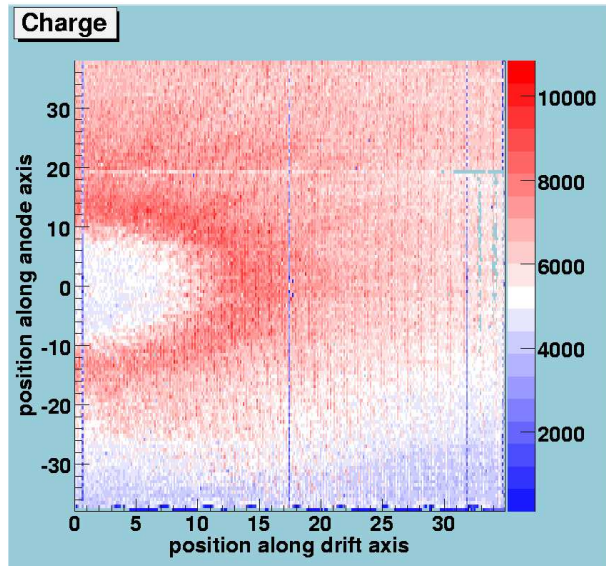


Figure 6.7: *Collected charge for a module showing surface defects.*

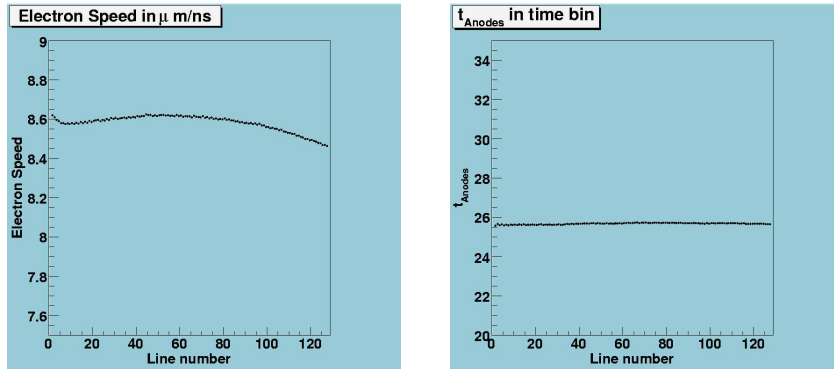


Figure 6.8: *Electron speed vs. mapping line.*

Figure 6.9: *Offset in the drift position vs. drift time plot.*

the cooling pipes, refrigerating the HV board, which are not perfectly fixed to the detector support. Figure 6.7 shows the charge collected by a detector with visible defects on its surface.

The electron speed value is obtained by means of a linear fit to the measured time-bin centroid as a function of the laser position along the drift coordinate. The slope of the line is the drift velocity. During the laser-mapping of a single module, two different phases can be distinguished :

- the detector is at room temperature and there are no effects due to higher temperature on sides (along anode direction). The situation is shown in figure 6.8, where the electron drift speed is plotted for each line of the map parallel to the anodes (the map starts from the left side). The first 5-6 lines of mapping are performed after few minutes from the switching-on of HV and LV bias and the average speed on these anodes is higher than standard.
- after few minutes from biasing, the voltage divider and the front-end electronics contribute to increase the temperature on both sides of the detector along anode direction, therefore decreasing the electron drift speed in these areas. The central part of the detector shows a lower temperature, and thus a higher drift speed, since the voltage divider power dissipation heats the external parts of the detector more than the central one.

Besides, the effect of the wrap-around cable is visible in the right part of the plot, where the average electron speed is lower than in the left side because of the power dissipation of the cable very close to the detector surface.

In figure 6.9 the time-bin centroid for charge released on one anode (t_{Anodes}), i.e. at 35 mm from the center, is shown. The values of the drift speed and of t_{Anodes} are used to calculate the impact position along drift direction starting from the measured time-bin centroid.

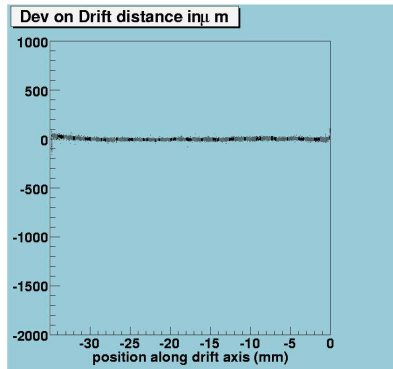


Figure 6.10: *Drift position deviations, indicating the voltage divider linearity.*

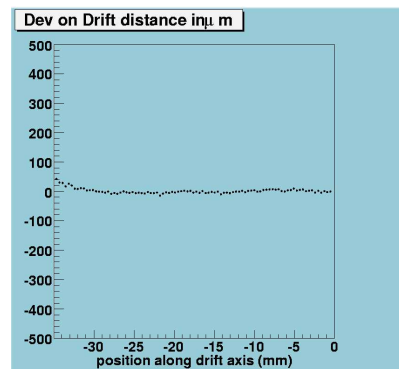


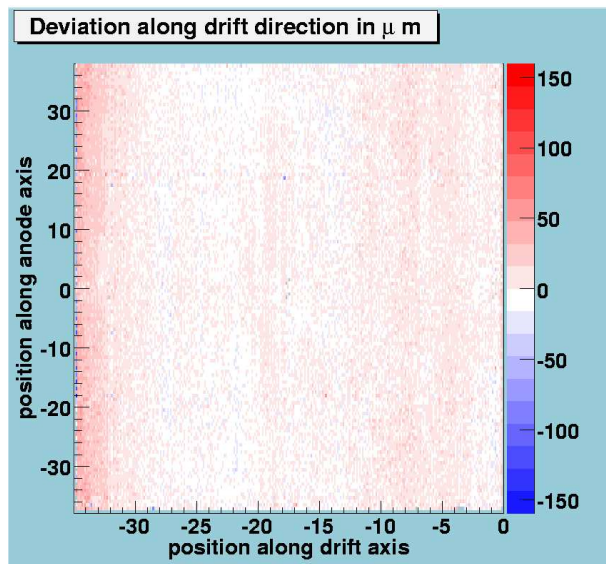
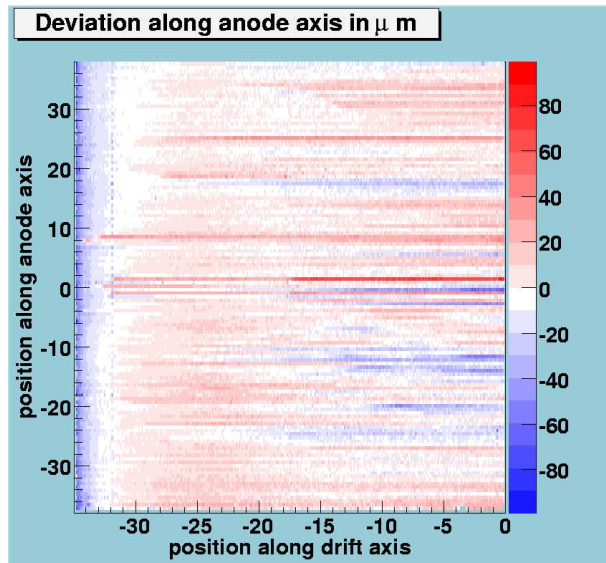
Figure 6.11: *Mean values over the mapping lines of drift distance deviations.*

Figure 6.10 shows the difference between the position along the drift coordinate estimated from the measured time-bin and the one known from the laser position. Data from all the mapping lines are plotted. The fact that all the residuals⁴ are approximately zero indicates the linearity of the voltage divider. In figure 6.11 the mean values over all the mapping lines are shown. The increase at the first line numbers shows a small non-linearity in the voltage divider.

Deviations of the reconstructed coordinates along drift axis from the real ones (defined by the laser positions) are represented in figure 6.12 in color scale (or grey scale for the b/w version) as a function of the laser position on the detector surface. In figure 6.14 the distribution of the deviations is shown: it is almost Gaussian with an r.m.s. value of about $13 \mu\text{m}$. The distribution is centered at $1.3 \mu\text{m}$, while the expected value for the mean value of the residuals is zero. By plotting the same distribution on a logarithmic scale (figure 6.15) and performing a Gaussian fit, we can see that in fact it is not a perfect Gaussian distribution. In particular there is an anomalous peak at about $80 \mu\text{m}$, which corresponds to the points with a higher deviation value in the left side of figure 6.12. Nevertheless the σ of the Gaussian fit, i.e. the resolution on the drift coordinate, is about $9 \mu\text{m}$ and it is well below the $30 \mu\text{m}$ required by ALICE for almost all the detectors we studied. Besides the fit is centered at zero, as expected. The maximum deviation observed is about $100 \mu\text{m}$. The bidimensional map shows that the residuals are uniform through all the sensitive area: no doping inhomogeneities and significant voltage divider non-linearity effects are present.

Figure 6.13 shows the bidimensional map of the residuals along anode di-

⁴The *residual* is defined as the difference between the reconstructed coordinate and the laser position.

Figure 6.12: *Deviations along drift direction.*Figure 6.13: *Deviations along anode direction.*

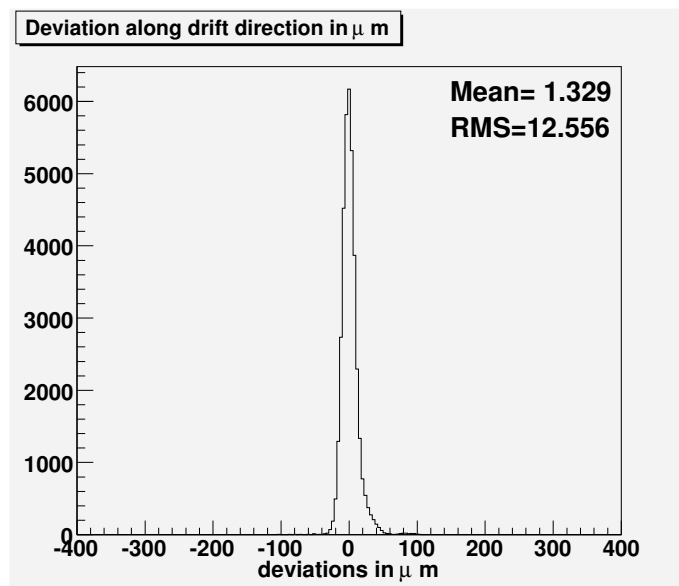


Figure 6.14: Histogram of eviations along drift direction.

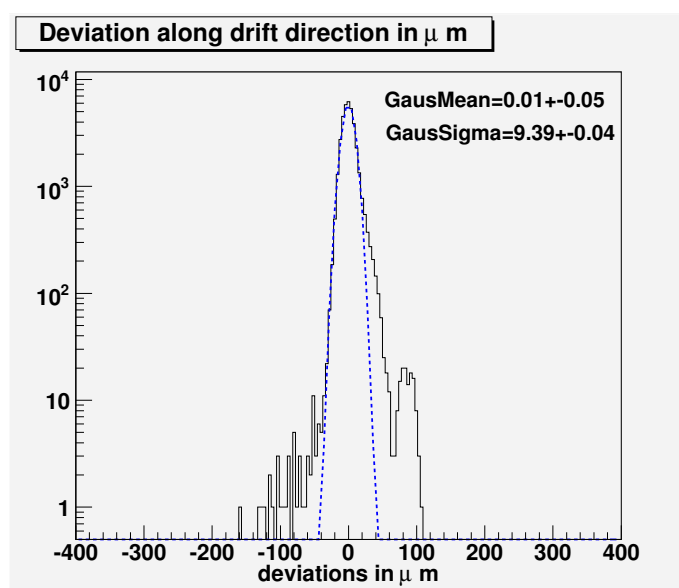
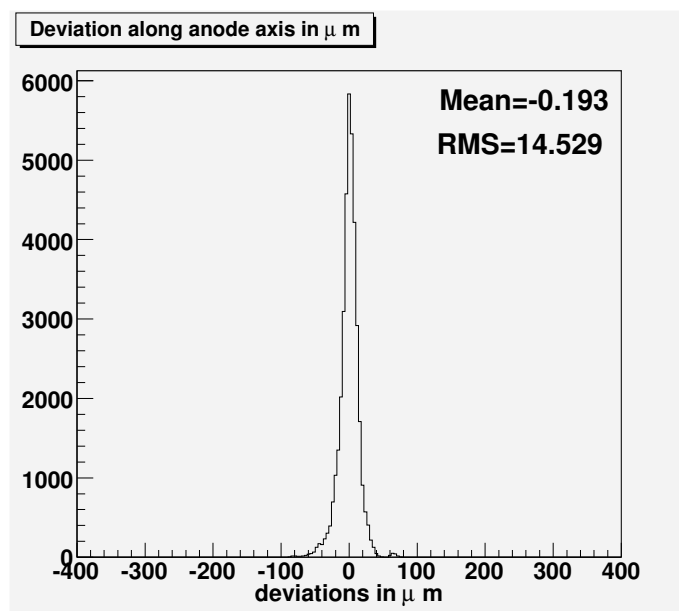
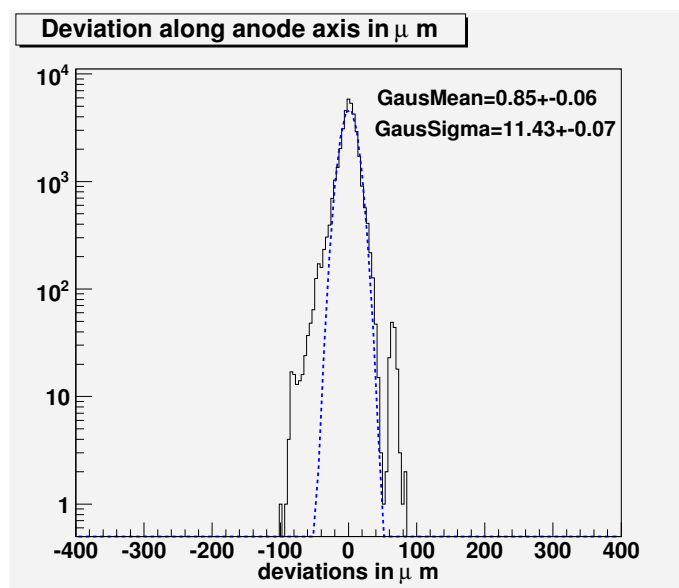


Figure 6.15: Histogram of deviations along drift direction (logarithmic scale).

Figure 6.16: *Histogram of deviations along anode direction.*Figure 6.17: *Histogram of deviations along anode direction (logarithmic scale).*

rection. It has a striped structure in proximity of some anodes (right part of the plot) due to systematic effects in the calculation of the centroid, probably caused by differences in channel gains. A more refined analysis taking into account gain differences should correct this problem; however this is quite a small effect. In figure 6.16 the distribution of the residuals is reported: it is centered at zero and the r.m.s. is about $15 \mu\text{m}$. Figure 6.17 shows the same plot on a logarithmic scale. The Gaussian fit is centered at zero and the value of σ is about $11.5 \mu\text{m}$. Therefore, as well as along the drift direction, the resolution on the anode coordinate is below the required $30 \mu\text{m}$. The maximum value of the residuals is about $100 \mu\text{m}$.

6.3.2 Non-linearity of the voltage divider

The non-linearity of the voltage divider may cause a systematic error in the reconstruction of the impact position because the relation between drift time and drift distance is no longer linear. If the drift potential distribution is non-linear, the electron drift speed is not the same along all the drift coordinate. Therefore the laser spot position along drift direction can not be estimated by simply multiplying the drift time centroid by the drift speed of plot 6.8. In this case an off-line correction of the experimental data using the map of deviations is mandatory. Figure 6.18 shows the average deviations along drift coordinate for a detector with a non-linear voltage divider. Comparing with figure 6.10 it can be seen that the residuals are significantly different from zero and depend on the drift distance. These deviations have a different shape for each detector and the only way to correct them is to map all the detectors. The deviations on drift coordinates as a function of laser positions on the detector are shown in figure 6.20. The deviations can reach values as large as $400 \mu\text{m}$. In figure 6.19 the histogram of the residuals is shown: the distribution is clearly not Gaussian due to the systematic effect connected with the non-linearity of the voltage divider. It is evident that a correction for this effect is mandatory to reach the required resolution of $30 \mu\text{m}$.

6.3.3 Doping inhomogeneities

As explained in section 3.3.1 any inhomogeneity of dopant concentration in the silicon bulk may affect position reconstruction both along the drift and anode coordinate. In a first set of prototype detectors (produced on WACKER silicon wafers), which have not been mounted on the SDD ladders, strong doping gradients were revealed, showing a circular concentric structure. This circular structure is characteristic of the way in which the silicon ingot is produced [1]. In this case we need to apply a correction using the measured laser map [2]. Since the amount of data is very big, a compression algorithm was developed. By using a cylindrical system of coordinates the circles become straight lines. A Fourier transform is performed on this new map and a threshold is applied to the Fourier coefficients. In this way the most significative ones can be selected. The reduction obtained is almost a factor 60. Then, during physics data anal-

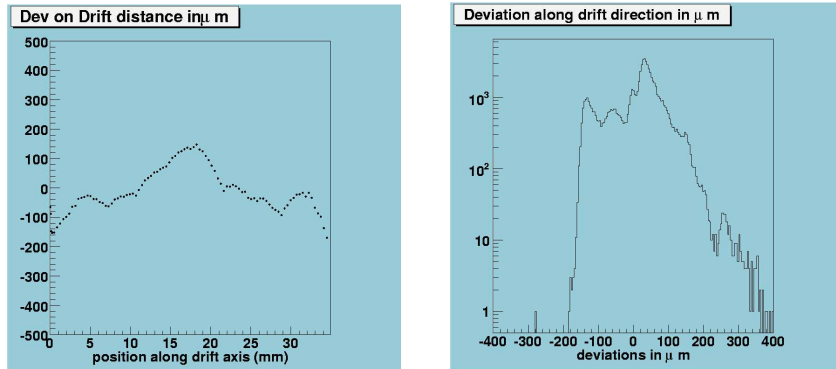


Figure 6.18: Mean value of the drift distance deviations as a function of the mapping line for a detector showing a non-linearity of the voltage divider.

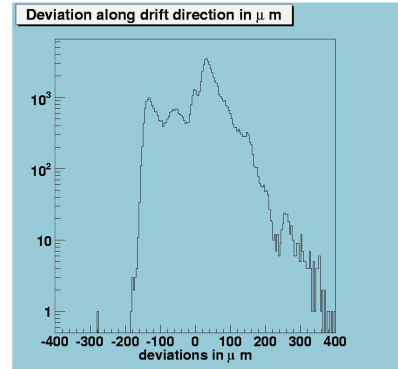


Figure 6.19: Deviations of the reconstructed position along drift direction for a detector showing a non-linearity of the voltage divider.

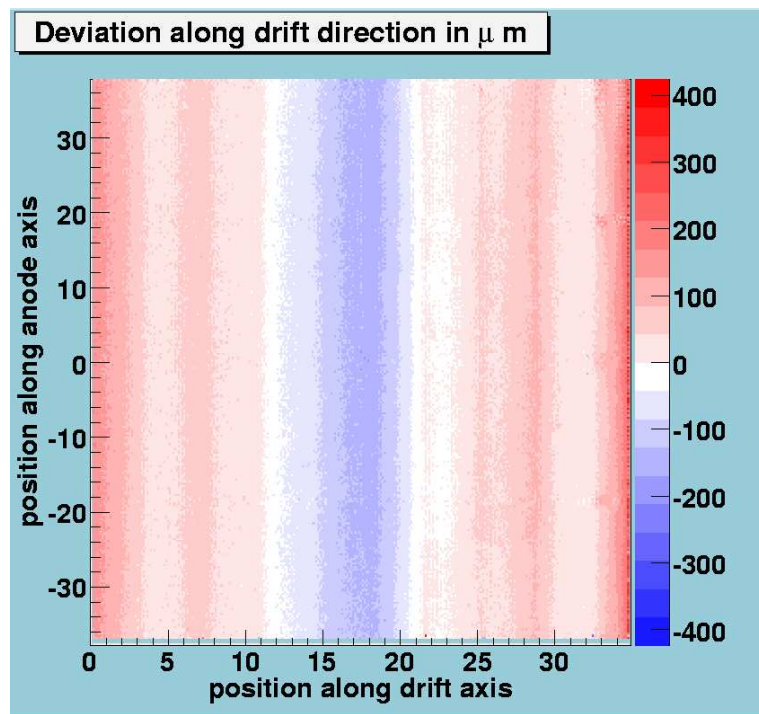


Figure 6.20: Deviations of the reconstructed positions along drift direction for a detector showing a non-linearity of the voltage divider.

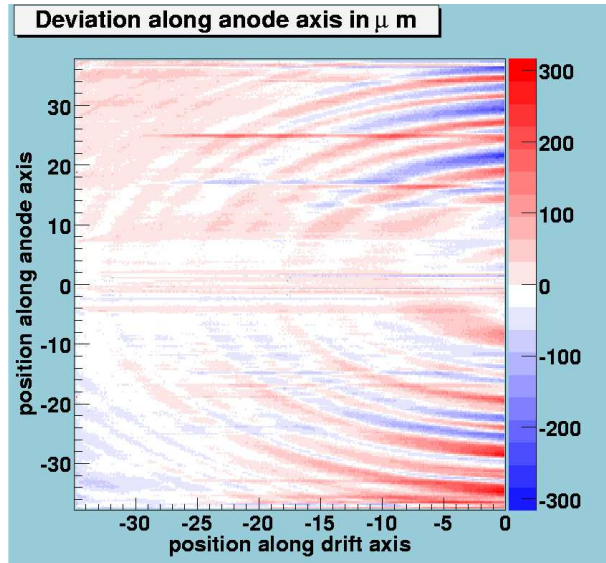


Figure 6.21: *Deviations of the reconstructed positions along anode direction. The doping inhomogeneity effect is clearly visible.*

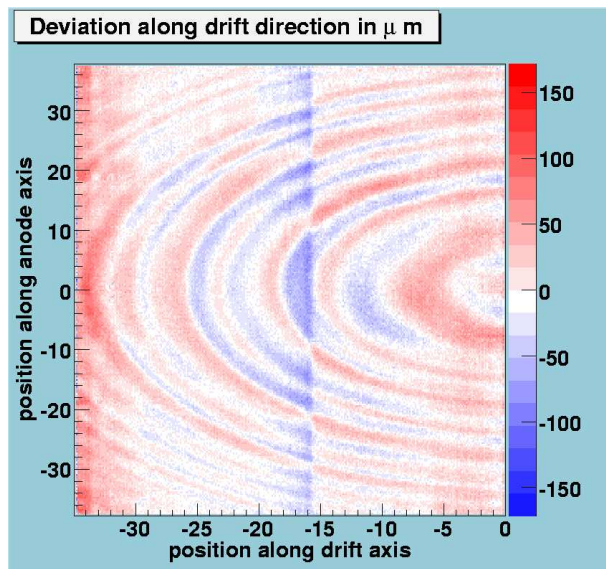


Figure 6.22: *Deviations of the reconstructed positions along drift direction. The doping inhomogeneity effect is clearly visible.*

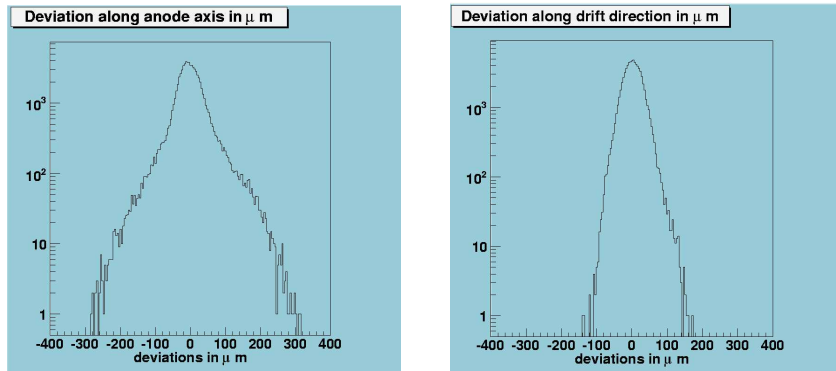


Figure 6.23: *Deviations of the reconstructed position along anode direction. The non-Gaussian shape is due to doping inhomogeneities.*

Figure 6.24: *Deviations of the reconstructed position along drift direction. The non-Gaussian shape is due to doping inhomogeneities.*

ysis the inverse Fourier transform must be performed to calculate the position correction to apply. Figure 6.23 shows a distribution of the deviations of the reconstructed position along anode direction. The distribution is not Gaussian and the deviations can reach values as large as $300 \mu\text{m}$. Figure 6.21 is a typical map of deviations along anode direction and shows that the systematic effect of doping inhomogeneities affects anode coordinate as well (while the non-linearity of the voltage divider affects the drift coordinate only). Similar results are obtained for the drift coordinate and are shown in figures 6.22 (map of deviations) and 6.24 (residual distribution). After this first phase of prototype detector production, we started to produce the final version of ALICE SDD on new material (i.e. NTD wafers produced by TOPSIL). Among the ~ 300 detectors mapped only 4 were affected by doping inhomogeneities problems (WACKER). All the others, produced from the better quality silicon (TOPSIL), do not show the radial dependence of the dopant concentration. Nevertheless on Layer 4 about 40 detectors were mounted showing circular structures with deviations lower than $50 \mu\text{m}$. In this case the systematic effect is negligible.

6.4 Perspective of injector data analysis

Silicon Drift Detectors are very sensitive to temperature fluctuations. In the ALICE SDDs the current flowing in the integrated voltage divider causes heat dissipation, giving rise to temperature gradients in the sensitive region of the SDD, which reflecte in the drift velocity dependence on the anodic coordinate shown in figure 6.8. Variations of the environmental temperature during operation also influence the detector temperature and thus the drift speed. Therefore it is extremely important to be able to measure the drift velocity during data

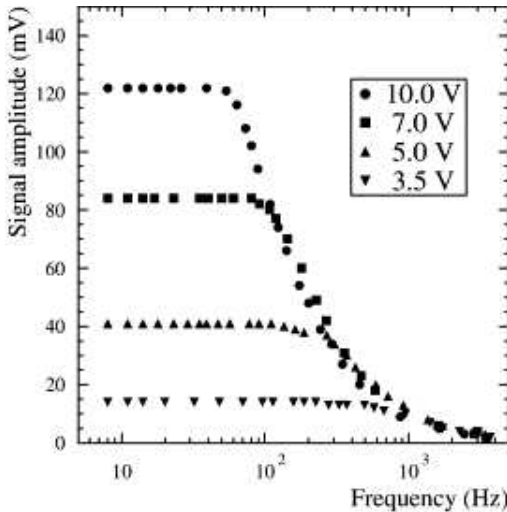


Figure 6.25: *Semilogarithmic plot of the signal amplitude as a function of the frequency of the injection pulse.*

acquisition, to update the value of electron mobility (and hence of the drift velocity) to be used in the analysis. Temperature variations of 0.1 K require the measure of the drift velocity with an accuracy of 0.1 % [3]. For this purpose SDDs are equipped with MOS charge injectors, which allow the drift velocity calibration through the measurement of the time-bin centroid of the signal generated by injecting charge at known positions on the sensor. A description of the injectors can be found in Chapter 3 or in [4].

During the detector full-test one injector event is registered at the end of every line of the map, resulting in 257 events. Furthermore other 200 events are collected with a pulse generator trigger. These measurements require particular care in the choice of the gate pulses (and thus of the trigger rate). The gate pulses frequency influences the process of electron accumulation below the gate oxide. If the gate pulse frequency is too high the injected signal charge decreases [4, 5]. Figure 6.25 shows the behaviour of the injector signal amplitude as a function of the frequency of the injection pulse: according to these results during the preliminary tests the injector events are acquired with a trigger rate of about 100 Hz.

A typical injector event is shown in figure 6.26, for a half module. Three lines of 33 injectors are visible at distances from anodes corresponding to 50, 120 and 200 time-bins. The amount of charge injected is different for the three lines. In particular the first line (time-bin 50) always injects less charge than the other two. Besides, a parasitic signal is present at time-bin number 30, which

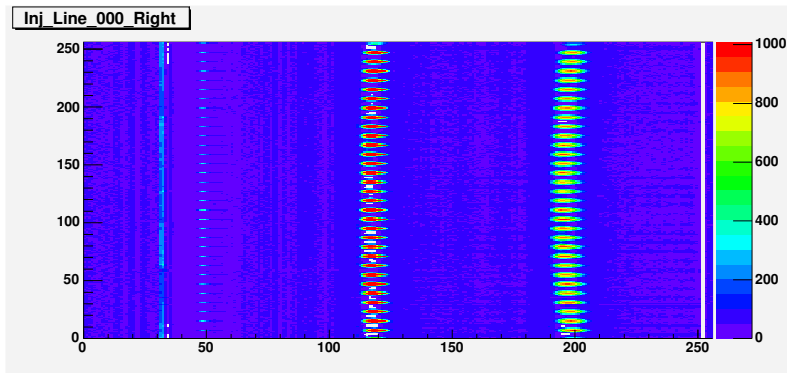


Figure 6.26: *A typical injector event.*

gives the time offset. The left part of plot 6.26 corresponds to shorter drift times (proximity of the anode row). The plot shows clearly that the drift time for the injectors of the third line from anodes is not constant. In particular the shape of the *injector line* seems to be parabolic. This effect is due to the temperature distribution along the detector and it is consistent with the parabolic shape of the drift speed measured during laser mapping (figure 6.8). Signals in the outermost and hottest regions of the detector show a longer drift time with respect to the most central ones.

Along drift direction the three injector signals for each anode position should be distributed along a straight line, provided that the drift field is uniform. In early detector prototypes the first injector line was placed in the very proximity of the collection region, where the potential distribution is not linear because of detector design. In this case the injector points along drift were compatible with a parabolic distribution. In the final detector design the injector line positions along drift have been optimized to avoid this effect and a linear fit can be performed to the three points. The drift velocity is given by the slope of the linear fit for each position along anodes. In the cases where some of the injectors were not working, the slope is calculated with only two points or one point and the time zero parasitic signal.

Figure 6.27 shows a comparison between the drift speed estimated from the laser points and from the injector data. The two results are in good agreement within the statistical errors. The error on the velocity extracted from laser data is much smaller because we used 290 points to perform the fit instead of the 3 (or less) used in the case of injector procedure. In both cases the error on the experimental points is given by the signal r.m.s. The left part of plot 6.27 refers to a half module with all the 3 injector lines. The right part shows the case of a half module with only one injector line: as expected higher errors on the drift velocity are obtained, since the fit is performed on two points only. Furthermore, in figure 6.28 we see a case in which the drift velocity estimated from

injector data is systematically lower than the one estimated with laser points (referring to a module with only one injector line). This could be due to a large deviation on drift position, because of the non-linearity of the voltage divider, in the position of the injector line.

Besides, from the data generator (DG2020) settings, we expect a fixed offset of 200 ns, corresponding to 8 time-bins, between laser and injector triggers, which would result in a systematic shift of the impact positions reconstructed by injector data, with respect to laser data. Figure 6.29 compares the time zero (offset) value extracted from mapping results (figure 6.9) to the same value relative to injector data. As expected the difference between the two values is about 8 time bins. The remaining difference ($\simeq 0.5$ t.b.) may be due to different delays in the electronic chain or to different synchronization of the trigger signal with the clock of the front-end chips. This effect is however important to be understood and corrected in a future analysis because a difference of 0.5 time-bins, i.e. 12 ns, introduces a systematic effect on the drift coordinate of about 100 μm for a drift speed of $\simeq 8 \mu\text{m}/\text{ns}$.

6.5 Conclusions

The results of the tests performed on 328 modules, during the production and construction phases, are summarized in table 6.1. Only 7 modules have been rejected after the laser tests. In particular, the modules rejected after the laser mapping had the following problems:

- position deviations due to the non-linearity of the voltage divider of $\sim 1 \text{ mm}$ (Layer 3)
- laser events registered only when shooting near the anodes (Layer 4)
- current in the voltage divider increases with time (Layer 4)

Besides, Layer 4 has been equipped with 32 out of 176 second choice detectors with about 20 dead or noisy channels each. For all the modules which have been mounted on the ladders, the laser test allowed to determine the map of residuals due to the voltage divider non-linearity and to the dopant concentration inhomogeneity (this last is important for only 4 detectors), which will be used to correct the data acquired by the SDD for systematic effects. The injector lines are working (at least partially⁵) on all the detectors. The time under HV after which the injector signals start to appear is below 4 hours for all the modules. In about 10 modules the injector signal appears after more than 5 hours of module biasing.

⁵In the case of an entire line not working, the JFET generating the injector signal for that line was replaced and the injector line was recovered. In the case of lines with only part of the 33 injectors working, it was verified on few modules that after waiting a proper amount of time (which could be as long as 5 hours) all the injectors which were not immediately working started to visible.

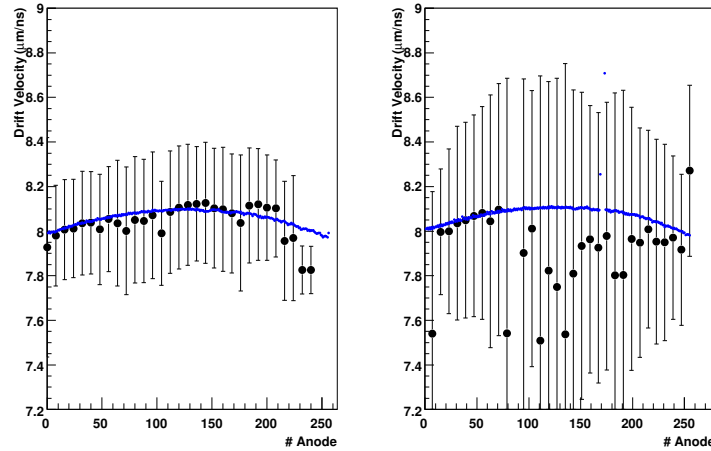


Figure 6.27: Comparison between drift speed estimated from the mapping (small points) and from injectors (large circles) for both sides of the detector.

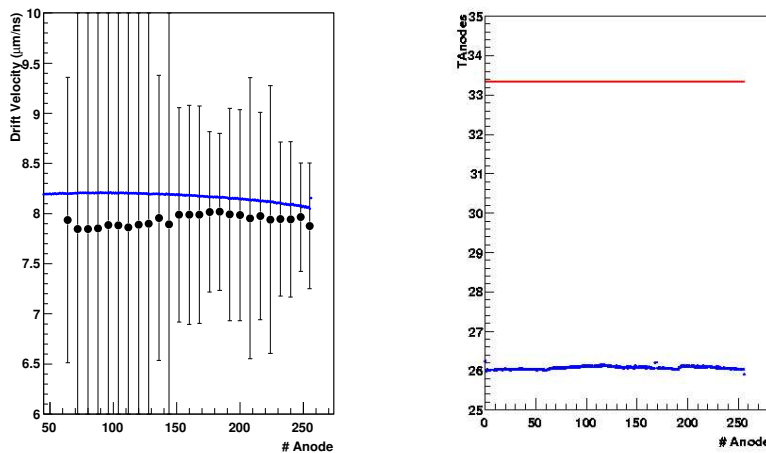


Figure 6.28: Comparison between drift speed estimated from the mapping (small points) and from injectors (large circles). A systematic effect is shown.

Figure 6.29: Comparison between t_{Anodes} for laser data (small points) and time-zero from injectors (continuous line).

Table 6.1: *Full-test results for the 328 modules studied.*

	Layer 3	Layer 4
tested	130	198
rejected after preliminary tests	3	1
doping fluctuations $> 100 \mu\text{m}$	4	-
doping fluctuations $< 50 \mu\text{m}$	-	41
rejected after mapping	1	2

For each module, during the preliminary tests 200 injector events are registered and other 257 are acquired during the laser mapping. These data allow a comparison between the electron drift speed extracted from laser and injector measurements. In the first case the electron drift speed can be estimated with a greater accuracy because of the higher statistics. Nevertheless injector data are of extreme importance since they allow the study of the performance of such devices during data analysis. Besides, the charge generation process induced in the detector by injector pulses is physically more similar to the case of a real crossing particle than in the case of a laser event. From a preliminary study of these events it emerged that drift velocity values extracted from injector and laser data are in good agreement within the statistical error. The precision on the measurement is strongly influenced by the number of working injector lines. Future analysis should be able to provide a deeper insight into the problem, allowing a concrete understanding of injector performance and detector calibration using such devices.

Bibliography

- [1] W. Von Ammon, H. Herzer, Nucl. Instr. and Methods **226** (1984) 84
- [2] G. Batigne, *9th ICATPP Conference Proceedings*, Villa Olmo (Como), October 2005
- [3] D. Nouais at al. Nucl. Instr. and Meth. **A 450** (2000) 338
- [4] V. Bonvicini, P. Burger et al., *Characterizing large area silicon drift detectors with MOS injectors*, Il Nuovo Cimento **112 A** (1999) 1-2
- [5] C. Piemonte, A. Rashevsky et A. Vacchi, *Device Simulation of the ALICE Silicon Drift Detector*, ALICE Internal Note/ITS: ALICE-INT-2002-15 1.0

List of Figures

1.1	<i>The phase diagram of QCD.</i>	6
1.2	<i>The order of the phase transition.</i>	7
1.3	<i>Energy density behaviour predicted by lattice QCD calculations: a phase transition is expected at a temperature of about 200 MeV.</i>	8
1.4	<i>Peripheral and central collision in the centre of mass system of the two nuclei.</i>	11
1.5	<i>Space-time evolution of a central collision between heavy ions.</i>	13
1.6	<i>Elliptic flow in peripheral collisions: almond shaped overlap zone generated just after an $A+A$ collision where incident nuclei are moving along the z axis (left). Spatial distribution (top right). Momentum distribution after elliptic flow develops (bottom right).</i>	17
1.7	<i>3 generations of experiments at SPS.</i>	18
1.8	<i>The ratio between J/Ψ and DY cross sections as a function of L, for several collision systems, compared to the normal nuclear absorption pattern.</i>	19
1.9	<i>Anomalous J/Ψ suppression as a function of energy density, for $S-U$ and $Pb-Pb$ collision systems, compared to the normal nuclear absorption pattern. Expected J/Ψ are extracted from a fit to pA data.</i>	20
1.10	<i>dN/dY at midrapidity as a function of the total number of participants for strange and multy-strange baryons.</i>	21
1.11	<i>Phase-space integrated kaon to pion multiplicities from NA49 experiment.</i>	21
1.12	<i>Inverse slope T of transverse mass spectra as a function of particle mass. Data are from WA97, NA44 and NA49 experiments in $Pb-Pb$ collisions at CERN SPS.</i>	22
1.13	<i>Transverse momentum distribution for charged hadrons. Data refer to different centrality hypothesis in $Au-Au$ collisions: values of 0 – 5% indicate a truly central event, while values of the order of 80 – 92% represent a peripheral collision.</i>	23
1.14	<i>Nuclear modification factor R_{AA} in different centrality conditions. Data are referred to the highest centrality sample (0 – 5%).</i>	24

2.1	<i>The range of Bjorken x and M^2 in nucleus-nucleus collisions for SPS, RHIC and LHC. Lines of constant rapidity are shown.</i>	30
2.2	<i>Longitudinal view of the ALICE detector.</i>	34
2.3	<i>Layout of the ITS.</i>	40
2.4	<i>Prototype of the ITS SDDs with all detectors and the cooling system.</i>	44
3.1	<i>Energy loss as a function of the particle momentum.</i>	49
3.2	<i>Principle of operation of a silicon drift detector.</i>	51
3.3	<i>Double p^+n junction: not fully depleted (a), of a not fully depleted single semiconductor wafer with two p^+n junctions at the two sides (b) and fully depleted single semiconductor wafer with two p^+n junctions at the two sides (c).</i>	52
3.4	<i>Parabolic profile of the potential distribution in a fully depleted junction with a p^+ cathode on each side.</i>	52
3.5	<i>Numerical simulation of the potential distribution in the drift region of a silicon drift detector.</i>	54
3.6	<i>Uniformity of electric field in the drift channel of a SDD for different values of the ratio r between cathode pitch and detector thickness.</i>	55
3.7	<i>Typical real potential distribution in the collection zone of a silicon drift detector (numerical simulation).</i>	56
3.8	<i>Layout of the ALICE SDD. The sensitive area is split into two different regions by the central, highest voltage, cathode. Each drift region has one row of 256 collection anodes and three rows of 33 point-like MOS charge injectors for monitoring the drift velocity. Drift and guard regions have independent built-in voltage dividers.</i>	57
3.9	<i>High voltage divider at the cathodes and guard region (a detail).</i>	59
3.10	<i>Effect of doping inhomogeneities on the particle trajectory.</i>	60
3.11	<i>Principle of operation of the MOS charge injectors.</i>	61
3.12	<i>Schematic representation of a SDD hybrid: the 4 pairs of PAS-CAL and AMBRA are shown. The upper part of the figure represents the connections with detector anodes.</i>	62
3.13	<i>The SDD are mounted at different radii in both r_z and r_ϕ planes to obtain the full coverage in the acceptance region (units are millimetres).</i>	63
3.14	<i>Support structure of the SDD ladders (with a layer of ladders already mounted).</i>	64
3.15	<i>Detector module mounted on a ladder: the front-end boards are shown folded to the two sides of the structure. Microcables are not shown.</i>	64
3.16	<i>The SDD module.</i>	66
3.17	<i>Schematic layout of a SDD front-end module.</i>	67
4.1	<i>Experimental set-up for laser mapping and diffusion measurements.</i>	70
4.2	<i>Laser-camera system.</i>	71

4.3	<i>Schematical representation of the set-up.</i>	72
4.4	<i>Trigger system.</i>	72
4.5	<i>Laser trajectory for preliminary measurements.</i>	73
4.6	<i>Laser trajectory for diffusion measurements.</i>	74
4.7	<i>Laser trajectory for mapping.</i>	76
4.8	<i>Probability of transmission as a function of photon energy.</i>	77
4.9	<i>Map of the charge collected by the detector for different laser wavelengths.</i>	78
4.10	<i>Determination of the laser-camera offset.</i>	79
4.11	<i>Reference crosses for detector alignment on the top side of the SDD sensor.</i>	80
4.12	<i>The angle θ between detector and motors axes.</i>	80
4.13	<i>Measurement of the angle between motors.</i>	80
5.1	<i>Evolution of the electron cloud during the drift.</i>	83
5.2	<i>Charge collected (ADC counts) by the anode under study vs. laser position along anode coordinate for a single scanning line.</i>	86
5.3	<i>Position along drift direction (mm) vs. drift time (time bins).</i>	88
5.4	<i>Drift speed vs. anode number for different experimental conditions.</i>	89
5.5	<i>Charge collected (ADC counts) by a single anode vs. laser position along anode coordinate for different scanning lines. Far from the anodes the electron cloud diffusion effect shows up in the charge distribution broadening and lowering.</i>	91
5.6	<i>$\sigma(t)^2$ in mm^2 vs. drift time in ns. The black solid line represents the linear fit to data.</i>	92
5.7	<i>Fraction of the charge collected (cumulative function) vs. position of the light spot. (a)-(c) individual anodes, (d) sum over three anodes.</i>	93
5.8	<i>Cloud profiles (y is the anode coordinate).</i>	95
5.9	<i>Dependence of the cloud size on drift time. Points are data. Solid line shows a solution of the continuity equation with both diffusion and Coulomb repulsion contributions. Dashed line shows the diffusion only. Dotted line shows Coulomb repulsion only.</i>	96
6.1	<i>Baselines before equalization vs. anode number. The 4 regions correspond to the 4 AMBRA/PASCAL pairs.</i>	100
6.2	<i>Electronics r.m.s. noise vs. anode number.</i>	101
6.3	<i>Electronics r.m.s. noise vs. anode number. In the 4th sector 1 dead and many noisy channels are visible.</i>	101
6.4	<i>PASCAL gain for the 256 channels of a half detector.</i>	102
6.5	<i>Registered signal vs. test-pulse charge for a single anode.</i>	103
6.6	<i>Collected charge for a typical module.</i>	104
6.7	<i>Collected charge for a module showing surface defects.</i>	104
6.8	<i>Electron speed vs. mapping line.</i>	105
6.9	<i>Offset in the drift position vs. drift time plot.</i>	105
6.10	<i>Drift position deviations, indicating the voltage divider linearity.</i>	106

6.11	<i>Mean values over the mapping lines of drift distance deviations.</i>	106
6.12	<i>Deviations along drift direction.</i>	107
6.13	<i>Deviations along anode direction.</i>	107
6.14	<i>Histogram of eviations along drift direction.</i>	108
6.15	<i>Histogram of deviations along drift direction (logarithmic scale).</i>	108
6.16	<i>Histogram of deviations along anode direction.</i>	109
6.17	<i>Histogram of deviations along anode direction (logarithmic scale).</i>	109
6.18	<i>Mean value of the drift distance deviations as a function of the mapping line for a detector showing a non-linearity of the voltage divider.</i>	111
6.19	<i>Deviations of the reconstructed position along drift direction for a detector showing a non-linearity of the voltage divider.</i>	111
6.20	<i>Deviations of the reconstructed positions along drift direction for a detector showing a non-linearity of the voltage divider.</i>	111
6.21	<i>Deviations of the reconstructed positions along anode direction. The doping inhomogeneity effect is clearly visible.</i>	112
6.22	<i>Deviations of the reconstructed positions along drift direction. The doping inhomogeneity effect is clearly visible.</i>	112
6.23	<i>Deviations of the reconstructed position along anode direction. The non-Gaussian shape is due to doping inhomogeneities.</i>	113
6.24	<i>Deviations of the reconstructed position along drift direction. The non-Gaussian shape is due to doping inhomogeneities.</i>	113
6.25	<i>Semilogarithmic plot of the signal amplitude as a function of the frequency of the injection pulse.</i>	114
6.26	<i>A typical injector event.</i>	115
6.27	<i>Comparison between drift speed estimated from the mapping (small points) and from injectors (large circles) for both sides of the detector.</i>	117
6.28	<i>Comparison between drift speed estimated from the mapping (small points) and from injectors (large circles). A systematic effect is shown.</i>	117
6.29	<i>Comparison between t_{Anodes} for laser data (small points) and time-zero from injectors (continuous line).</i>	117

List of Tables

2.1	<i>LHC machine parameters for pp and Pb-Pb runs for ALICE.</i>	31
2.2	<i>ITS material budget traversed by straight tracks perpendicularly to the detector surface. Units are percentages of radiation length.</i>	42
2.3	<i>Dimensions of the ITS detectors (active areas).</i>	43
2.4	<i>Parameters of the various detector types. A module represents a single sensor element.</i>	43
3.1	<i>The main characteristics of the ALICE silicon drift detectors.</i>	58
3.2	<i>The main parameters of the ALICE SDD layers and ladders.</i>	65
5.1	<i>Measured drift speed and estimated electron mobility and detector temperature under different experimental conditions.</i>	90
5.2	<i>Temperature, electron mobility and diffusion coefficient under different experimental conditions.</i>	90
6.1	<i>Full-test results for the 328 modules studied.</i>	118